The University of Kansas

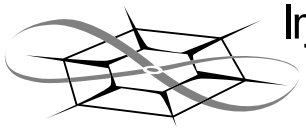

Information and Telecommunication Technology Center

Technical Report

Development of a 1319-nm Laser Radar Using Fiber Optics and RF Pulse Compression

Christopher T. Allen and Sek Ken Chong

ITTC-RSL-FY2002-TR-18680-01

May 2002

Project Sponsor:
Instrument Incubator Program, NRA-98-OES-05
NASA, Langley Research Center

Abstract

Laser radar systems will play an increasingly important role in global climate change monitoring applications. The fine spatial and range resolution capabilities of laser radar systems make them specially qualified for this work. The current generation of laser radar systems employ short-duration, high peak power pulses, typically using modest pulse repetition frequencies to prolong the limited laser lifetimes associated with such applications.

We have demonstrated the feasibility of a concept that uses low-peak power, long-duration laser pulses to achieve range a theoretical accuracy comparable to short-duration, high-peak power systems. Using optical heterodyne downconversion and RF pulse compression we have achieved receiver sensitivities that are compatible with a low-peak power laser altimeter. Through analysis, simulation, and laboratory demonstration, we have demonstrated the validity of this concept.

Our laboratory breadboard uses standard, single-mode optical fiber, off-the-shelf fiber-optic modulators, amplifiers, and photodetectors. An off-the-shelf 1319-nm single-mode laser serves as the optical source. RF and digital signal processing techniques used commonly in modern radar systems are also employed to improve the receiver sensitivity. Results from our laboratory experiments indicate a receiver sensitivity of about -90 to -100 dBm. Pulse repetition frequencies of 1000 to 4000 Hz were used.

Using commercial-grade astronomical telescopes to launch and receive our optical signal from free space, we measured the range to both man-made and natural extended targets at ranges of 3 to 35 m.

With these findings, we have validated the concept of applying coherent optical downconversion and RF signal processing to reduce the required peak transmitted power.

TABLE OF CONTENTS

Chapter 1

INTRODUCTION

Chapter 2

THEORY AND CONCEPTS

Chapter 3

CONCEPT IMPLEMENTATION

Chapter 4

EXPERIMENT AND RESULTS—DIRECT DOWNCONVERSION

CHAPTER 1

INTRODUCTION

1.1 Science objective

Ice sheets and glaciers cover roughly 10% of the Earth's land surface area ([1], p. 1). Ice, both on land and in the sea, plays an important role in the continuous exchange of energy that takes place at the Earth's surface. Solar energy is reflected back into space by the ice, and this keeps the Earth's average global temperature lower. But if global warming were to occur, the melting of polar and glacial ice would mean that less solar energy is being reflected back. The Earth's average global temperature would then begin to rise. This rise would in turn melt more of the ice, and a reinforcing process take over, causing global warming. As a result of global warming, the sea level would rise and this rise would affect coastal development and wetland resources. However, sea ice does not affect sea level, because sea ice is floating on the ocean already and is in equilibrium with it ([1], p. 2). On the other hand, the Greenland and Antartic ice sheets (both of which are land ice), because of their huge sizes, have great potential for changing sea level. It is uncertain, however, whether the Greenland and Antartic ice sheets are growing or shrinking ([1], p. 2).

In addition to increasing the amount of melting, global warming would also increase the amount of precipitation in the polar regions. The reasons for this phenomenon are: a) warmer air carries more moisture than colder air; b) warmer water causes an increase in ocean evaporation; and c) more ocean area will be exposed to the atmosphere as a result of decreasing sea ice ([1], p. 2). Climate models have predicted

that sea-level rise along the Gulf coast could range from 8 to 20 in. in the next century [2].

Continuous monitoring of the ice sheets is needed to predict climate and sea level change. The observations would also help scientists better understand the relationship between climate change and the ice sheets. One such observation is ice sheet elevation change, and altimeters are important in measuring ice sheet elevation. Laser altimeters such as the Geoscience Lidar Altimeter System (GLAS) provide more accurate measurements over a wider area than radar altimeters ([1], p. 4).

1.2 Brief system description

The objective of this project is to develop a new class of laser radar or lidar that uses commercial off-the-shelf advanced fiber-optic components primarily for spaceborne altimeter application. The needed surface elevation measurement or range accuracy has been shown to be 10 cm. At the moment, most spaceborne lidars transmit short pulses with high peak power and low-pulse repetition frequency (PRF). A low-pulse repetition results in sparse spatial sampling along the sweep path of the satellite. Furthermore, the high transmit optical power will shorten the lifetime of the laser diode. The higher PRF gives us denser sampling.

Pulse compression, an RF signal processing technique, allows the use of lower peak transmit power while maintaining good receiver sensitivity. We will show that applying RF pulse compression further enhances the performance of the new class of radar. The transmitted signal, a gated CW optical carrier intensity modulated with a linear FM (chirp) RF signal [3], is launched into free space through a telescope. The concepts were built on work reported by Mullen at al. [4]. The wavelength used is 1319 nm to

enable the use of commercial fiber optic devices. At this wavelength, the reflectivity of snow and ice is increased as compared to a 1550 nm wavelength. An optical telescope is used as a receive aperture and couples the +backscattered signal into a single-mode fiber (SMF). A balanced photoreceiver is used for photodetection. The development and preliminary results of the fiber-optic-based laser radar that applies RF pulse compression and digital signal processing to improve receiver sensitivity and range measurement capabilities has been reported (IGARSS ’99 [5], ’00 [6], ’01 [7]).

To further improve the receiver sensitivity, we employed the use of a data acquisition system developed by Torry Akins of the University of Kansas through digital signal processing. The data acquisition system was originally developed for the Greenland Ice Sheet Measurement project [8].

1.3 Characteristics of prior laser altimeters

The GLAS is being developed by NASA for the Earth Science Project to map the topography of land, ocean and the polar ice sheets. The lidar will be incorporated into the NASA Ice, Cloud, and Land Elevation Satellite (ICESAT). Some key characteristics of the GLAS are summarized in Table 1.3.1. The peak transmit power is 15 MW. As a result, the high peak transmit power will shorten the lifetime of the laser diode. The satellite flies with three Q-switched Nd:YAG diode-pumped lasers.

A rough comparison between the GLAS system and the hybrid laser radar system is given in Table 1.3.2. We see that the same gain is achieved in the hybrid laser radar system with a lower peak power, as compared with the GLAS system. The 77 dB of receiver gain offsets the low transmitter power. Furthermore, the lidar we developed would have 1000 range samples/s , twenty five times that of the GLAS.

Table 1.3.1 Key GLAS characteristics.

Parameters	Specification
Wavelength	1064 nm
Orbit altitude	600 km
Receive aperture diameter	1 m
Pulse energy	75 mJ
Pulse power	15 MW
Pulse duration	5 ns
Pulse rate	40 per second
Lifetime	3 – 5 years
Laser footprint diameter	70 m
Range accuracy	10 cm

Table 1.3.2 Rough comparison of GLAS and hybrid laser radar system.

Parameter	***GLAS***	***Hybrid Laser Radar***	***Units***	***Difference***
Wavelength	1064	1319	**nm**	
Peak Power	$15x10^6$	0.15	**W**	
Peak Power	102	25	**dBm**	**- 77 dB**
Pulse Duration	5	200000	**ns**	
Transmitted Bandwidth	250	260	**MHz**	
Pulse Repetition Frequency	40	1000	**Hz**	**25 x**
Samples per Estimate	1	1	**--**	
Receiver Optical Gain	0	30	**dB**	**+ 30 dB**
Pulse Compression Gain	0	47.16	**dB**	**+ 47 dB**
Range Sample Rate	40	1000	**s^{-1}**	**25 x**
Range Accuracy	10	10	**cm**	

Some key characteristics of the breadboard hybrid 1319 nm laser radar with pulse compression, which we developed, are shown in Table 1.3.3.

Table 1.3.3 Hybrid laser radar with pulse compression characteristics.

Parameters	Specification
Wavelength	1319 nm
Peak power	15 dBm
Receive aperture diameter	5 in./127 mm
Optical amplifier gain	30 dB
Pulse duration	200 μs
Pulse rate	1000 per second
Pulse compression ratio gain	47 dB
Range accuracy	10 cm

We have developed and tested a breadboard hybrid laser radar system that requires low peak power and improved receiver sensitivity, which we obtained by applying RF pulse compression, digital signal processing, coherent detection and direct downconversion. The development of the hybrid laser radar system will be described in the chapters that follow.

CHAPTER 2

THEORY AND CONCEPTS

This chapter provides the theoretical and conceptual background for the development of the laser radar system. The sets of formulas used serve as performance predictions and act as the underlying principles as to how the system functions. The theories used are not new and include electromagnetic wave theories, communication theories and fiber optic theories.

2.1 Range accuracy formula

The range accuracy formula predicts the performance of the laser radar with regard to the detected signal-to-noise ratio (SNR).

The RMS range error of the detected target is given by the formula below [9, 10]:

$$\sigma_R = \frac{c}{2B\sqrt{2\,SNR}} \tag{2.1.1}$$

where σ_R is the overall range accuracy, which is bandwidth and signal-to-noise ratio dependent, and,

B = bandwidth of the transmit signal (Hz)

SNR = received signal-to-noise ratio

c = speed of light (3×10^8 m/sec).

Here, the requirement is that the SNR should be greater than 10. In other words, the above formula tells us the extent or margin of error of the target range. For example, if the transmitted bandwidth of the system is B = 260 MHz, and the SNR = 10, then the range accuracy is σ_R = 0.129 m. In other words, for the given parameters, the range

accuracy of the system is within an error margin of 0.129 m. Also, for a range accuracy $\sigma_R = 0.1$ m, the SNR required is then SNR = 16.64 = 12.2 dB.

2.2 Radar range equation

The microwave radar range equation is used to derive the received or return signal power and is governed by the equation below. The received signal power is ([9], p. 3):

$$P_R = \frac{P_T G_T}{4\pi R^2} \times \frac{\sigma}{4\pi R^2} \times \frac{\pi D^2}{4} \times \eta_{ATM}\ \eta_{SYS} \qquad (2.2.1)$$

P_R = received power at photodetector (W)

D = receive aperture diameter (m)

P_T = peak transmit power (W)

G_T = transmitter antenna gain = $\frac{4\pi}{\theta_T^2}$

θ_T = transmitter beamwidth = $\frac{K_a \lambda}{D}$ (far-field operation)

λ = wavelength (m)

K_a = aperture illumination constant

σ = effective target cross section (m^2)

R = distance from transmitter to target (m)

η_{SYS} = system loss factor

η_{ATM} = atmospheric loss factor.

Substituting the above definitions into (2.2.1), the radar range equation for a far field range of operation is shown here in (2.2.2) ([9], p. 3),

$$P_R = \frac{P_T \sigma D^4}{16 R^4 \lambda^2 K_a^2} \times \eta_{ATM}\ \eta_{SYS} \qquad (2.2.2)$$

The far-field (Fraunhofer) range is defined as $R > \frac{2D^2}{\lambda}$. For a radar with D = 0.15 m and operating wavelength of 1310 nm, the far-field distance is approximately 34 km. However, for our laboratory experiments, we usually operate in the near-field region. As a result, the transmitter beamwidth, θ_T, is modified for near-field range as shown in (2.2.3) ([9], p. 4).

$$\theta_T = \left[\left(\frac{K_a D}{R} \right)^2 + \left(\frac{K_a \lambda}{D} \right)^2 \right]^{1/2} \tag{2.2.3}$$

The effective target cross section is given by ([9], p. 5),

$$\sigma = \frac{4\pi}{\Omega} \rho_T A \tag{2.2.4}$$

Ω = scattering solid angle of target (sr), ($\Omega = \pi$ sr for a Lambertian target)

ρ_T = target reflectivity

A = target area illuminated (target normal to beam)

$A = \frac{\pi R^2 \theta_T^2}{4}$ (m^2)

For an extended target, (2.2.4) then becomes ([9], p. 6)

$$\sigma_{EXT} = \pi \rho_T R^2 \theta_T^2 \tag{2.2.5}$$

However, when considering the assumption that the target is an extended Lambertian target (i.e., the area illuminated by the transmitter is smaller than the target itself for an extended target) and that the target is in the near field, the beamwidth θ_T must be modified. A Lambertian target has a surface that scatters uniformly in all directions. A specular target (a mirror, for example) is defined as a target that has an angle of reflection equal to the angle of incidence [11]. Two target classifications are illustrated in Figure 2.2.1.

Specular target, $\theta_i = \theta_r$ Ideal Lambertian (diffuse) target

Figure 2.2.1 Specular versus diffuse target.

Substituting (2.2.3) and (2.2.5) into (2.2.1) results in ([9], p. 6),

$$P_R = \frac{P_T \rho_T \pi D^2}{(4R)^2} \times \eta_{ATM}\ \eta_{SYS} \tag{2.2.6}$$

Thus, the return radiation has a range-squared dependency.

2.3 Square-law photodetection and balanced photodetection

Photodetection is accomplished by using a reverse-biased PIN junction diode. The incident photons on the junction are absorbed by the semiconductor, and electron-hole pairs are generated. In the strong electric field created by the reverse biasing of the diode, the electron-hole pairs separate and move in opposite directions. Thus, photocurrent is generated. The laser light can be expressed as an electromagnetic field as shown in (2.3.1), and a photodetector output current, in terms of the incident electromagnetic field is shown in (2.3.2) ([12], p. 296).

$$E_{opt} = A\cos(\omega_c t) \tag{2.3.1}$$

$$I = \Re E_{opt}^2 \tag{2.3.2}$$

where

E_{opt} = optical electromagnetic field (V/m)

$\Re$ = responsivity of photodiode (A/W)

I = photodetector current output (A)

ω_c = optical frequency corresponding to the wavelength of the laser (rad)

A = amplitude (V/m)

The responsivity, $\Re$, corresponds to the photodiode's conversion of optical power into electrical current. Hence, the term "square-law photodetector" is used to describe photodectors since it is a squared relationship between the optical electromagnetic fields and the detected current.

In coherent detection, the signal and the optical LO are combined in a fiber coupler. The output of the fiber coupler is converted into photocurrents by a balanced photodetector. A balanced photodetector has two photodiodes connected front to back, and the generated photocurrents of the two photodiodes are subtracted. Figure 2.3.1 illustrates the balanced photodetector setup.

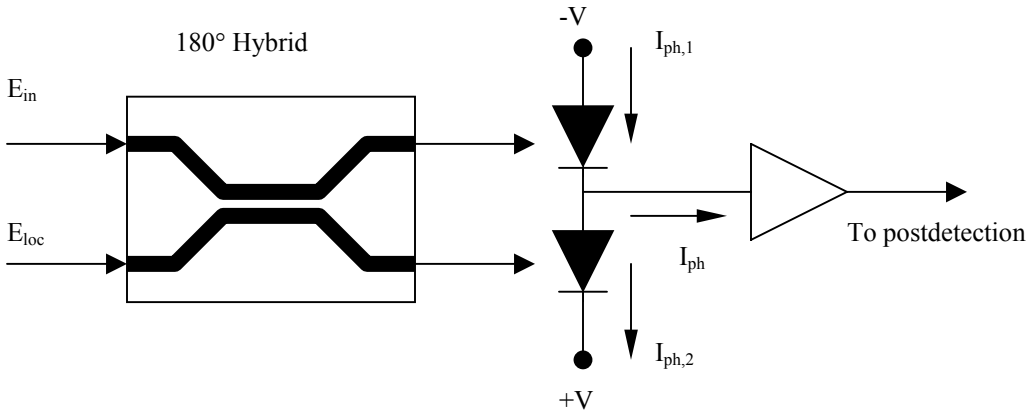

Figure 2.3.1 Balanced photodetection.

The coupler used to mixed the LO and the signal optically is a 180° hybrid coupler. The coupler induces a 180° phase shift between the two output ports of the hybrid coupler. The hybrid coupler can be represented by a 2×2 matrix as follows ([13], p. 757):

$$\overline{H} = \frac{1}{\sqrt{2}} e^{j\theta} \begin{bmatrix} 1 & 1 \\ 1 & -1 \end{bmatrix} \qquad (2.3.3)$$

Then, the outputs of the four-port 180° hybrid coupler can be expressed as electrical fields ([13], p. 757):

$$\begin{bmatrix} E_1 \\ E_2 \end{bmatrix} = \overline{H} \begin{bmatrix} E_{in} \\ E_{loc} \end{bmatrix} \tag{2.3.4}$$

where E_1 and E_2 are the output fields. E_{in} is the input signal field and E_{loc} is the LO field.

Following (2.3.3) and (2.3.4), the two outputs of the 180° hybrid coupler can be expressed as ([13], p. 759):

$$E_1 = \tfrac{1}{\sqrt{2}}\left(E_{in} + E_{loc}\right) \tag{2.3.5}$$

$$E_2 = \tfrac{1}{\sqrt{2}}\left(E_{in} - E_{loc}\right) \tag{2.3.6}$$

Then the outputs of the two photodiodes in the balanced photodetector, in terms of power, are ([13], pp. 759 – 760):

$$I_{ph,1} = \frac{1}{2}\Re\left\{P_{in} + P_{loc} + 2\sqrt{P_{in}P_{loc}}\cos(\gamma)\cos\left[(\omega_{in} - \omega_{loc})t + \phi(t)\right]\right\} \tag{2.3.7}$$

$$I_{ph,2} = \frac{1}{2}\Re\left\{P_{in} + P_{loc} - 2\sqrt{P_{in}P_{loc}}\cos(\gamma)\cos\left[(\omega_{in} - \omega_{loc})t + \phi(t)\right]\right\} \tag{2.3.8}$$

where ω_{in} and ω_{loc} are the angular frequencies of the incident signal and the LO in rad/s, respectively. The arbitrary phase difference between the incident signal and the LO is $\phi(t)$. In the $\cos(\gamma)$ term, γ represents the mismatch in polarization states between the LO and the incident signal. Then, at the output of the balanced photodetector, the difference between the two photocurrents is:

$$I_{ph} = 2\Re\sqrt{P_{in}P_{loc}}\cos(\gamma)\cos\left[(\omega_{in} - \omega_{loc})t + \phi(t)\right] \tag{2.3.9}$$

One major advantage of using balanced photodetectors is that the relative intensity noise (RIN) is removed. RIN is the intensity fluctuation at a laser diode output, and it is caused by random spontaneous emission of photons ([13], p. 246). RIN is directly proportional to the optical signal power incident on the photodiode. A high-powered LO

is needed for efficient coherent detection, and, since RIN is proportional to the incident light power, the RIN will be high. As (2.3.9) suggests, the dominant term, which is the DC LO (or P_{loc}) term, is subtracted off. Hence, RIN is eliminated.

Equation (2.3.9) shows that the use of the balanced detector removes the direct detected signal, P_{in}. As a result, any overlapping in the frequency domain between the coherently detected signal and the direct detected signal is avoided. Consider an amplitude-modulated double-sided band linear chirp with an optical carrier frequency of f_c = 600 MHz, for example. Assume that the chirp bandwidth is 300 MHz and the start frequency is 100 MHz. Let the LO be the same optical carrier used in the AM signal, but downshifted by an offset of 600 MHz. The mixing of the downshifted LO and the AM signal will produce a chirp signal with an IF of 600 MHz center frequency. However, as (2.3.7), (2.3.8) and (A1.5) from the receiver analysis show, the directly detected signal P_{in} is also present. As Figure 2.3.2 illustrates, the directly detected signal will overlap with the desired coherently detected signal.

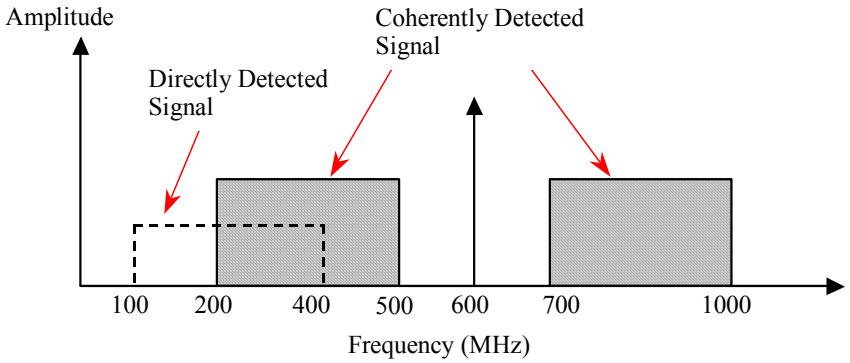

Figure 2.3.2 Overlapping of directly detected signal and coherently detected signal.

The overlap between the directly detected signal and the coherently detected signal becomes a major problem if the incident signal power P_{in} is large in comparison to the LO power. The difference between the two photodiode currents eliminates the common term, P_{in}. As a result, the directly detected signal is eliminated. In coherent detection

applications, the use of balanced photodetectors has its advantages. As mentioned, the balanced detector removes unwanted direct detection signals and RIN is eliminated.

2.4 Noise characteristics

In every electrical and optical system, the noise factor has to be taken into consideration. There are several types of noise sources in fiber optics – shot noise, thermal noise, and dark current. Shot noise is due to the random combination of the electron-hole-pair within the active junction of the photodiode. It can be treated as additive white noise and has a Gaussian random distribution with zero mean. The time-domain shot noise is given as ([13], p. 237),

$$i_{shot}(t) = i_{ph}(t) - I_{ph} \tag{2.4.1}$$

where $i_{ph}(t)$ = photocurrent, I_{ph} = time average photocurrent.

The power spectral density is then given by ([13], p. 238),

$$S_{shot}(\omega) \cong q(I_{ph} + I_d) \tag{2.4.2}$$

where ω is the angular frequency, q is the electron charge (1.6×10^{-19} C), and I_d is the dark current. But, since we operate in a narrow bandwidth, the Gaussian shot noise will be band limited and the noise power over bandwidth B is ([13], p. 238):

$$\overline{i_{shot}^{\,2}} \cong 2q(I_{ph} + I_d)B = 2q(\Re P_{sig} + I_d)B \tag{2.4.3}$$

Another significant source of noise is thermal noise. Thermal noise is also white Gaussian distributed noise. The band-limited average thermal noise power is calculated as ([13], p. 240),

$$\sigma^2 = 2kTB \tag{2.4.4}$$

and average thermal noise current is given by ([13], p. 241):

$$\overline{i^2_{\,thermal}} = \frac{4kTB}{R} \tag{2.4.5}$$

where k = Boltzmann's constant (1.38×10^{-23} J/K), R = resistance (Ω), and T = temperature (K).

In coherent detection systems, a high-powered optical LO is needed for detecting weak return signals. However, the high LO power will also increase shot noise. In our breadboard laser radar system, shot noise is the dominant source of noise. External noise, dark current, and thermal noise will still be present but are negligible in comparison to the significantly larger shot noise power. RIN, as stated earlier is removed by the use of the balanced photodectector. Hence, we say that the laser radar is operating as a shot noise-limited system.

2.5 Heterodyne detection and SNR formulation

Coherent detection is divided into two types: homodyne and heterodyne. For example, to detect the signal with a passband signal $m(t)\cos(\omega_c t)$, the received signal is multiplied with a local oscillator frequency (LO) $\cos(\omega_{LO} t)$. The product of the two frequencies is then ([13], p. 754):

$$m(t)\cos(\omega_c t)\times\cos(\omega_{LO} t) = \tfrac{1}{2}m(t)\cos\{(\omega_c-\omega_{LO})t\} + \tfrac{1}{2}m(t)\cos\{(\omega_c+\omega_{LO})t\} \quad (2.5.1)$$

Let $\omega_{IF} = \omega_c - \omega_{LO}$, where IF = intermediate frequency.

The above equation shows the mathematical representation of heterodyne detection. Heterodyne detection shifts the signal to an intermediate frequency and preserves the double-sided bands. If $\omega_{LO} = \omega_c$, then the detection process is called homodyne, where $\omega_{IF} = 0$. Homodyne detection shifts the detected signal down to baseband. As a result, the bandwidth of the detected signal is half that of the heterodyne detected signal.

Heterodyne detection is the same, both in the optical domain and in the RF domain. Both use the mixing of a local oscillator frequency with the detected signal to obtain an intermediate frequency (IF). In the example above the IF created in heterodyne detection would be $\omega_{IF} = |\omega_c - \omega_{LO}|$.

In optical communications, heterodyne detection is done via optical mixing with devices, such as an optical coupler. The received signal is mixed with a local oscillator frequency as shown below in Figure 2.5.1.

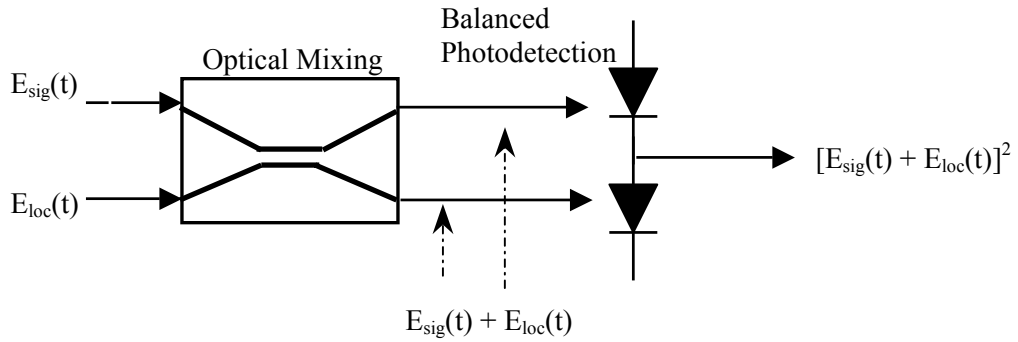

Figure 2.5.1 Coherent detection with balanced photodetection.

The signal-to-noise ratio at the photodiode output is defined as:

$$\text{SNR} = \frac{\text{Signal power}}{\text{Total noise power}} \tag{2.5.2}$$

Therefore, by substituting (2.4.4) for shot noise contribution and (2.4.5) for thermal noise contribution into (2.5.2), the SNR in heterodyne detection is ([12], p. 296; [13], p. 761),

$$\text{SNR}_{coh} = \frac{\left(2\Re\sqrt{P_{sig}P_{lo}}\right)^2}{2B\left[\Re q\left(P_{sig} + P_{lo}\right) + I_d + 2kT/R\right]} \tag{2.5.3}$$

Here we can ignore I_d because we are assuming that shot noise and thermal noise are much greater than I_d. Then, (2.5.3) becomes,

$$\mathrm{SNR}_{\mathrm{coh}} = \frac{\left(2\Re\sqrt{P_{\mathrm{sig}}P_{\mathrm{lo}}}\right)^2}{2B\left[\Re q\left(P_{\mathrm{sig}} + P_{\mathrm{lo}}\right) + 2kT/R\right]} \tag{2.5.4}$$

Similarly, we can derive the SNR for incoherent or direct detection as shown in (2.5.5) ([12], p. 296).

$$\mathrm{SNR}_{\mathrm{incoh}} = \frac{\left(\Re P_{\mathrm{sig}}\right)^2}{2B\left(\Re q P_{\mathrm{sig}} + 2kT/R\right)} \tag{2.5.5}$$

Here is an example to illustrate the amount of gain obtained from using a coherent detection scheme.

Let P_T = 1 W, P_{LO} = 1 mW,

Range = 600 km, R = 50 Ω,

D = 0.127 m (5 in. aperture diameter), T = 273 K,

ρ_T = 1, $\Re$ = 1 A/W,

η_{ATM} = 0.3, B = 800 MHz (photodetector

η_{SYS} = 1, bandwidth).

Then from (2.2.6), $P_R = 2.64\times10^{-15}$ W. Substituting $P_{sig} = P_R$ into (2.5.5), $SNR_{incoh} = 2.89\times10^{-17}$ W or -165 dB, and substituting P_{LO} and $P_{sig} = P_R$ into (2.5.4), we get $SNR_{coh} = 2.13\times10^{-5}$ W or -47 dB. There is an increase of about 118 dB in signal-to-noise ratio in the coherent detection system in comparison to the incoherent system.

2.6 Optical coherence

There are two types of coherence we need to consider – spatial and temporal coherence. Spatial and temporal coherence of an electromagnetic wave are determined by the time or spatial interval over which an electromagnetic wave is in phase with itself.

Both coherence types can be expressed in terms of the laser source bandwidth, ΔF. The period where the electromagnetic wave is in phase with itself is determined by the equation ([9], p. 34)

$$\Delta t = 1/\Delta F \qquad (2.6.1)$$

and temporal coherence is related to spatial coherence in this relationship ([9], p.24)

$$\Delta R_c = c\Delta t = c/\Delta F \qquad (2.6.2)$$

Coherent single-mode laser sources tend to exhibit high spectral purity and therefore exhibit narrow linewidths and long coherence times. The round trip coherence distance is given by

$$\Delta R_c = c/2\Delta F \qquad (2.6.3)$$

For example, if the laser linewidth is given as 5 kHz, then $\Delta R = 3\times10^8/2\times5000$ or 30 km. The linewidth requirement limits our system to measure only over 30 km in range accurately. However, a phase-locked laser source could have an even narrower line-width.

2.7 Pulse compression

Two important factors determine the design of laser radars. The first is SNR, which is determined by the peak transmit pulse duration or pulse width. The longer the pulse width and the higher the transmit power, the larger the SNR. For the sake of discussion, consider a pulse without any modulation. The bandwidth of the transmit pulse is the reciprocal of the transmit pulse duration. However, to achieve good range accuracy, a large bandwidth is required as shown by (2.1.1). Range accuracy is the second factor that determines the design of laser radars. As mentioned in Chapter 1, the lidar used onboard ICESAT transmits short pulses with peak power of 15 MW. The short pulse and high peak power ensures good SNR and range accuracy. However, high peak power shortens

the life of the laser diodes. So, to solve this problem, a pulse with lower peak transmit power and longer duration is used. This is illustrated in Figure 2.7.1. Figure 2.7.1(a) shows a short pulse with a high peak transmit power, and Figure 2.7.1(b) shows a long pulse with a lower peak transmit power. Although the peak transmit powers and the pulse durations are different, the areas under the curves, which gives the energy of the pulses, are the same. If both their areas are the same, the SNR, which can be thought of in terms of the ratio of the transmitted pulse energy and noise energy, will also be the same. However, transmitting a longer pulse will decrease the range accuracy.

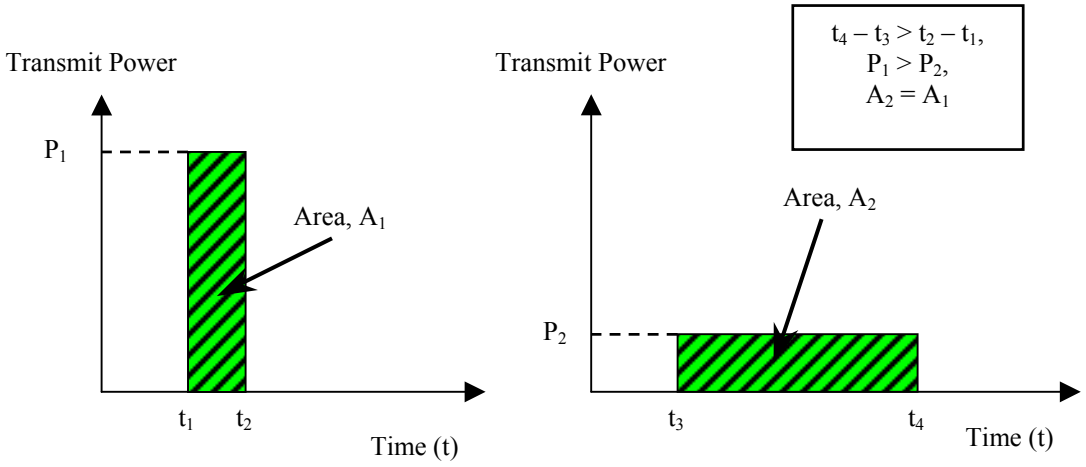

Figure 2.7.1 (a) Short pulse, high peak transmit power.

Figure 2.7.1 (b) Long pulse, lower peak transmit power.

Figure 2.7.1 Comparison of long and short transmit pulses.

This dilemma of transmitting a pulse short enough for good range accuracy, and yet long enough for a sufficiently high SNR, is resolved by using pulse compression. Pulse compression is achieved by modulating a short transmit pulse with a linear frequency chirp (linear FM) ([14], p. 287; [15], p. 163).

Pulse compression involves the transmission of a long coded pulse and the processing of the return echo signal to obtain a relatively narrow pulse. This allows for

the generation of a long pulse while avoiding the use of high peak power. Pulse compression is obtained by modulating the transmitted pulse with sufficient pulse duration. This provides the necessary average power with the appropriate peak power. The received signal is then "compressed" by the demodulation process ([14], p. 287; [15], p. 163).

There are several methods of modulating the pulse – linear frequency modulation (chirp), binary phase modulation, and polyphase modulation ([14], p. 288). Here we are only going to discuss the linear frequency chirp modulation scheme. A chirp is created when the frequency of the transmitted pulse is incremented at a constant rate from the start of the pulse to the end of the pulse. In a laser radar system, the chirp waveform is imprinted on an optical carrier before transmission, using intensity modulation.

The equation that describes a chirp waveform is given by

$$v(t) = \sin\left\{ 2\pi\left(f_o t + 0.5kt^2 + \phi_o\right)\right\}, \quad 0 \le t \le T \tag{2.7.1}$$

where k is the linear chirp rate = B/T (Hz/s), T is the pulse duration, f_o and ϕ_o are the starting frequency and phase, respectively.

The relationship between linear chirp, detected frequency, and the delay time can be established through the derivation below.

Let f_o be the start chirp frequency. The instantaneous change in frequency can be expressed as

$$f(t) = f_0 + \frac{B}{T}t \tag{2.7.2}$$

where k = B/T, and

$$v(t) = \cos\left(2\pi \int f(t)dt + \phi_o\right) \tag{2.7.3}$$

$$v(t) = \cos\left\{2\pi\left(f_o t + \frac{Bt^2}{2T} + \phi_o\right)\right\} \tag{2.7.4}$$

The return signal with delay τ is

$$v(t-\tau) = \cos\left\{2\pi\left(f_o(t-\tau) + \frac{B(t-\tau)^2}{2T} + \phi_r\right)\right\} \tag{2.7.5}$$

where ϕ_r = random phase of return signal. Then, by mixing and thus beating the return signal with an original version of itself, we obtain

$$v(t)v(t-\tau) = \cos\left\{2\pi\left(f_o t + \frac{Bt^2}{2T} + \phi_o\right)\right\}\cos\left\{2\pi\left(f_o(t-\tau) + \frac{B(t-\tau)^2}{2T} + \phi_o\right)\right\} \tag{2.7.6}$$

and after low-pass filtering the beat signal,

$$s(t) = v(t)v(t-\tau) = \frac{1}{2}\cos\left(2\pi f_o \tau + \frac{\pi B t \tau}{T} + \frac{\pi B \tau^2}{T}\right) \tag{2.7.7}$$

By examining the terms within the cosine, we see that the only term that is time varying is $\pi B\tau t/T$, and hence we have a sinusoidal term of a single frequency given by

$$f_R = \frac{B}{T}\tau \tag{2.7.8}$$

where the round-trip delay $\tau = 2R/c$ and the range resolution is

$$\Delta R = \frac{c}{2B} \tag{2.7.9}$$

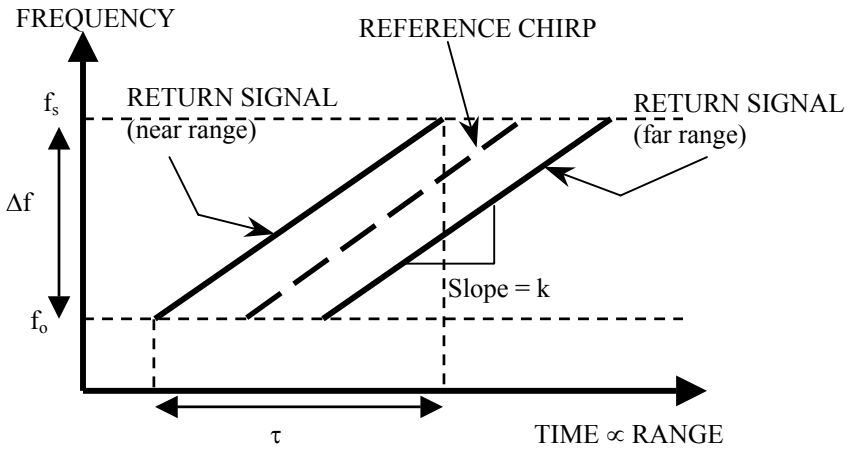

Figure 2.7.2 Chirp waveform frequency and time relationship (adapted from [16], p. 11).

The figure above is another way of thinking about dechirping or decoding a return chirp signal. When the return signal is mixed with the reference signal or also known as the local oscillator (LO), the parallelogram of Figure 2.7.2 is transformed into another parallelogram shown below in Figure 2.7.3. The resultant signal is a pure sinusoid of a significantly lower frequency, which we will call f_1 for a far-range target and f_2 for a near-range target [16].

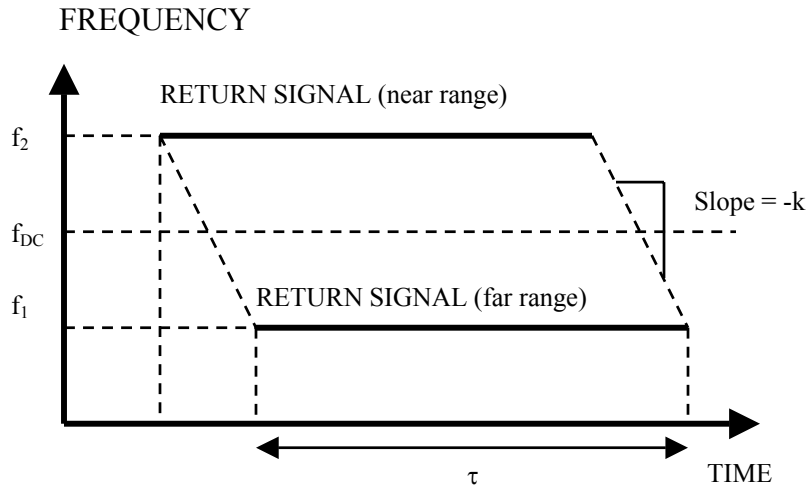

Figure 2.7.3 Dechirped signal frequency vs. time relationship (adapted from [16]).

Pulse compression is achieved by passing the echo or the received frequency chirp signal through a matched filter receiver. The filter will introduce a delay that decreases linearly with the frequency at the same rate that the frequency of the chirp is increasing. Because of the matched delay, the highest frequency component of the chirp, which was transmitted at the trailing end, takes less time to pass through the filter than the leading end of the chirp. Hence, successive portions of the chirp tend to "bunch up", causing the amplitude of the pulse to increase and the width to decrease. As a result, the pulse has been compressed ([15], p. 163-168).

In Figure 2.7.3, the diagram shows that the dechirped signal has a single frequency (a sinusoid), f_1 or f_2. As a result, the range of a target can be determined by the frequency difference between the offset frequency f_{DC} and the dechirped frequency f_1 or f_2. The slope $-\boldsymbol{k}$ is then the chirp rate in Frequency/Time (e.g., MHz/μs). Figure 2.7.4. illustrates the compressed and uncompressed pulse in the time-domain.

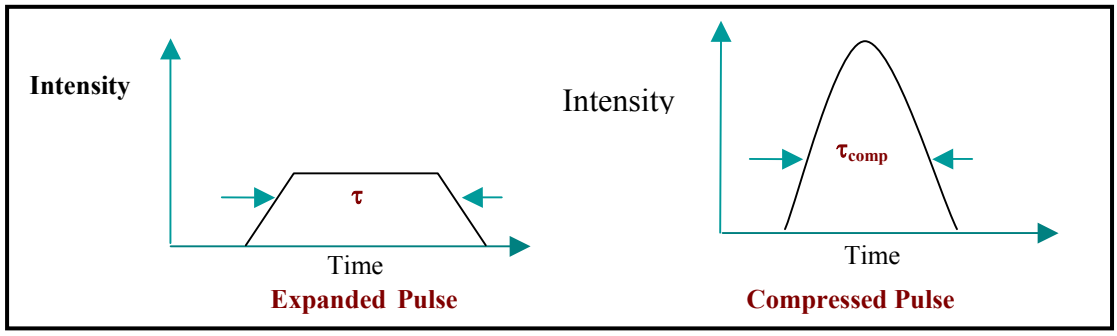

Figure 2.7.4 Comparison of pulse with and without compression.

The advantage we have here is transmission of a low-amplitude pulse of longer duration; instead of using high-peak transmit power and short-duration pulses. This helps prolong the life of the laser diode, and lower the high-peak transmit power requirement.

The range of a target can be determined by stretch radar decoding of the chirp echo or the received chirp signal. In stretch radar decoding, the echo is mixed with an original version of the transmitted chirp (dechirping). As can be seen from Figure 2.7.2, the return signal echo has a time delay with respect to the reference chirp. This time delay is proportional to the range of a target.

The pulse compression ratio (i.e., the ratio of the uncompressed pulse width, τ, to the compressed pulse width, $\tau_{comp)}$, is given by ([14], p. 287; [15], p. 168)

$$\text{Pulse compression ratio} = \frac{\tau}{\tau_{comp}} = \frac{\Delta F}{\Delta f} \tag{2.7.10}$$

where $\Delta f = 1/\tau$, and ΔF is the bandwidth of the chirp. The pulse compression ratio can also be expressed as the time-bandwidth product ([15], p. 168)

$$\text{Pulse compression ratio} = \tau \Delta F \tag{2.7.11}$$

and ([15], p. 168)

$$\tau_{comp} = \frac{1}{\Delta F} \tag{2.7.12}$$

So, for a system with ΔF = 260 MHz, τ = 200 μs, then Δf = 1/(200 μs) = 5 kHz, τ_{comp} = 1/(260 MHz) = 3.85 nsec, and the pulse compression ratio τ/τ_{comp} is 52000 or 47 dB. As a result, the detected signal power will be 47 dB higher in a pulse compression system than a radar system that uses a simple short pulse with no pulse compression. Furthermore, the chirp bandwidth and the pulse width can be manipulated to increase the compression ratio and thus increase the overall gain of the receiver. Table 2.7.1 shows that as the bandwidth is doubled, the gain also doubles or increases by 3 dB. Similarly, doubling the pulse width, doubles the gain.

Table 2.7.1 Increasing receiver gain through chirp bandwidth and pulse duration.

ΔF [MHz]	τ [μs]	Δf [kHz]	τ_{comp} [s]	Pulse Compresssion Ratio	Gain (dB)
100	40	25	1.00E-08	4000	36.0
100	80	12.5	1.00E-08	8000	39.0
100	160	6.25	1.00E-08	16000	42.0
200	40	25	5.00E-09	8000	39.0
400	40	25	2.50E-09	16000	42.0
800	40	25	1.25E-09	32000	45.1

2.8 Envelope detection

Amplitude modulation (AM) has been widely used in the radar world and in radio communications. An AM signal is defined as "a process in which the amplitude of the carrier wave is varied about a mean value, linearly with the baseband signal" ([17], p. 122). The transmitted AM signal consists two sidebands and a carrier in the center of the two.

Coherent receivers are especially sensitive to changes in the received signal phase and frequency relative to the local oscillator. These changes occur as the return signal propagates through the air. Envelope detection discards these changes, which are contained in the optical phase of the signal.

During demodulation, envelope detection strips away the carrier, which contains any phase and frequency fluctuation. This is shown in A2.4 in the analysis given in Appendix 2.

In amplitude modulated systems, the message or necessary information is contained within the sidebands centered about the carrier frequency. An amplitude-modulated system, in the time domain, can be described by the ([17], p. 122):

$$s(t) = A\left[1 + \beta m(t)\right]\cos\omega_c t \qquad (2.8.1)$$

where A = amplitude of the AM signal, m(t) = message or the envelope, β = modulation index, and ω_c = carrier angular frequency. The spectrum of the AM signal is given as ([17], p. 124):

$$S(f) = \frac{A}{2}\left\{\left[\delta(f - f_c) + \delta(f + f_c)\right] + \beta\left[M(f - f_c) + M(f + f_c)\right]\right\} \qquad (2.8.2)$$

where δ = delta function and M(f) = Fourier transform of m(t). Figure 2.8.1 shows the spectrum of the AM signal. The signal is a chirp with start frequency f_1 and stop frequency f_2.

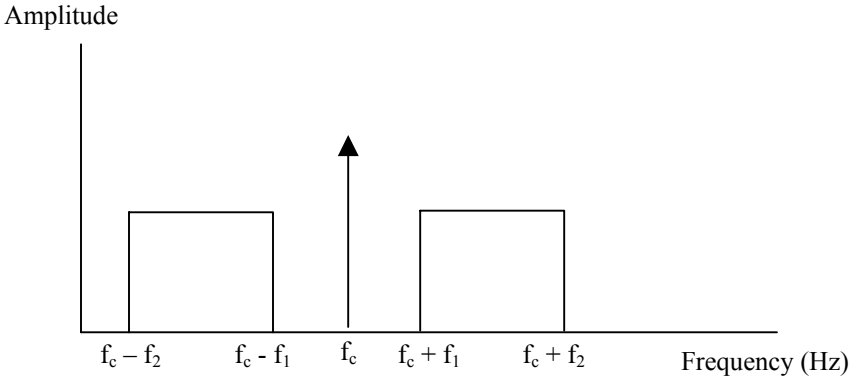

Figure 2.8.1 Double-sided AM signal.

At the detection end, the signal needs to be demodulated to regain the information. This information recovery can be done through envelope detection or direct frequency down-conversion. Envelope detection, simply put, is recovery of the waveform of the original message; and frequency down-conversion, as its name suggests, shifts the AM signal frequency back down to the original waveform frequency band.

As mentioned earlier, the envelope detection scheme is superior in the sense that it rids the system of optical phase fluctuations. However, more hardware is needed since

the photodetected signal will have to undergo a frequency up-conversion process in order for envelope detection to work, and envelope detectors tend to have about 7 – 10 dB noise factor and conversion loss. An envelope detector changes a Gaussian probability density function (PDF) noise-limited system with a zero mean into a Rayleigh PDF with non-zero mean, as shown in Figure 2.8.2 ([18], p. 42).

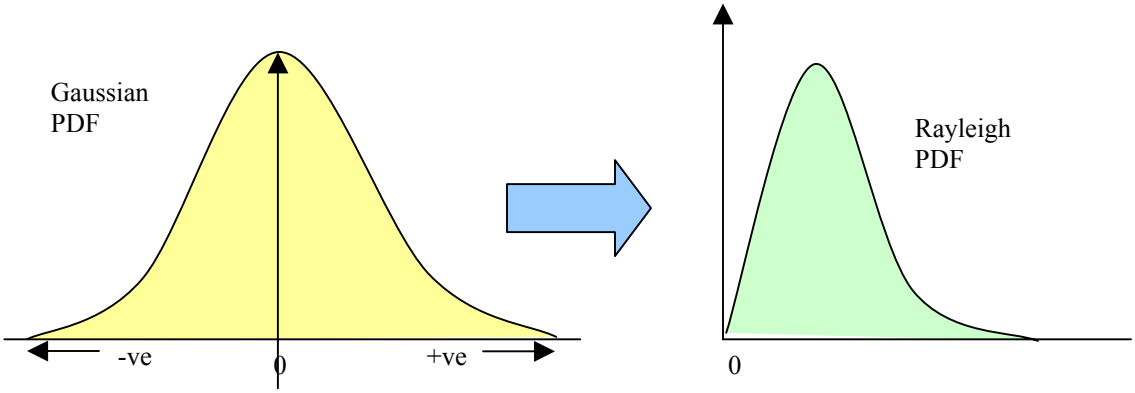

Figure 2.8.2 Envelope detector changes the noise characteristics.

Therefore, this non-zero Rayleigh distributed noise will give rise to a DC offset in the time-domain noise. A frequency downconversion scheme is superior in that the Gaussian noise characteristic is preserved as the noise is passed through the frequency down-converter.

2.9 Coherent integration and incoherent integration

Transmission of M coherent or synchronous pulses allows for coherent integration, with the condition that the return pulses are in-phase with one another. Coherent integration is done prior to detection. At the detector end, coherent processing can be thought of as adding up M number of return signal pulses coherently and then averaging the sum of the pulses. It is important that synchronicity is maintained from one pulse to another while adding up the pulses. The advantage of coherent processing is that the noise power can be reduced. Therefore, the band-limited noise power is ([18], p. 45),

$$N = N_o f_B = \frac{N_o}{\tau_r} \tag{2.9.1}$$

where N = band limited noise power of the system [W],

N_o = total noise power [W/Hz],

f_B = bandwidth of receiver [Hz].

Also, let M be the number of pulses transmitted with τ_r pulse duration for each pulse and N_o be the total noise power per Hertz. Then, $M\tau_r$ is the duration of M pulses transmitted. Therefore, we can rewrite the above equation for the coherently integrated M number of pulses as ([18], p. 45),

$$N_M = \frac{N_o}{M\tau_r} = \frac{N}{M} \tag{2.9.2}$$

We see that the noise power has been decreased by a factor of M. From (2.9.2), the signal power for one pulse is the same for M number of pulses integrated coherently. It is only the noise power that has been lowered by a factor of M. The strict condition applies that coherency has to be maintained throughout propagation and reflection. In addition to that, the initial phase of the signal must be constant. Another less optimal approach than coherent integration is incoherent integration ([18], p. 45).

After envelope detection, incoherent integration can be done on M return signal pulses. Using incoherent integration, a less stringent scheme can be applied to reduce the noise power and hence increase the SNR, albeit incoherent integration is a less optimal technique. A square-law detector (i.e., a detector that has a quadratic relationship between the input power and output power) is used in the process. A linear detector can also be used, but there are no integration performance differences in using either the linear detector or the square-law detector. For a system transmitting M pulses, the improvement

in SNR is by a factor of √M when incoherently integrating M pulses. This comes from the fact that, with incoherent integration, the use of downconversion technique is necessary to compensate for the arbitrary return signal phase. As such, this method of signal processing will be discussed next ([18], pp. 45 - 47).

2.10 In-Phase and Quadrature Signal Processing

Atmospheric and environmental changes, polarization effects, and laser source frequency drift cause fluctuation in the optical signal phase. As a result, the detected signal will fluctuate, especially when coherent detection is involved. In order to solve this problem, in-phase (I) and quadrature (Q) signal processing is employed. I and Q signal processing is simply the sampling of the in phase and the 90° phase-shifted component of the RF return signal. Figure 2.10.1 illustrates the use of I and Q sampling procedure ([18], p. 203).

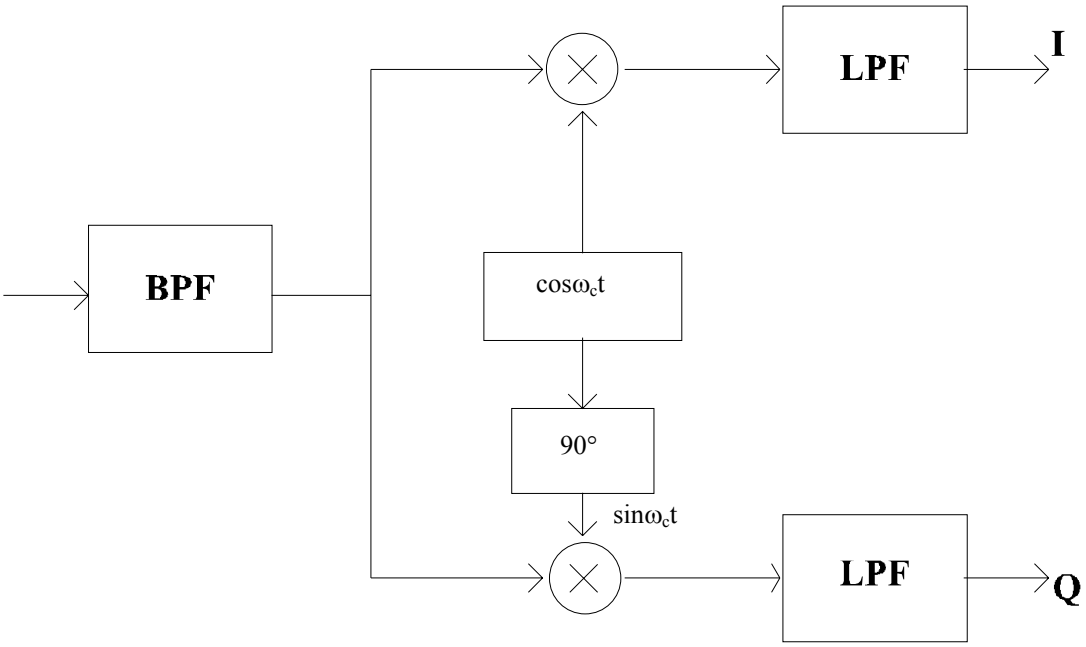

Figure 2.10.1 I & Q Detector.

If the signal input to the band-pass filter of the I and Q detector is ([18], p. 203),

$$s(t) = p(t)\cos\left[(\omega_c t) + \phi(t)\right] \tag{2.10.1}$$

where p(t) is the envelope pulse and $\phi(t)$ is the arbitrary phase of the return signal. Then the signal s(t) is multiplied by the sine and cosine signals of the same frequency. The outputs at the lowpass filters of the I and the Q channel are ([18], p. 204),

$$I(t_n) = \tfrac{1}{2} p(t_n)\cos\left[\phi(t_n)\right] \tag{2.11.2}$$

$$Q(t_n) = \tfrac{1}{2} p(t_n)\sin\left[\phi(t_n)\right] \tag{2.11.3}$$

where t_n is the period when the sampling of each pulse is taking place. The analog-to-digital system that does the sampling function has to be synchronous to the transmission pulse repetition rate. The low-pass filters are such that they block out twice the carrier frequency. From s (2.10.2) and (2.10.3), we see that if the phase term $\phi(t)$ fluctuates with time, one channel may go to zero whereas the other is at a maximum. After digitization of the samples collected from both channels, the samples can be treated as amplitudes or voltages. Hence, we can square and sum up both the channels to regain the signal envelope. Equation (2.11.4) summarizes this summation process for each pulse ([18], pp. 204 – 206),

$$p(t_n) = \left[I^2(t_n) + Q^2(t_n)\right]^{1/2} \tag{2.11.4}$$

In the same way, we can take the Fourier transform of the time domain I(t) and Q(t) outputs and sum them up.

$$P(f_n) = \left[I^2(f_n) + Q^2(f_n)\right]^{1/2} \tag{2.11.5}$$

This I and Q detection process, together with incoherent detection, will increase the SNR of the detected signal, and at the same time rid the system of SNR fluctuation due to the optical phase uncertainty.

CHAPTER 3

CONCEPT IMPLEMENTATION

After having developed the theory to predict and analyze the performance of the laser radar system, the concepts are ready to be put to the test. Chapter 3 discusses the hardware used and the implementation of the concepts and theories of the laser radar. The bread-boarding implementation of the laser radar system is shown in Figure 3.1.1 on the next page.

The following sections describe the transmitter part of the laser radar system, which consists of the laser source, the optical modulator, optical amplifier, the free-space optics, and then the transmission of the signal. The individual RF and fiber optic component parts used are standard, off-the-shelf industrial devices and are readily available commercially.

3.1 Transmitter—Single-mode laser

The heart of the laser radar system is the laser source. The laser source used is a single-mode, diode-pumped, fiber-coupled, non-planar ring laser from Lightwave® Electronics. Table 3.1.1 gives the specification of the laser source.

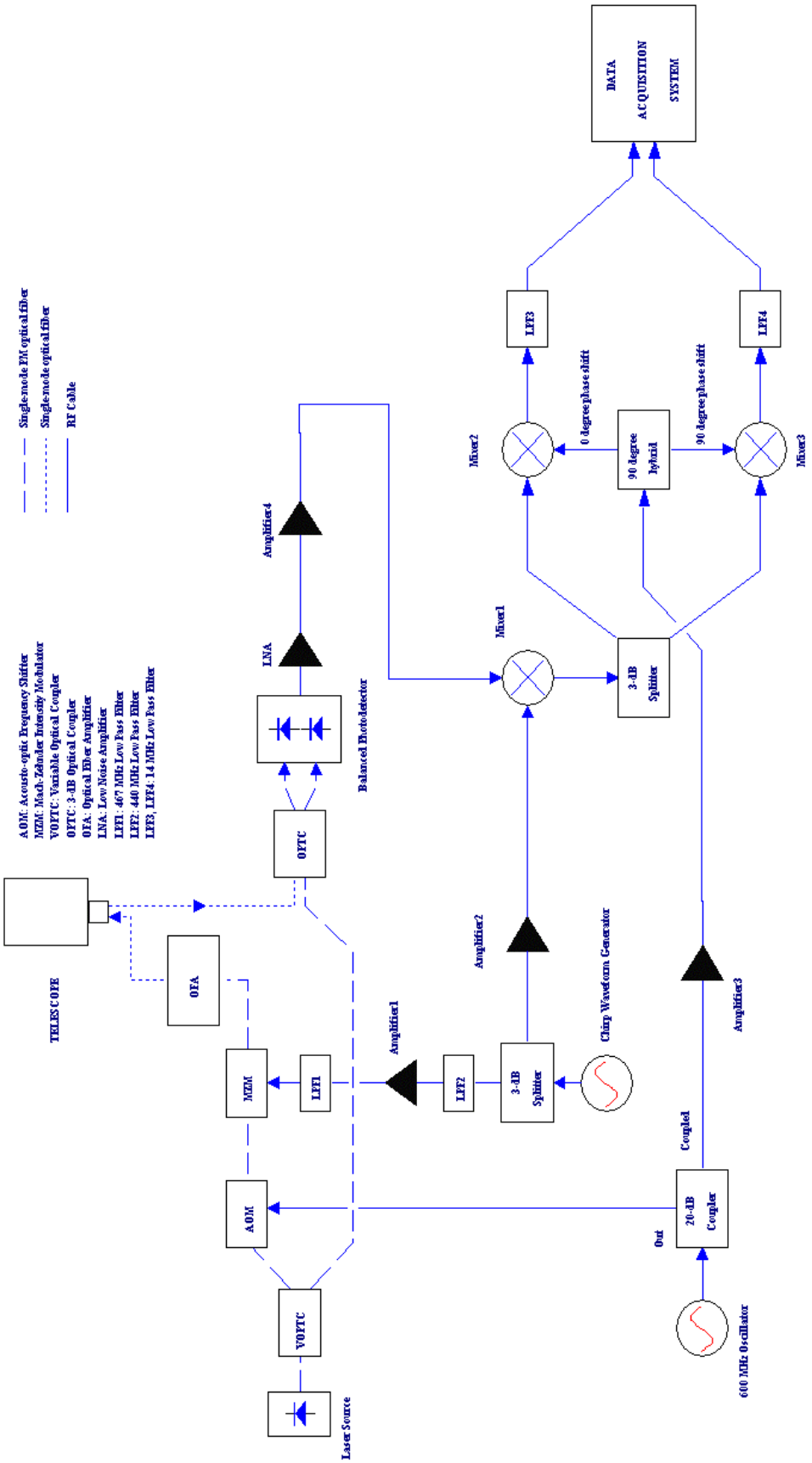

Figure 3.1.1 Block diagram of the laser radar breadboard implementation.

Table 3.1.1 Laser source specifications.

Model Number	125-1319-100
Wavelength	1319 nm
CW maximum output power	100 mW
Spatial mode	TEM_{00}
Longitudinal mode	Single frequency
Frequency stability: Linewidth Jitter Drift, at constant temperature	 <5 kHz/msec <200 kHz/sec <50 MHz/hour
Power stability: Amplitude noise (10 Hz to 2 MHz) Power drift	 0.05 % rms $< \pm$ 5%/8hours

As mentioned in the previous chapter, frequency stability and laser linewidth play an important part in the detection process. Any shift in the frequency of the laser would result in phase fluctuation of the detected signal and hence would affect the SNR. The use of a single-mode laser source simplifies the building of the radar. Here, we are not concerned with the bandwidth of the laser source for direct modulation (modulation that occurs inside the laser source) since we are externally modulating the light using an intensity modulator. The laser source power supply has a variable power control. This facilitates the control of the laser emission power levels. The laser head contains a 30-dB isolator to reduce back reflections that arises from optical feedback. Optical feedback will produce instabilities in the laser.

3.2 Transmitter—Single-mode fiber

As can be seen from Figure 3.1.1, the fiber cable used in the overall system is polarization-maintaining (PM), single-mode fiber since the source is also single mode. Polarization-maintaining fibers preserve the polarization state of the laser light as it travels through the fiber core. Furthermore, polarization-maintaining fiber facilitates the use of coherent communication systems and coherent detection systems. This minimizes

the losses due to polarization misalignment. As given in (2.3.9) of Section 2.3, the resultant photocurrent at the photodetector is dependent on the relative polarization states of the signal and the LO. As a result, the use of polarization-maintaining fibers preserves the polarization states of the LO and the signal. The laser source and the Mach-Zehnder intensity modulator require the use of polarization-maintaining fibers because they are polarization dependent devices.

When a linearly polarized light is launched into a PM fiber, the output will be polarized along one of the principal axis. Light coupled into the PM fiber is split into two orthogonal axes. In an ideal situation, the two orthogonal mode light will propagate independently. Stresses are induced along the fiber core to create the two orthogonal axes, and hence we have what is called a stress-induced birefringent fiber. The plane along the stress point is called the slow axis. Most of the stress-induced birefringent fibers have a panda configuration as shown in Figure 3.2.1.

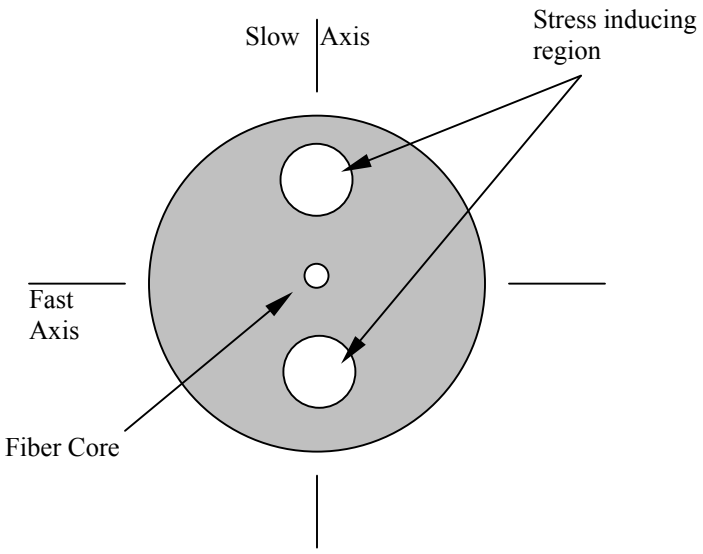

Figure 3.2.1. Fast/slow axis alignment of panda PM fiber.

The polarization-maintaining cable assemblies used are standard parts from Wave Optics™ and the stress-induced regions are aligned to the slow axis. For cable assemblies with FC/APC connectors, the typical insertion loss is between 0.4 dB and 0.8 dB. The standardized core/cladding diameters are 9/125 μm.

3.3 Transmitter—Optical frequency shifting

The 1319-nm wavelength laser light is downshifted in frequency by 600 MHz. An acousto-optic modulator can perform this function. The optical power output of the acousto-optic modulator is linearly dependent on the RF input power and the input frequency into the acousto-optic modulator. Figure 3.3.1 shows this measured relationship, where the input optical power is held constant at 10 dBm. The 600-MHz frequency driver outputs power at 28 dBm.

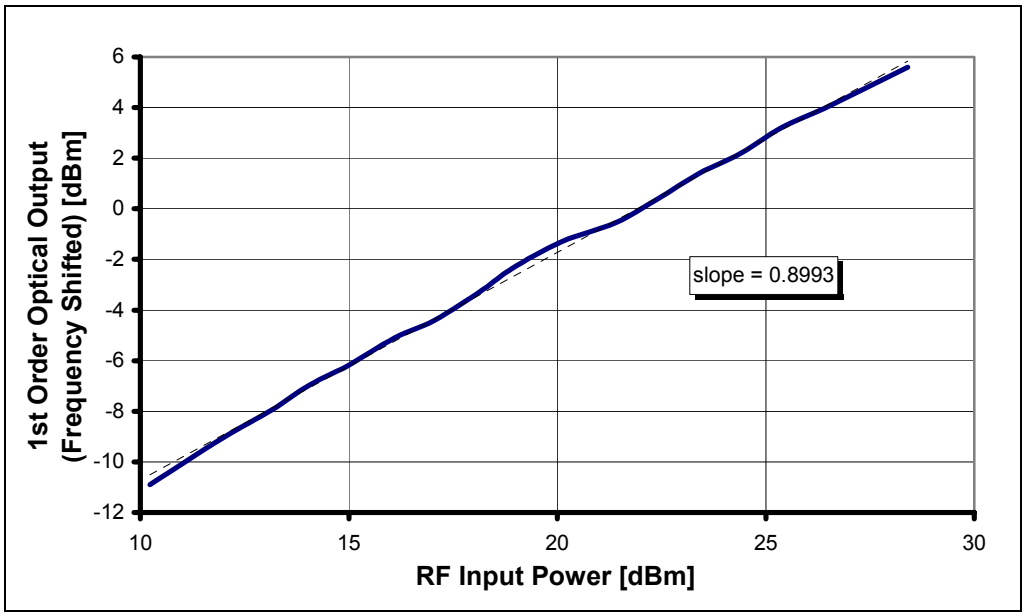

Figure 3.3.1 Plot of the first-order optical output versus 600 MHz input RF power.

The acousto-optic device used is the IPF-600-1300-3FP acousto-optic frequency shifter with fiber assembly. The FFF-600-A-F0.62 serves as a 600-MHz frequency driver for the acousto-optic frequency shifter. Both devices are manufactured by Brimrose

Corporation. The acousto-optic modulator works by passing acoustic waves through a substrate material such as indium phosphide. By doing so the substrate index of refraction is changed. Since the property of an acoustic wave is periodic, the wave then acts as a phase grating that diffracts part or all of the incident light. Thus, Bragg diffraction is obtained. The output light is frequency shifted by the amount of the acoustic frequency, $\omega_{out} = \omega_{in} \pm \Omega$, where Ω is the acoustic angular frequency, ω_{out} is the output angular frequency, and ω_{in} is the input angular frequency. The diffraction mechanism by which the frequency shifting works is shown in Figure 3.3.2. θ_B = Bragg diffraction angle, and Λ = acoustic wavelength. One output of the acousto-optic frequency shifter is frequency shifted, whereas the other output is not ([13], pp. 732 – 734).

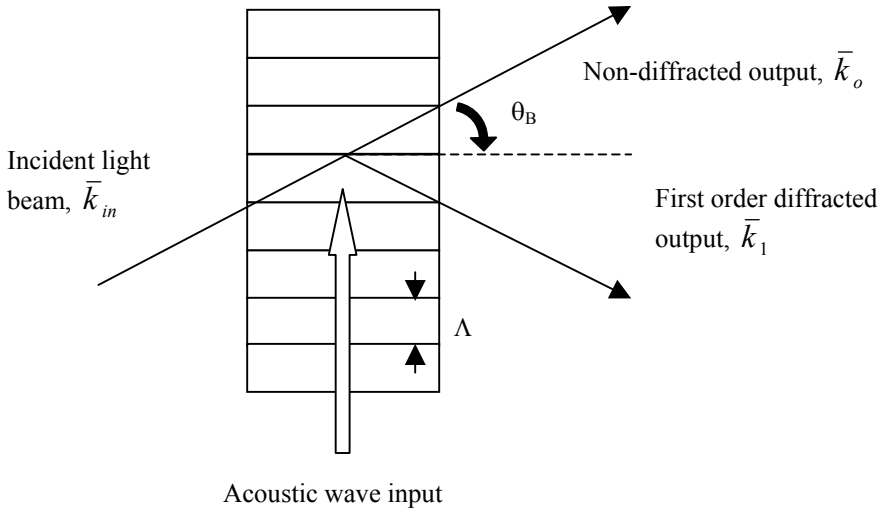

Figure 3.3.2. Down-shifted Bragg diffraction (adapted from [13], p. 733).

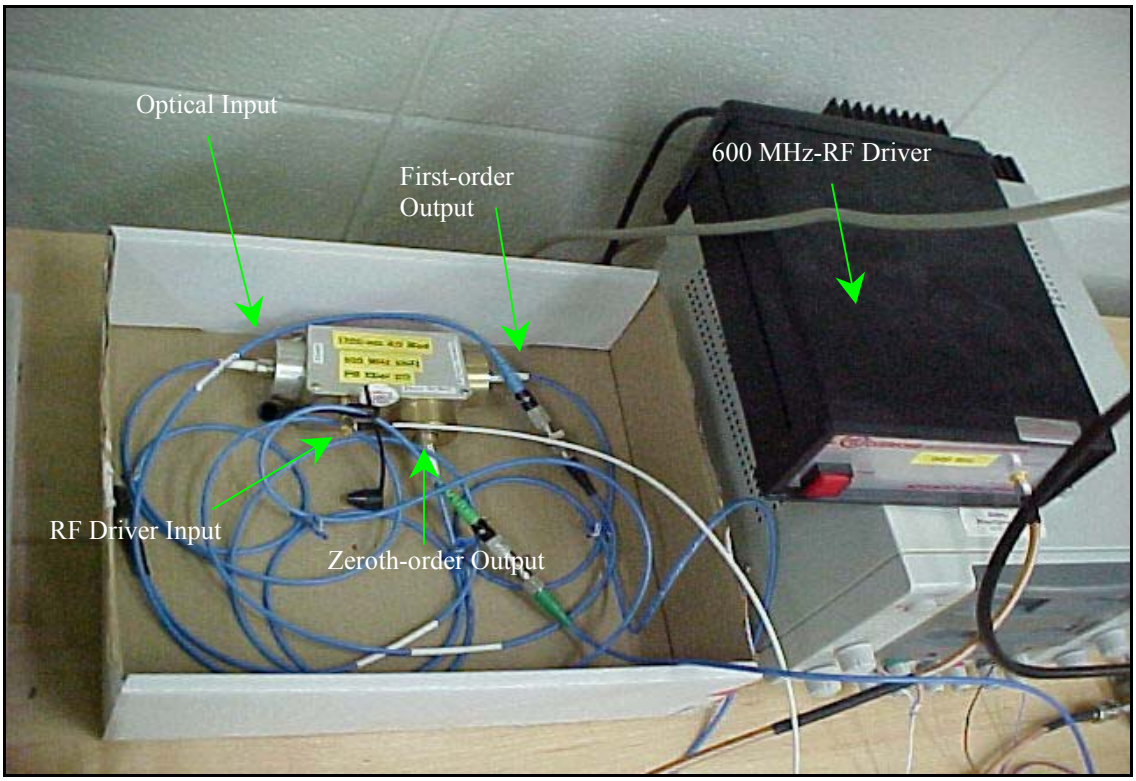

Figure 3.3.3 600-MHz acousto-optic frequency shifter and driver.

The frequency of the 1319-nm light corresponds to 227.4 THz (from the relationship $\nu = c/\lambda$, where ν and λ are the frequency and wavelength, respectively). Therefore, the optical output of the acousto-optic modulator will have a frequency corresponding to 227.4 THz – 600 MHz. The purpose of this downshifting is so the mixing of the optical local oscillator (LO) and the downshifted light will produce an intermediate frequency (IF) at the photodetector output. A picture of the Brimrose acousto-optic frequency shifter and the 600-MHz RF driver is shown in Figure 3.3.3.

3.4 Transmitter—Optical intensity modulation

After frequency shifting the optical carrier, the RF signal is imprinted upon the optical carrier by intensity modulating the carrier. A Mach-Zehnder intensity modulator is used to achieve this purpose. The Mach-Zehnder modulator is a polarization-sensitive

device. The electrical and optical specifications for the intensity modulator are shown in Table 3.4.1.

Table 3.4.1 Intensity modulator specifications.

Optical specifications	
Operating wavelength (nm)	1320 ± 10
Insertion loss, maximum (dB)	5.0
On/off extinction ratio, minimum (dB)	20
Optical return loss, maximum (dB)	-50
Maximum input optical power (mW)	200
Electrical specifications	
RF input power, maximum (dBm)	+27
V_π at 1 GHz, maximum (V)	5.3
Impedance, typical (Ω)	50

The intensity modulator used is the APE™ Extended Frequency Response Analog Modulator and operates from DC up to 20 GHz. It is model number AM-130-1-1-C2-I1-01 from Uniphase Telecommunications Products (UTP). No DC biasing is required for the operation [19].

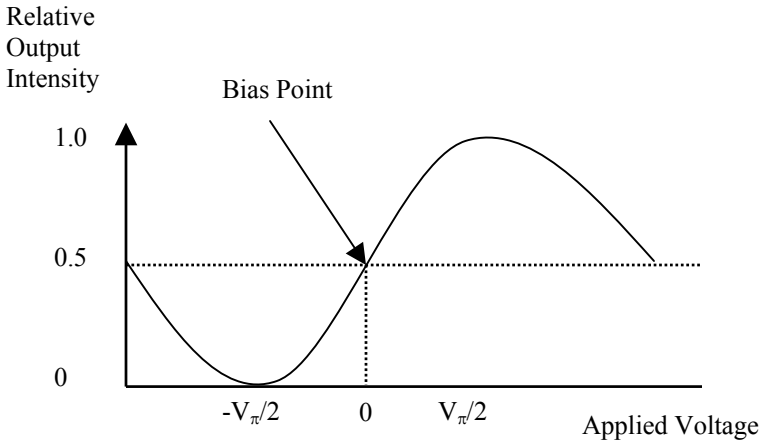

Figure 3.4.1 Modulator transfer function (copied from [19]).

Figure 3.4.1 shows the transfer characteristic of the intensity modulator. The modulation is achieved by applying a voltage of $-V_\pi/2 < V_{mod} < V_\pi/2$ to the modulation port of the device. A photograph of the UTP Mach-Zehnder intensity modulator is shown in Figure 3.4.2.

The intensity modulator is fed with a linear RF chirp with a start frequency of f_1 = 100MHz and a stop frequency of f_2 = 360 MHz ($\omega_2 = 2\pi f_2$). The bandwidth of the signal is therefore 260 MHz.

Figure 3.4.2 UTP Mach-Zehnder intensity modulator.

A polynomial waveform synthesizer Model 2045 from Analogic® Data Precision® is used to generate the RF chirp. Since the optical signal is amplitude modulated, the RF drive power into the intensity modulator must be enough to produce a sufficiently high

modulation index. The optical signal now will have the spectrum as shown in Figure 3.4.3.

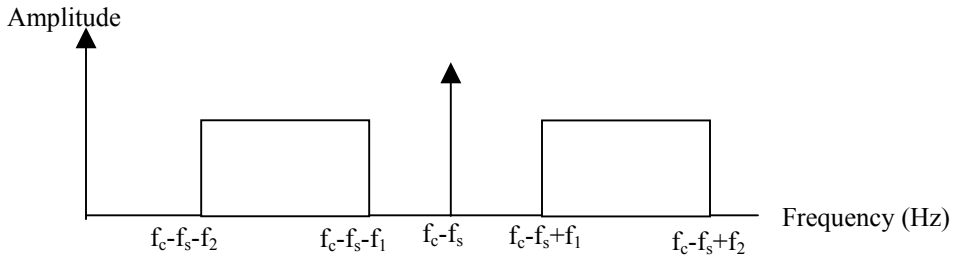

Figure 3.4.3 Spectrum of optical transmit signal.

where f_c = 227.4 THz corresponding to 1319 nm wavelength light,

f_s = 600 MHz (down-shifting frequency),

f_1 = 100 MHz (chirp start frequency), and

f_2 = 360 MHz (chirp stop frequency).

3.5 Transmitter—Fiber-optic amplifier

The optical signal is amplified using an optical amplifier. Amplification is done using the FLOUROAMP 1310, a praseodymium-doped fiber amplifier from IPG Photonics. The FLOUROAMP 1310 is manufactured for use in telecommunications and CATV instruments. It provides a single-stage, low-noise amplification. In the Amplified Stimulated Emission (ASE) mode, the amplifier provides gain even at very low input power. The ASE mode outputs a single-mode, unpolarized, broadband, 1290 nm to 1320 nm light source. In Table 3.5.1, we give the specifications for the amplifier.

Table 3.5.1. Optical amplifier specifications.

Parameters	Specifications
Operating wavelength	1285 – 1320 nm
Input signal range	Up to + 8 dBm
Output power	17 dBm typical
Input return loss	45 dB min.
Noise figure (@ 1319nm)	7.3 dB max.
Polarization sensitivity	0.2 dB max.

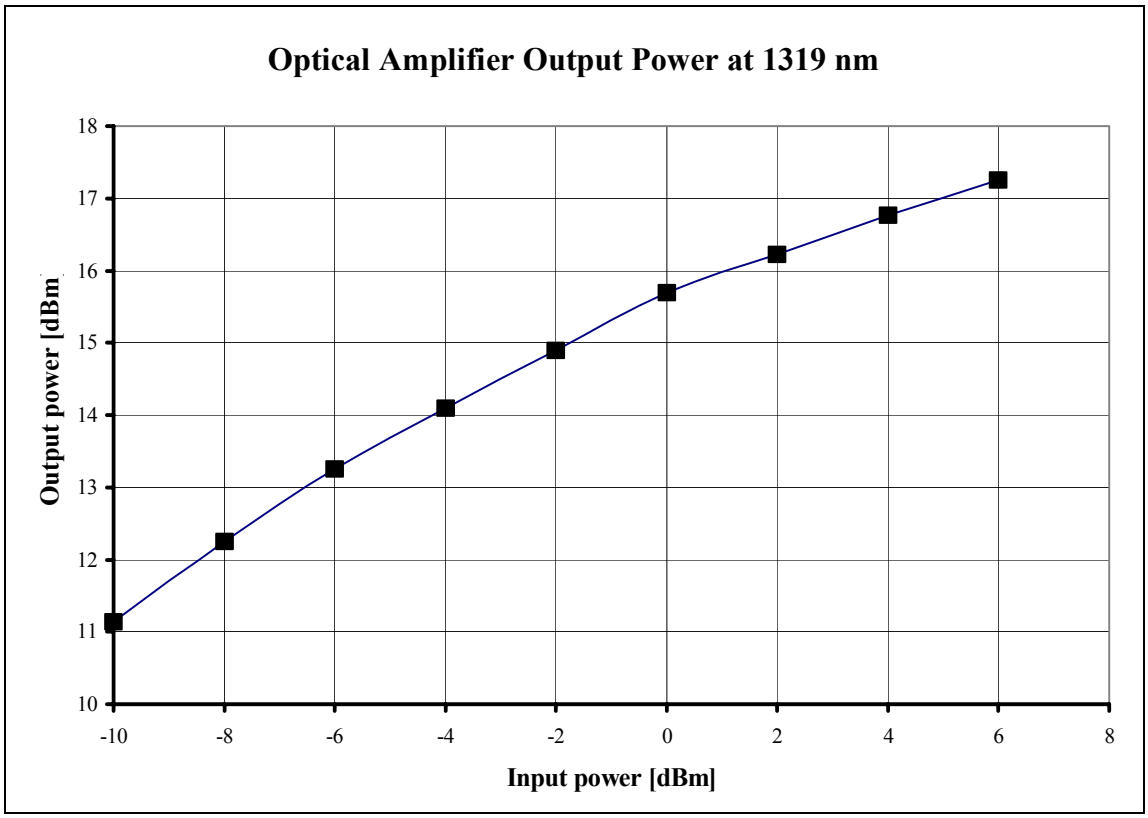

Figure 3.5.1. Optical power input/output amplifier characteristics at 1319 nm.

Figure 3.5.1 shows the transfer function of the optical amplifier and its linearity. The optical amplifier boosts the signal power prior to transmission.

3.6 Transmitter—Telescopes and optics

After the optical signal has been amplified, it is then fed into the telescope so the optical signal can be transmitted. A multi-fiber assembly with a MTP standardized ferrule connector from Johanson Fiber Optics Group, LLC (part number M0121M1F2001M10) is mounted in the focal plane of the telescope to enable reception and transmission of the optical signal. The assembly has a FC/PC polished connector and SM 9/125 μm 1-m fiber pigtails. The MTP connector end has 12 fibers arranged in a row as shown in Figure 3.6.1. Adjacent fibers are used for a transmission and reception.

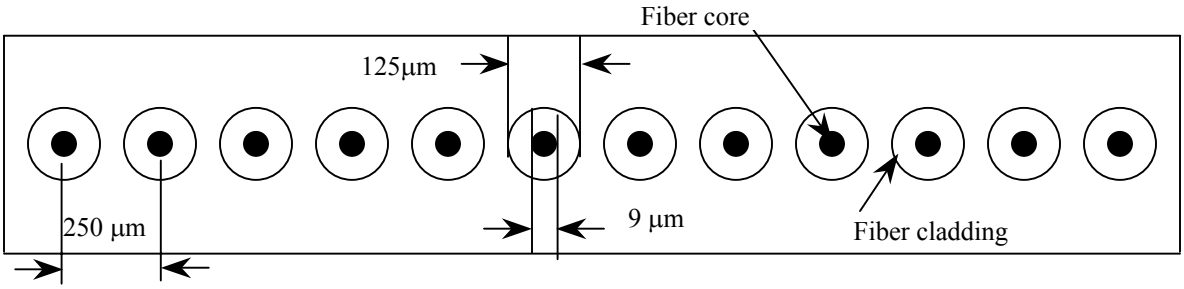

Figure 3.6.1 MTP ferrule fiber-array connector.

Photographs of the fiber array fixture mounted to the telescope focal plane and beam patterns formed 2 m away are shown in Figure 3.6.2.

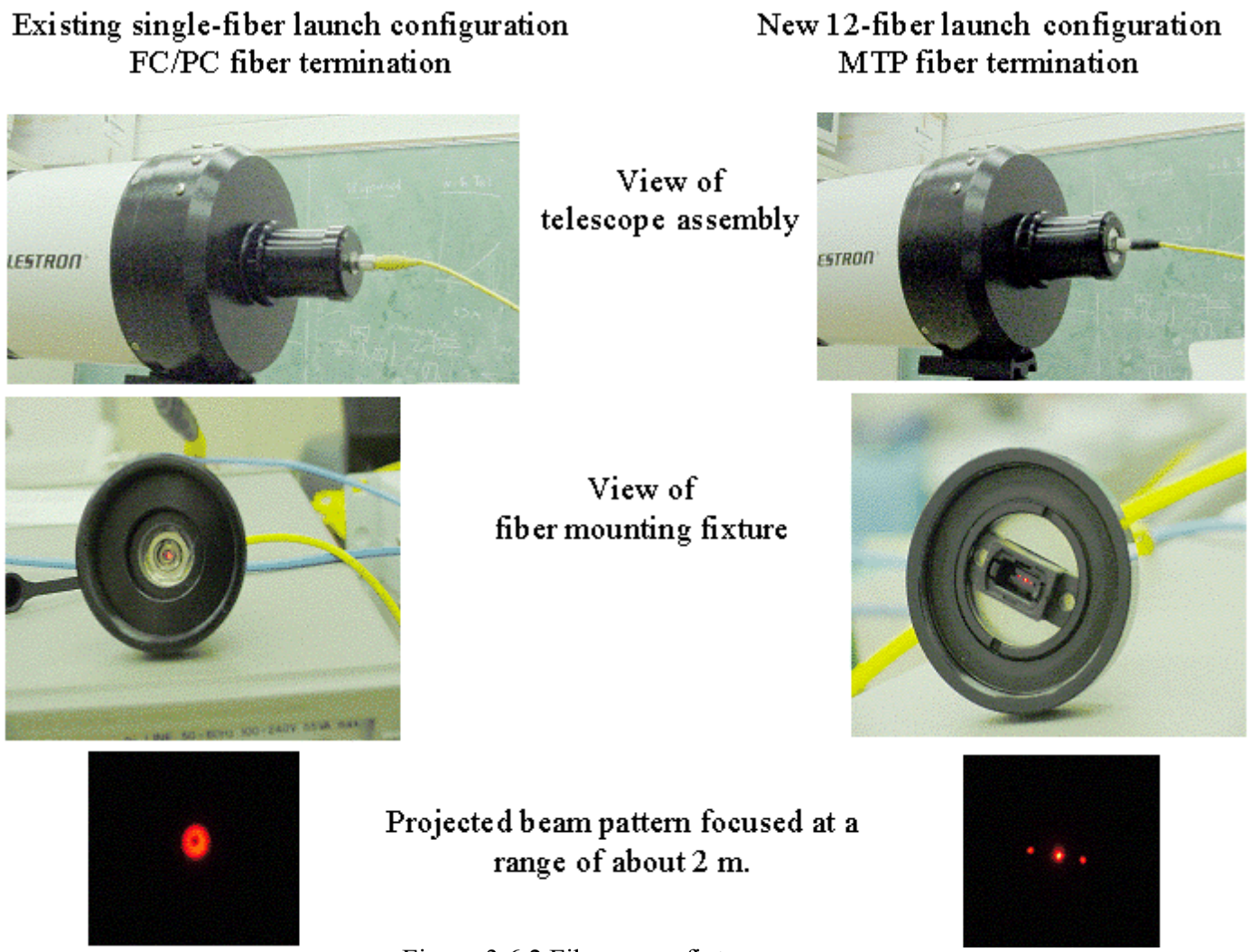

Figure 3.6.2 Fiber array fixture.

The coupling efficiency of the fiber to the telescope plays an important role in the laser radar system. Astronomers have shown that the maximum theoretical coupling efficiency of SMF to large aperture telescopes is about 80% (or 1 dB). This is due to the mismatches in the field distribution between the telescope and the fiber [20, 21]. Furthermore, in lidar applications, the maximum coupling efficiency is only 42% or -3.8 dB for random light coupling into SMF [22].

The telescope used in the transmission and reception is the C5+ and C5 Schmidt-Cassegrain design telescope from Celestron®. The internal structure of the telescope is shown in Figure 3.6.3, and Table 3.6.1 gives the telescope specifications.

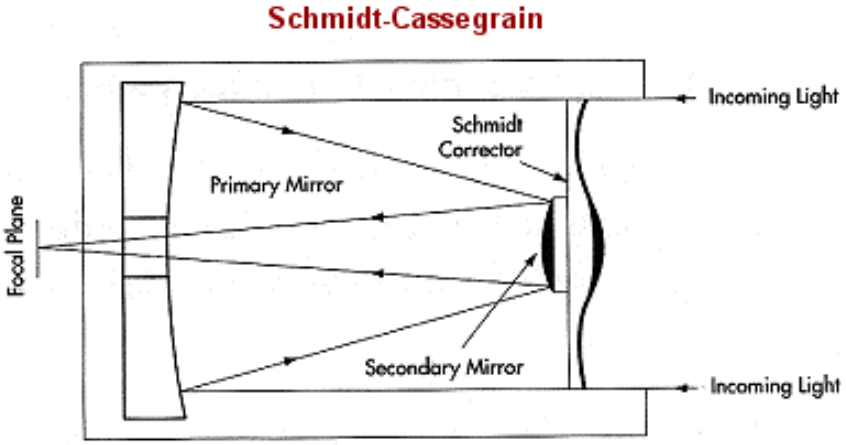

Figure 3.6.3 A Schmidt-Cassegrain or catadioptric telescope (from Celestron® http://www.celestron.com/schmidt.htm).

Table 3.6.1. Telescope specifications.

Parameters	Specifications
Aperture diameter	5 in./127 mm
Focal length	1250 mm
Near focus	20 ft.
f/#	10

The telescope can only focus on targets greater than 20 ft. away, as denoted by the near-focus distance. The aperture diameter of the telescope is used in the calculation of

the radar range equation given in Chapter 2. A photograph of the two telescopes is shown in Figure 3.6.4.

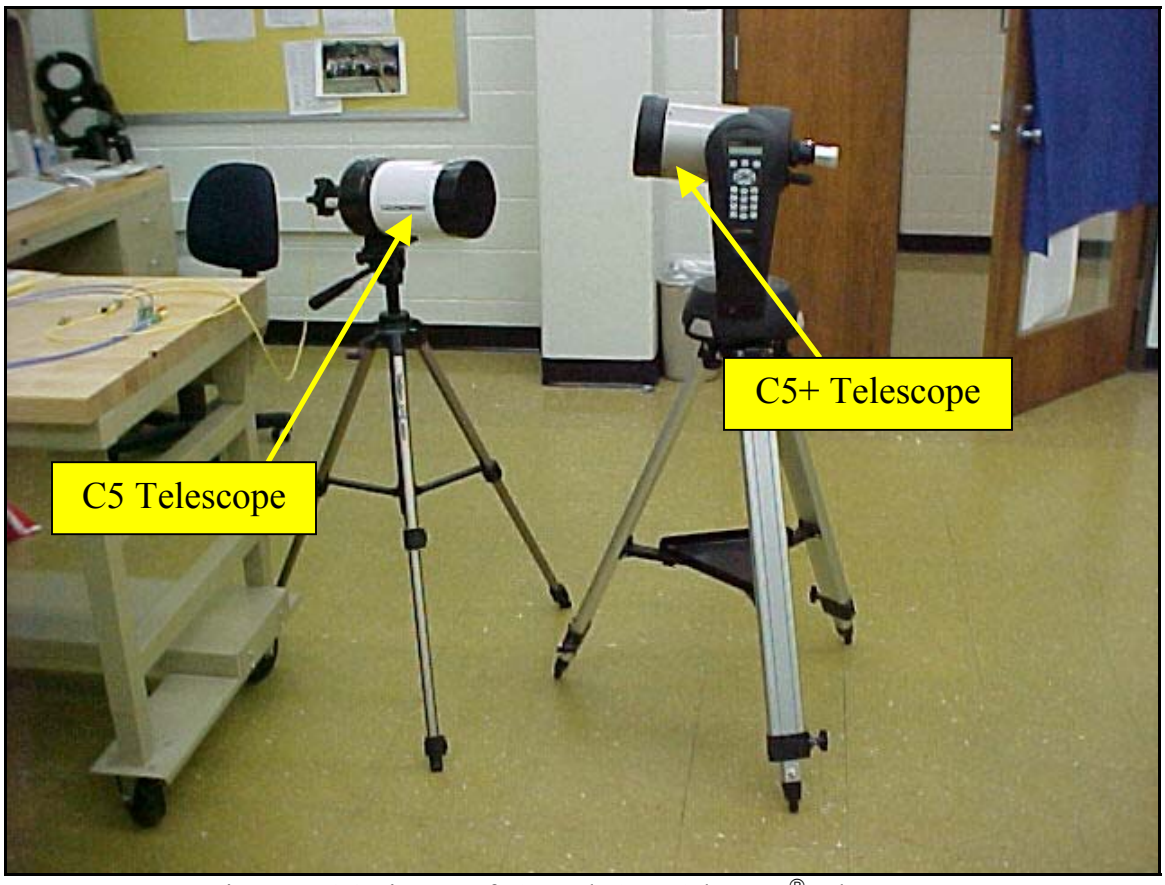

Figure 3.6.4 Picture of C5 and C5+ Celestron® telescopes.

The reception of the optical scattered signal entails the use of optical receive devices, after which comes RF signal processing. The RF signal process is comprised of photodetection, direct downconversion, dechirping, and then digitization. These are processes discussed below.

3.7 Receiver—Optical mixing

The scattered return signal is combined with the optical LO using a fiber optic coupler from Canadian Instrumentation and Research Limited. The coupler used is a polarization-maintaining model 904P fiber optic coupler with low loss and back reflection. The 1-m PM fiber pigtails also have the same Panda configuration shown in

Figure 3.2.1 and are terminated with FC/APC connectors to suppress back-reflections. The coupler used to combine the LO and the signal optically is a 180° hybrid coupler. The coupler induces a 180° phase shift between the two output ports of the hybrid coupler. As a result, both the phases of the LO and the return signal are unchanged.

3.8 Receiver—Balanced photodetection

Balanced photodetection is accomplished using the balanced photoreceivers model 1617-AC from New Focus, Inc.® Table 3.8.1 lists the specifications for the balanced photoreceivers.

The balanced photodetector works in the near-infrared region and is suitable for our application since our breadboard laser radar works at 1319 nm wavelength light. The maximum conversion gain in Table 3.8.1 gives the optical-to-electrical conversion factor. For example, if the optical input power is 0 dBm or 1 mW, then the RF output will be 0.7 V. The NEP or noise equivalent power defines the input optical power that will result in a SNR of 1 at the output of the photodetector for a given detector bandwidth. The noise in reference here is thermal noise. For example, given that the NEP is 20 pW/√Hz, the optical power required for a photodetector with a bandwidth of 800 MHz to obtain an SNR = 1 is $20\,\mathrm{pW}/\sqrt{\mathrm{Hz}} \times \sqrt{800\,\mathrm{MHz}} = 5.66 \times 10^{-7}$ W or -32.5 dBm.

Table 3.8.1 New Focus balanced photodetector specifications.

Parameters	Specifications
Wavelength	900 – 1700 nm
3-dB bandwidth	40 kHz – 800 MHz
Rise time (estimated)	0.6 ns
Typical max. responsivity, $\Re$	1.0 A/W
Transimpedance gain	700 V/A
Max. conversion gain	700 V/W
Minimum NEP	20 pW/$\sqrt{}$Hz
Saturation power	1 mW
Absolute max. power	2 mW
Max. output RF power	+12 dBm (into 50 Ω)
Photodiode material/type	InGaAs/PIN

Using the chirp as defined in Section 3.4 with a start frequency of 100 MHz and a bandwidth of 260 MHz, the spectrum at the output of the balanced photodetector is as shown in Figure 3.8.1. The actual measured spectrum at the output of the balanced photodetector is shown in Figure 3.8.2. The upper-side band rolls off because the photodetector's bandwidth upper limit is 800 MHz. We see some low frequency noise from 0 MHz to 150 MHz, this is due to frequency leakage from the waveform generator.

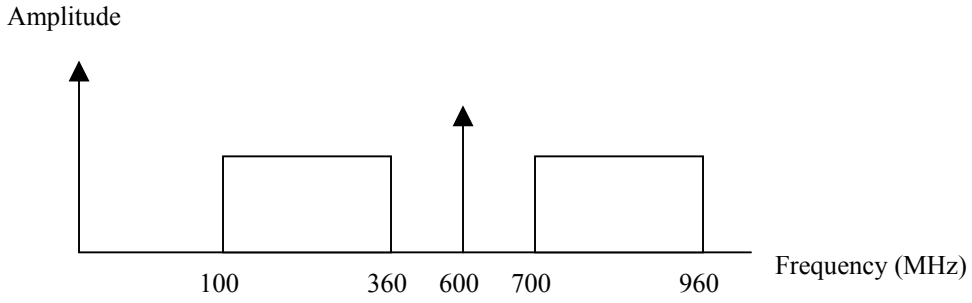

Figure 3.8.1 Spectrum of photodetected signal.

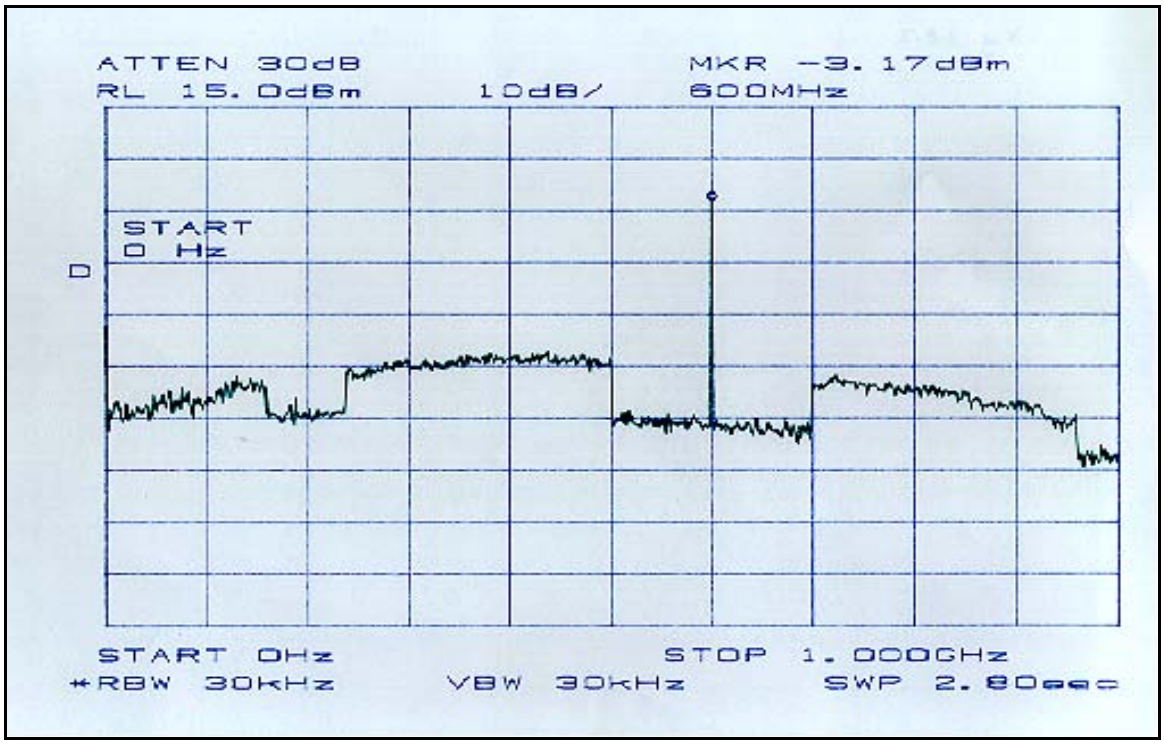

Figure 3.8.2 Spectrum of photodetected signal as seen on the spectrum analyzer.

3.9 Receiver—RF pulse compression and analog dechirping

The next step after photodetection is the dechirping of the photodetected signal. The signal from the balanced photodetector is mixed with the original version of the chirp. An RF mixer, CMK-7A6S from Synergy® Microwave Corporation is used for the dechirping process. The RF/LO ports work from 0.5 MHz to 2000 MHz, and the mixer requires an LO power of +13 dBm. The IF output has a range of 0.2 – 600 MHz. The output of the balanced photodetector is then amplified and fed into the RF port of the mixer, and the amplified original chirp is fed into the LO port with +13 dBm power. The difference in phase between the return signal chirp and the original chirp must be a constant phase; otherwise phase fluctuation will occur. Phase fluctuation implies a fluctuation in the amplitude of the dechirped signal. The output of the mixer will now consist of two frequency spikes, which correspond to the range delay. Since the source of the Mach-

Zehnder intensity modulator and the dechirping signal is the same, the phase difference between the return signal and the dechirp signal will be constant. Figure 3.9.1 shows the spectrum of the mixer output; the output signal is a dechirped signal. Δf relates to the round-trip delay time. The dechirped signal displayed on the spectrum analyzer is shown in Figure 3.9.2.

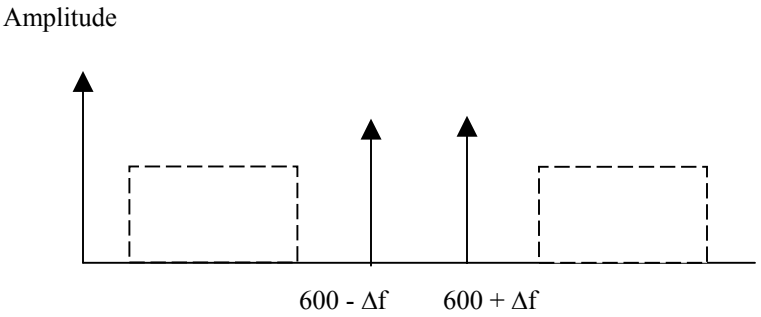

Figure 3.9.1 Spectrum of dechirped signal.

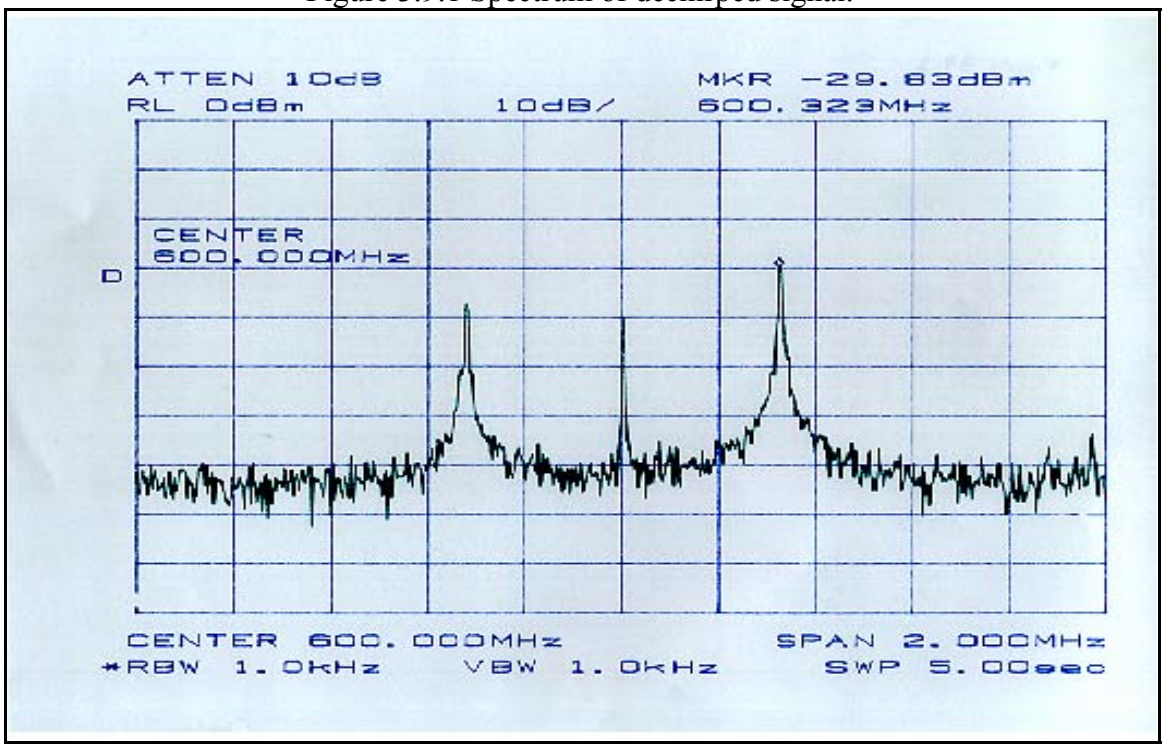

Figure 3.9.2 Spectrum of dechirped signal as seen on the spectrum analyzer.

3.10 Receiver—in-phase and quadrature detection (frequency down-conversion process)

The next step after the dechirping process is to strip away the carrier frequency, which contains no range information. All the necessary information is contained within the time-delayed chirp. Therefore we use direct downconversion to remove the RF LO. In this technique, we split the RF return chirp signal into two using a Mini-Circuits® ZFSC-2-2500 3 dB 0° splitter that works from 10 MHz to 2500 MHz . The 600 MHz tone that drives the acousto-optic frequency shifter is also split into two using a Mini-Circuits® ZFDC-20-5 coupler. The coupled output is 20 dB lower than the feed-through output. The feed-through output is used to drive the acousto-optic frequency shifter and the coupled output is used in the down-conversion process.

The coupled output is then passed through a 90° hybrid DQK-90-450S from Synergy® Microwave Corporation, which works in the 90 – 450 MHz range. Although the down-conversion frequency is 600 MHz and therefore beyond the range of the hybrid, we found out that the hybrid still works quite well at 600 MHz. The specification sheet shows that the typical insertion loss is 1.2 dB to 1.5 dB maximum. However, tests show that the insertion loss in the 0° port is 4.2 dB and 5.26 dB in the 90° port. This is because we are operating the hybrid outside of its intended frequency range. The tested phase difference between the two output ports is 87° and not 90°. This is within the specified phase unbalance of 3.0° – 5.0°. In the frequency down-conversion process, one branch of the dechirped signal is mixed with the carrier sinusoid, and the other branch is mixed with the quadrature (or 90° out-of-phase) version of the carrier sinusoid. In this way, as shown in Appendix 1, the total detected signal never fluctuates to zero. There is trading

of power between the two outputs. If the in-phase channel goes to zero, the other channel approaches a maximum level and vice versa. The output signal now will be a pure sinusoid with additive white noise. The frequency of the sinusoid is dependent on the range to a target.

3.11 Receiver – Data acquisition system

The I and Q detected signal is then low-pass filtered and digitized using the Greenland Integrator Card data acquisition system, which was built by Torry Akins in 1997 [8]. The data acquisition system first digitizes the analog data stream with 12-bit resolution. It then saves the data stream in the hard drive of the computer and displays the fast Fourier transform (FFT), as well as the time domain signal on the screen. The user can also specify the number of samples per pulse to be used up to a maximum of 2048 samples. The system uses a 16 MHz TTL clock, which provides a sampling frequency of 8 MHz. The system also uses this clock to trigger the chirp generator, which is user definable up to 18.4 kHz. In our case, we set the PRF to 1 kHz. Figure 3.11.1 shows the time-domain representation of the actual chirp generated with a 200-μs pulse duration. The 1-kHz PRF is fed into the waveform generator to produce the desired chirp.

The synchronization of the PRF and the chirp enables integration (averaging) of the detected signal pulses using the data acquisition system. As a result, we can increase the SNR as explained in the previous chapter under coherent integration.

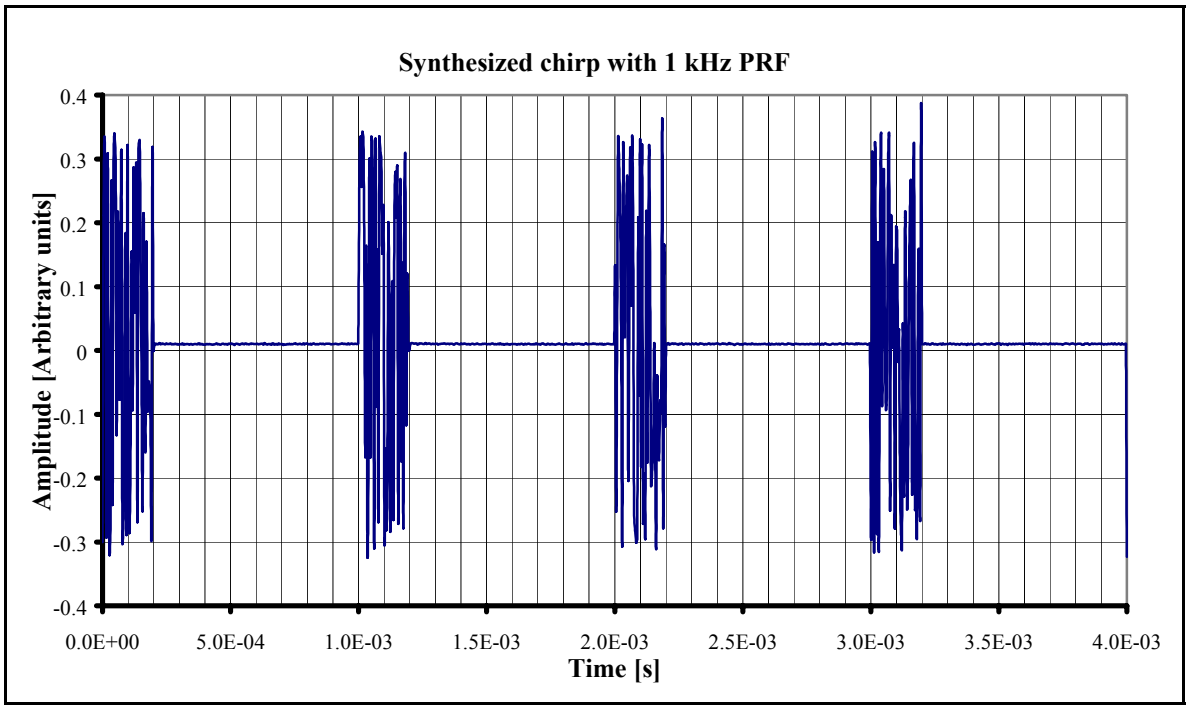

Figure 3.11.1 Time-domain chirp with 1 kHz PRF and 200 μs pulse duration.

However, the on-board coherent integration cannot be done using the direct downconversion detection technique since the phase of the I or the Q channel detected signal may fluctuate randomly between negative and positive values from pulse to pulse. As a result, coherent integration will only cause the signals to integrate to zero. Therefore as discussed in the end of Chapter 2, we square the FFT of the I and Q signals and then take their sum. In such a case, incoherent integration may be employed to reduce the noise variability.

3.12 Receiver—Simulation and results

Simulation is carried out to determine the shot-noise characteristics and how the receiver will behave for a shot-noise-limited system. Several assumptions were taken into consideration when we did the simulation on an MS EXCEL spreadsheet. First, the bandwidth of the system is 800 MHz corresponding to the photoreceiver bandwidth. This

sets the noise bandwidth. Secondly, the temperature of the system is assumed to be at constant room temperature (i.e., 290 K), and the responsivity, $\Re$, of the photoreceiver is assumed to be 1 A/W. The purpose of this simulation is to find out how changing the optical local oscillator power will affect the detected coherent return signal power, direct-detected signal power, and noise at the coherent receiver output.

First, we will need to set up and define the parameters that will be used in the analysis. The block diagram for the analysis of the outputs at the photodetector is given in Figure 3.12.1.

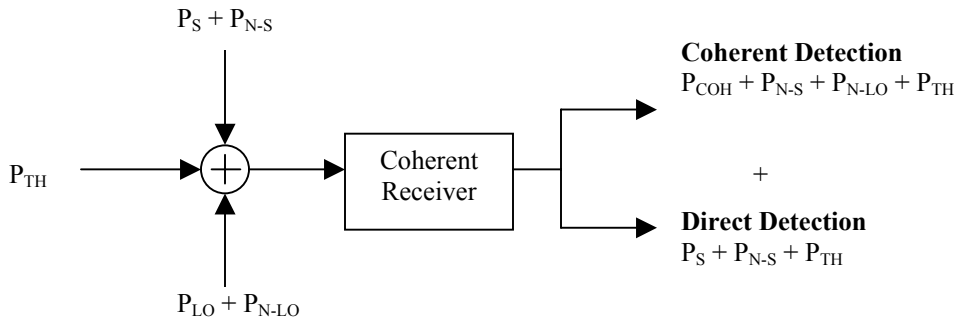

P_S = return signal power
$P_{N\text{-}S}$ = shot noise due to P_S
P_{LO} = optical LO power
$P_{N\text{-}LO}$ = shot noise due to P_{LO}
P_{TH} = thermal noise power
P_{COH} = coherent detected signal
$P_{COH} = \left(2\Re\sqrt{P_S P_{LO}}\right)^2$

Figure 3.12.1 Simulation block diagram.

As Figure 3.12.1 shows, the inputs into the coherent receiver will be the return signal power plus shot noise due to the signal power, the local oscillator power plus its shot noise counterpart, and thermal noise of the receiver. The outputs therefore consist of the coherent detected signal plus noise and the direct detection signal plus noise.

For calculation of the signal-to-noise ratios, we obtain the direct-detection SNR, and the coherent-detection SNR. The direct detection SNR is defined as

$$SNR_{DD} = \frac{P_S}{P_{N-S} + P_{TH}} \tag{3.12.1}$$

and, the coherent detection SNR is given as

$$SNR_{COH} = \frac{P_{COH}}{P_{N-S} + P_{N-LO} + P_{TH}} \tag{3.12.2}$$

Shot noise is calculated as shown below ((13), p. 238):

$$P_{SHOT} = 2qB\Re P \tag{3.12.3}$$

where P can be either return signal power or optical LO power. For thermal noise we have ((13), p. 240):

$$P_{TH} = \frac{4kTB}{R} \tag{3.12.2}$$

where k = Boltzmann's constant = 1.38×10^{-23} J/K, B = photoreceiver bandwidth (Hz), R = 50 Ω, and T = 273 K.

Figures 3.12.2 (a) through (d) show that by increasing the optical LO power, the coherently detected signal increases as expected.

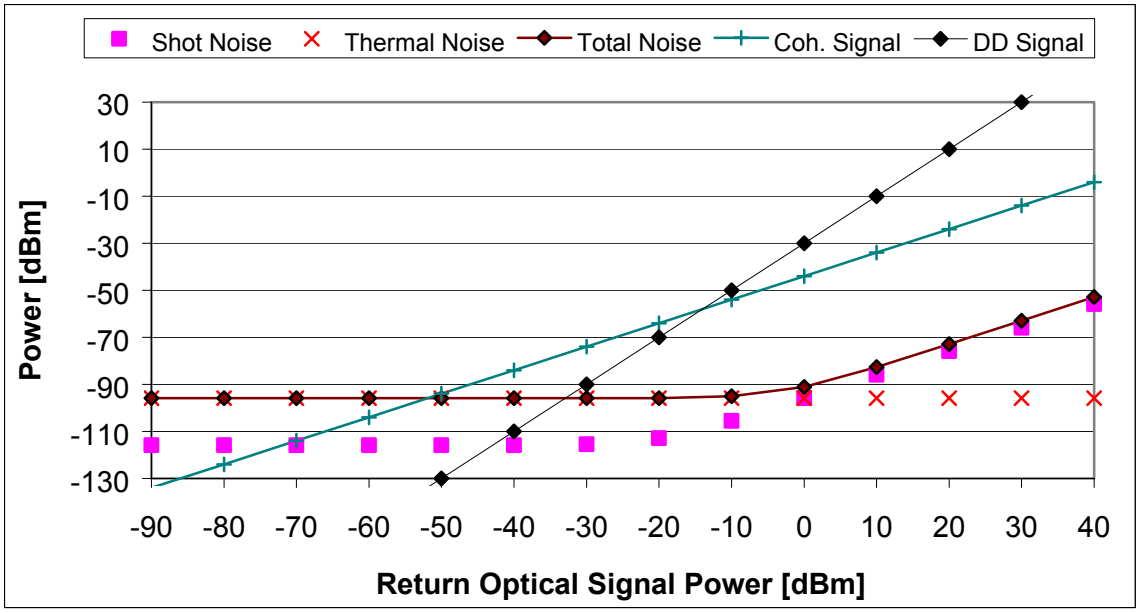

Figure 3.12.2 (a) Variation with return signal power: -20 dBm optical LO power.

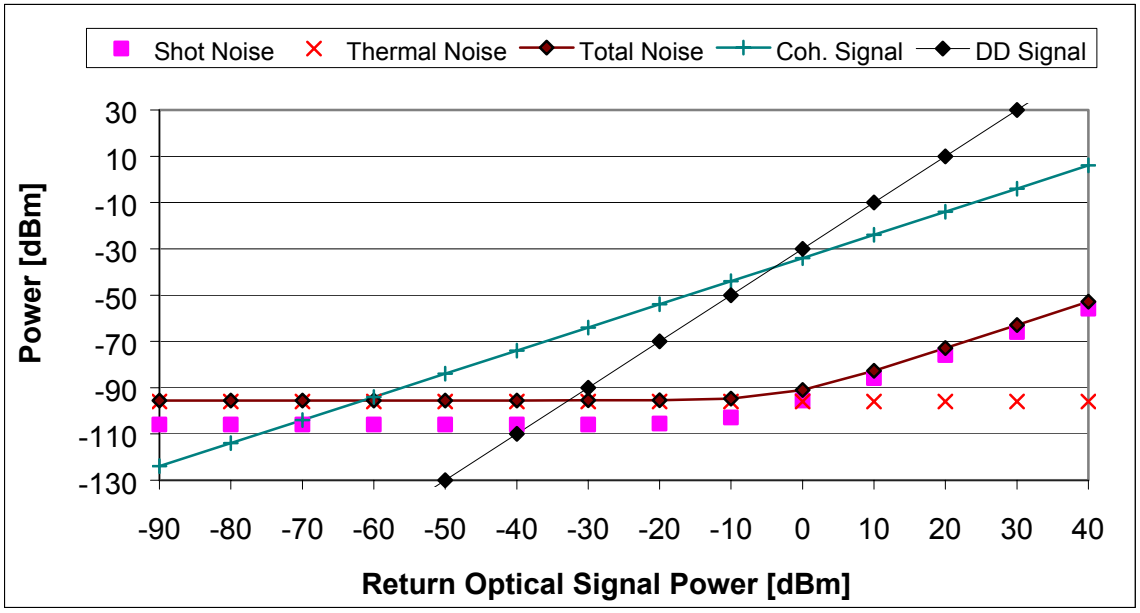

Figure 3.12.2 (b) Variation with return signal power: -10 dBm optical LO power.

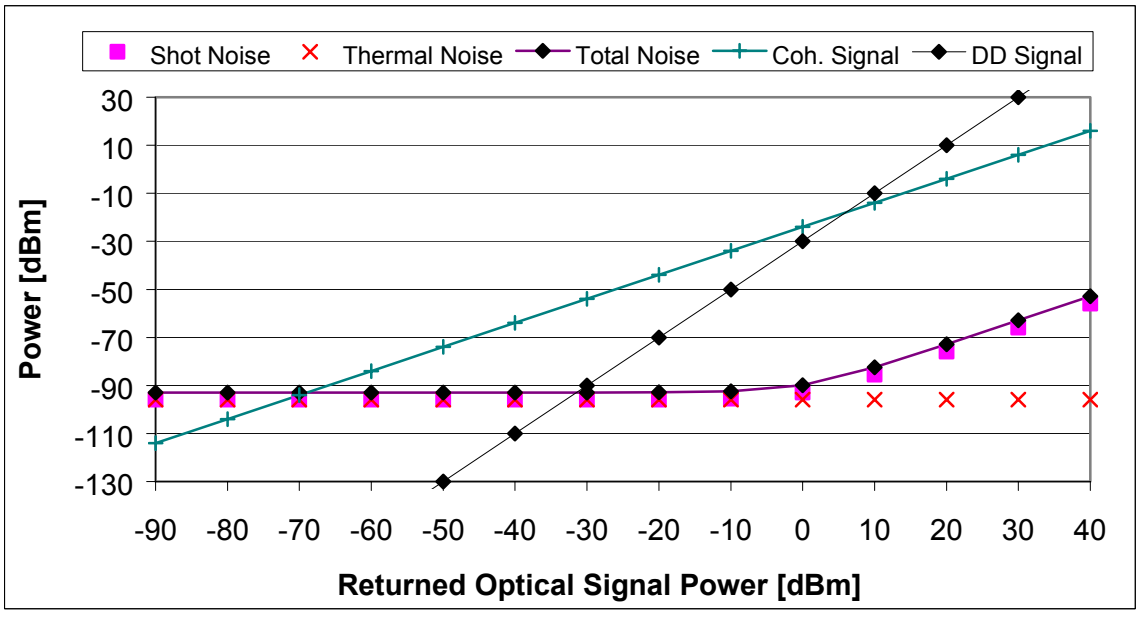

Figure 3.12.2 (c) Variation with return signal power: 0 dBm optical LO power.

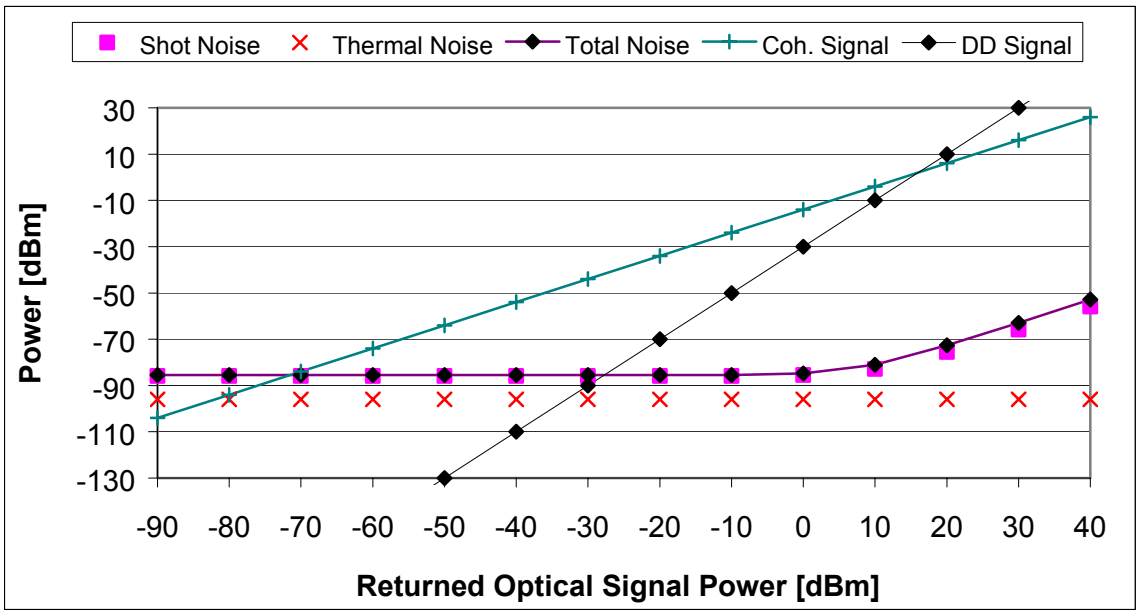

Figure 3.12.2 (d) Variation with return signal power: 10 dBm optical LO power.

We see that the crossing point between the directly detected signal curve and the coherently detected signal increases with respect to increasing optical LO power. However, only the coherently detected signal is useful. As shown in the example given at the end of Section 2.5, the coherently detected signal power is much higher than a directly detected signal. Taking into consideration that the return signal will be very weak (around 0.001 nW or -90 dBm), and that the direct detected signal should be as weak as possible in comparison to the coherently detected signal, a suitable optical LO power should be chosen. Figures 3.12.2 (a) through (d) show that the optical LO power should be as high as possible.

A similar simulation was done to determine how much optical LO power to use. The relationship between SNR at the photodetector output and the LO power for a fixed return signal of –90 dBm and 800 MHz photodetector bandwidth is given in Figure 3.12.3.

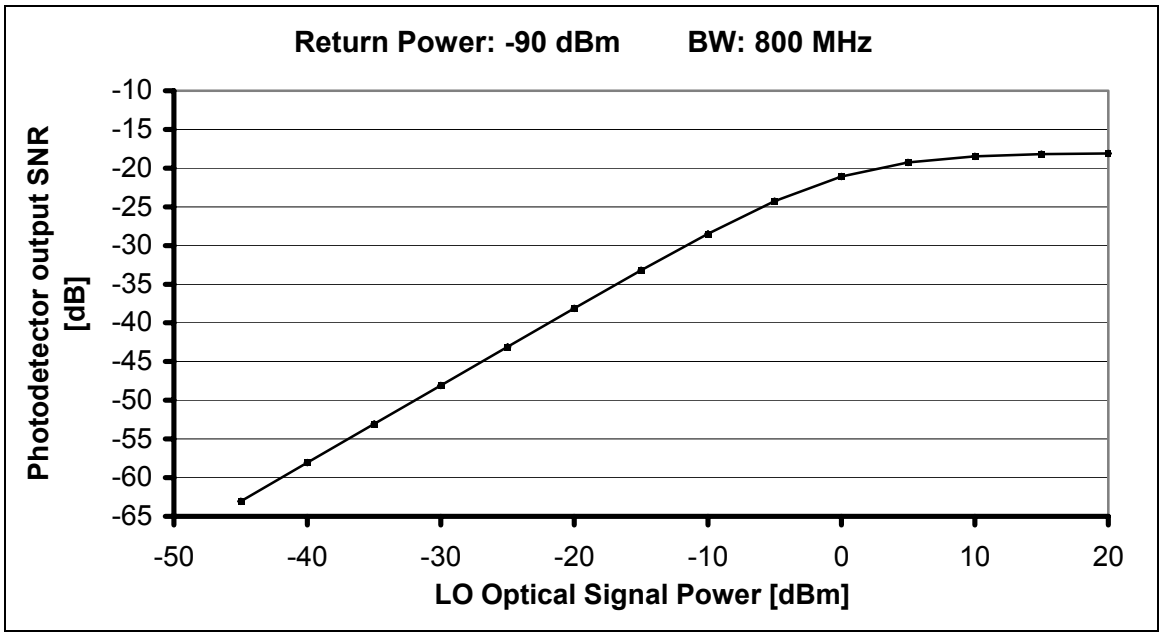

Figure 3.12.3 Photodetector output SNR and optical LO power relationship.

The relationship in Figure 3.12.3 shows that the SNR does not improve beyond using 0 dBm of optical LO power. This puts a limitation on how much LO optical power should be used.

Figure 3.12.4 shows how coherent detection is far superior to direct detection, in terms of SNR, for different levels of LO optical power and various optical return signal powers. It shows that coherent detection provides a higher SNR than direct detection for the same amount of return signal power. For example, for a return signal power of -80 dBm and 0 dBm optical LO power, the SNR for coherent detection signal is -11 dB, while the SNR is -94 dB for direct detection. This goes to show that using coherent detection gives an 83 dB gain over direct detection for a -80 dBm return signal power.

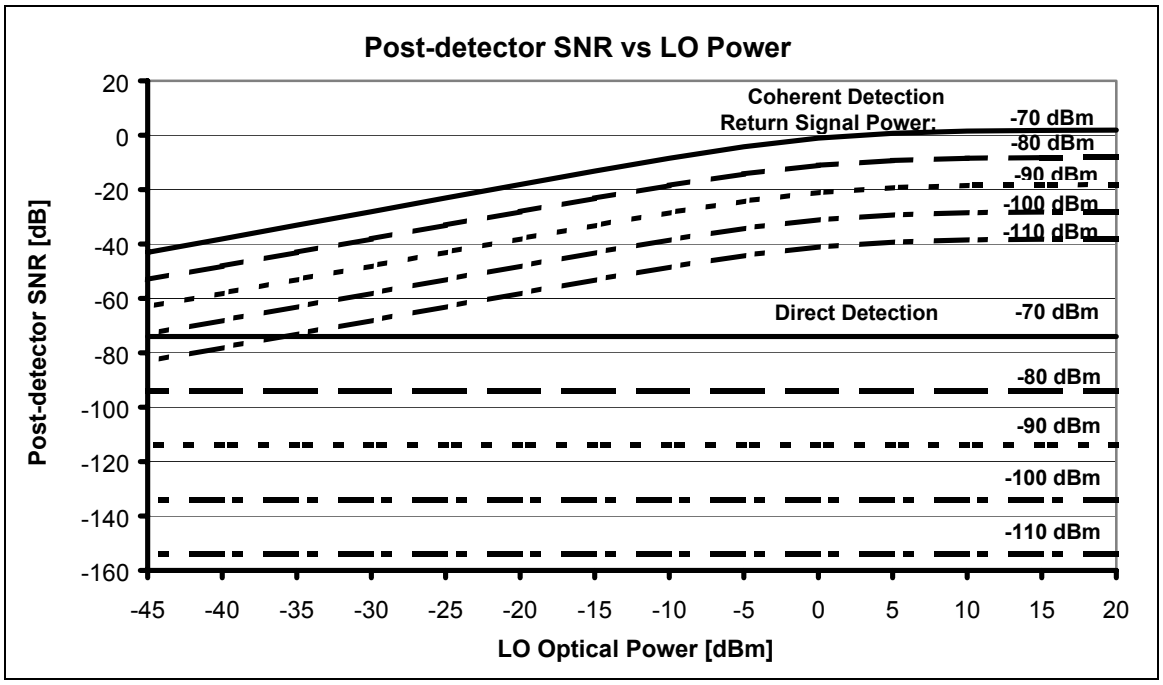

Figure 3.12.4 Comparison of coherent and direct detection.

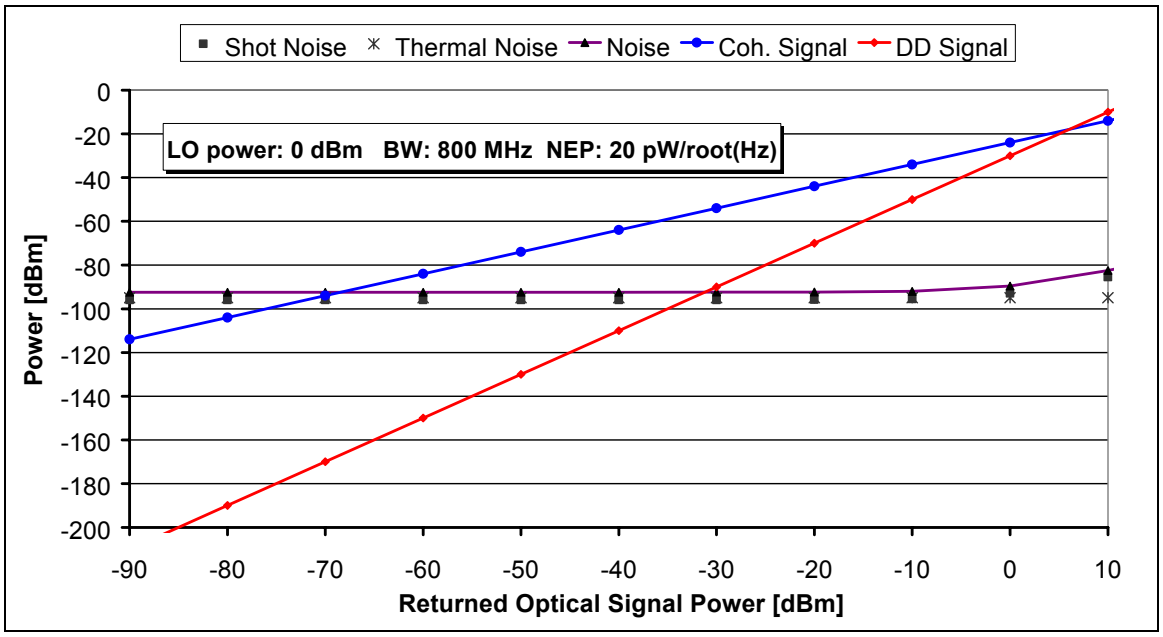

Figure 3.12.5 Variation of detected signal power with optically received signal power.

The analysis given in Figure 3.12.5 is modeled using the New Focus balanced photodetector parameters, and 0 dBm of LO power. As the optical LO power increases from 0 dBm, the directly detected signal power becomes comparable to the coherently

detected signal. In other words, the rate the direct-detected signal decreases is faster than that for the coherent-detected signal, for decreasing return signal powers, as shown in Figure 3.12.5. This is a problem if the directly detected signal bandwidth lies within the bandwidth of the coherently detected signal.

CHAPTER 4

EXPERIMENT AND RESULTS – DIRECT DOWNCONVERSION

In this section, we will discuss the testing procedures and the hardware test setup used to test the laser radar system using the in-phase and quadrature detection process.

4.1 Hardware laboratory test setup

The laboratory test setup is shown in Figure 4.1.1, and the test setup block diagram was given in Figure 3.1.1. The function of the HP 8156A variable optical attenuator is to provide a variable and known transmit optical power range for our measurements. The optical attenuator operates from 1200 to 1650 nm wavelength and has 60 dB of attenuation range. The return loss is 45 dB and the attenuation accuracy is less than ± 0.5 dB. The Model 2045 from Analogic® is an 8-bit polynomial waveform generator with an internal maximum clock frequency of 800 MHz. It has two selectable outputs, A and B. The A port outputs 3 mV to 5 V in amplitude and has a bandwidth of 200 MHz. The B port outputs 2 mV to 1 V has a bandwidth of up to 1 GHz. The B port is used because of the wide bandwidth. The polynomial waveform generator is used to generate the RF chirp necessary to drive the optical Mach-Zehnder intensity modulator. The MZM specifications have already been introduced in Section 3.4. To program the Analogic 2045 digital waveform generator, the following command is input using the keypads:

"AT +TRIG TO +TRIG RPT 1 (FOR 200u 0.5*(0.75 + 0.25*t/200u)*SIN(100M*t + 0.5*260M/200u*t*t)) CLK 1.25n."

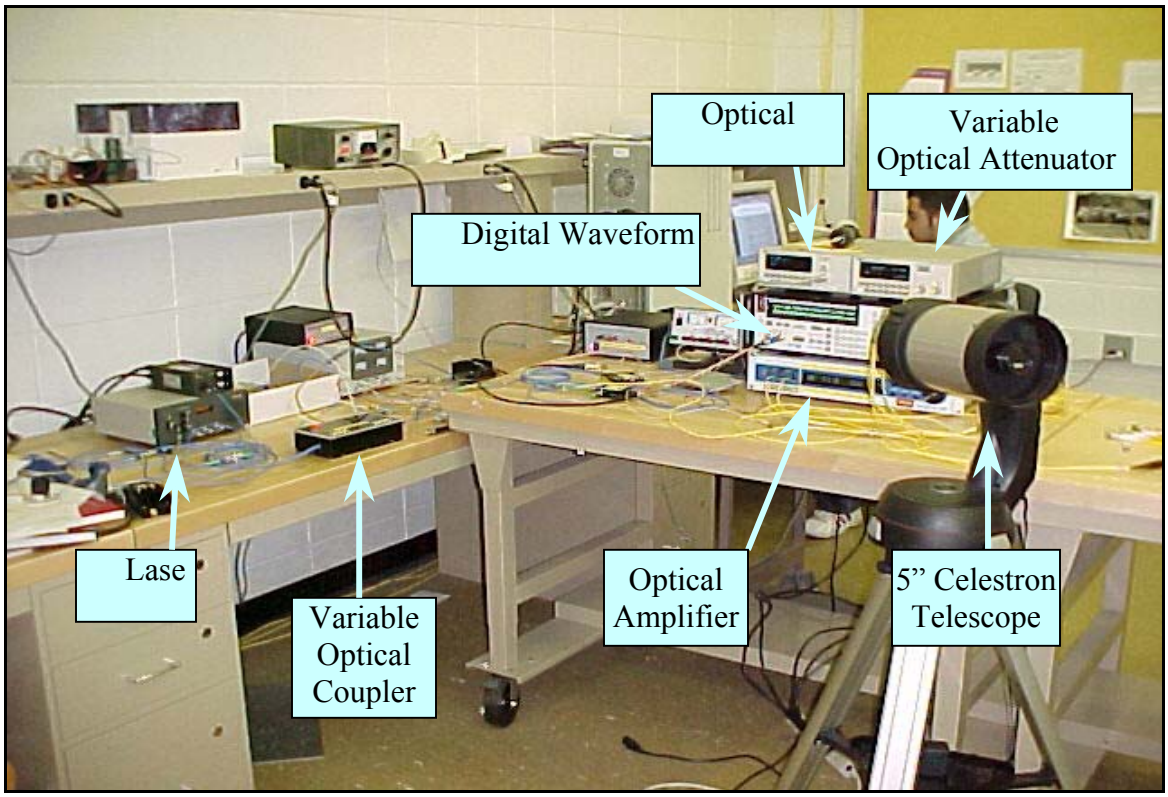

Figure 4.1.1. Laser radar laboratory test setup.

The "AT +TRIG TO +TRIG RPT 1" command tells the onboard computer to start the signal output when an external active trigger or rising edge of the trigger is received, create the function once, and then stop and wait for the next trigger. As mentioned in Chapter 3, the trigger is supplied by the control card, which also synchronizes the data acquisition system. The following line "FOR 200u" sets the pulse duration, and "0.5*(0.75 + 0.25*t/200u)" is the amplitude weighting function. Finally, the rest of the term describes the chirp equation. "CLK 1.25n" simply forces the system to use an internal clock that works at 1.25 ns intervals or at 800 MHz.

For all the experiments conducted we used the following parameters (Table 4.1.1), unless stated otherwise:

Table 4.1.1 Parameters used in the experiments.

Parameter	Setting
Number of samples collected	2048 samples
Sampling frequency (f_S)	8 MHz
Chirp pulse duration (T)	200 μs
Chirp bandwidth (B)	260 MHz
Chirp start frequency (f_S)	100 MHz
Pulse repetition frequency (PRF)	1 kHz
Optical local oscillator power (P_{LO})	0 to -1 dBm

4.2 Roundtrip loss

To determine the loss incurred in coupling light from the MTP connector to the telescope and from the telescope back to the MTP connector, two laboratory tests were conducted. First, the laboratory setup shown in Figure 3.1.1, and the optics setup is shown in Figure 4.2.1, are used to measure coupling and free-space losses. Two of the adjacent fibers located in the center of the twelve-fiber MTP connector are used as separate transmitter and receiver. We found that by adjusting the telescope focus so that the reflected image superimposed on the faceplate is the same size as the faceplate, the received signal is maximized. A mirror is placed 4 m away from the faceplate of the telescope. A visible light source from an optical fault locator is used to launch light into the telescope. The light projected onto the mirror is reflected back into the telescope. The visible light allows us to focus the telescope so the reflected image size is superimposed on the faceplate of the telescope.

In the second laboratory experiment, the telescope and the mirror are replaced by a piece of 40 m long fiber connecting the transmit and receive path of the test setup; see Figure 4.2.2.

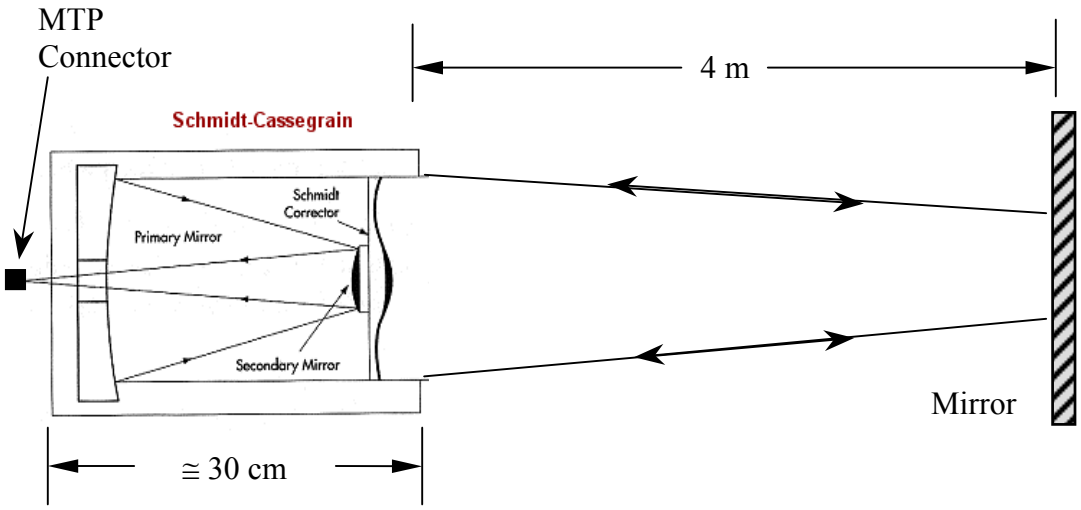

Figure 4.2.1 Free-space test setup (copied from Celestron®

http://www.celestron.com/schmidt.htm).

The transmit or optical signal power is varied using the optical attenuator in steps of 2 dB in the two laboratory setups mentioned previously. The results of the two tests conducted without incoherent integration are shown in Figure 4.2.3. From Figure 4.2.3, we can determine the roundtrip free-space loss due to the coupling of light into the telescope. Given a detected SNR, 20 dB for example, the optical signal power required to

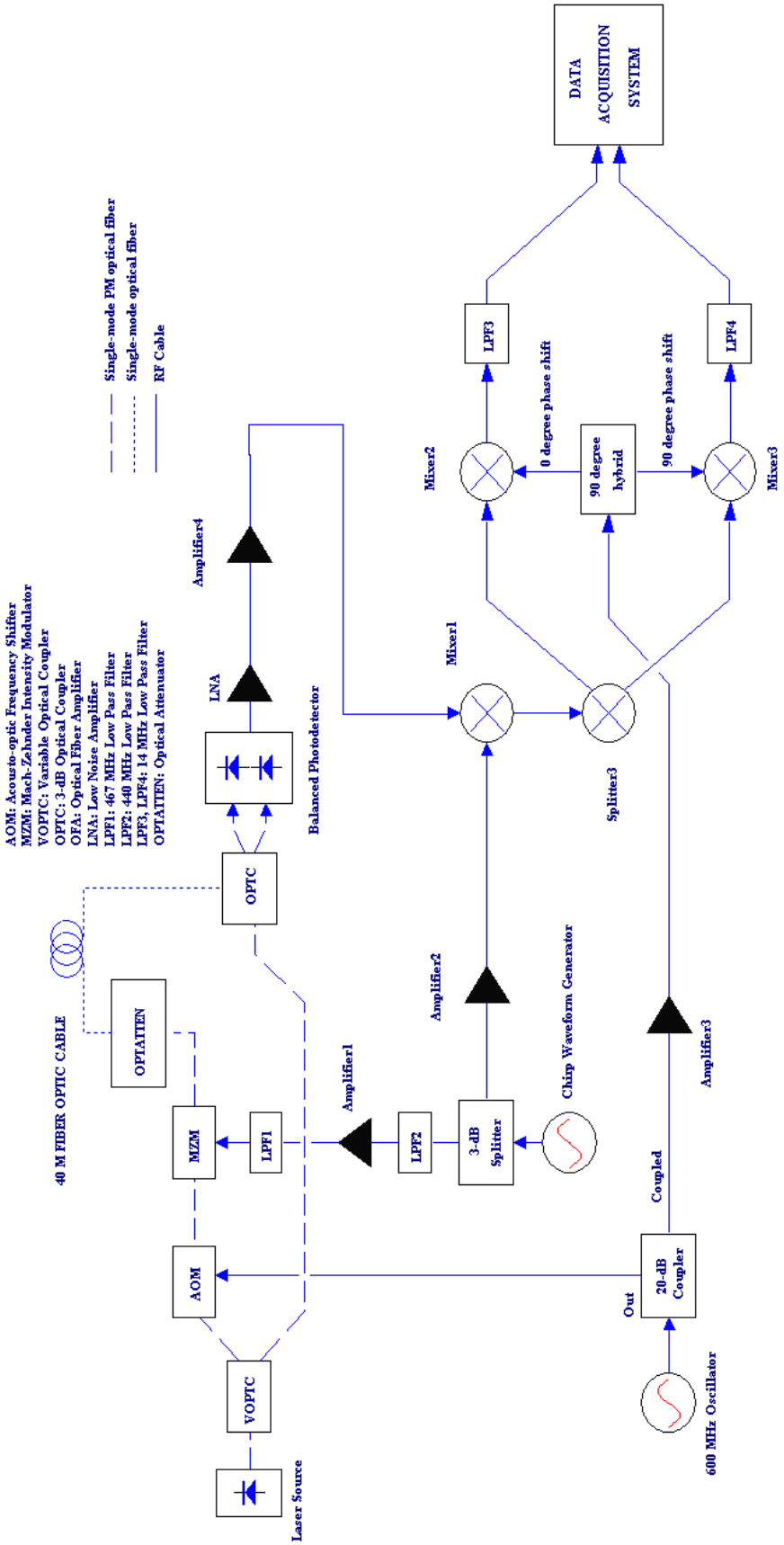

Figure 4.2.2 Block diagram for the breadboard laser radar fiber-to-fiber testing.

achieve this SNR will be around -80 dBm for the fiber loop-back case and -36 dBm for the mirror target test. Hence, the difference in signal power for a given SNR will be losses due to coupling and free-space losses. The loss in our case is around 44 dB. Note, however, that the loss measurement includes both coupling and propagation losses.

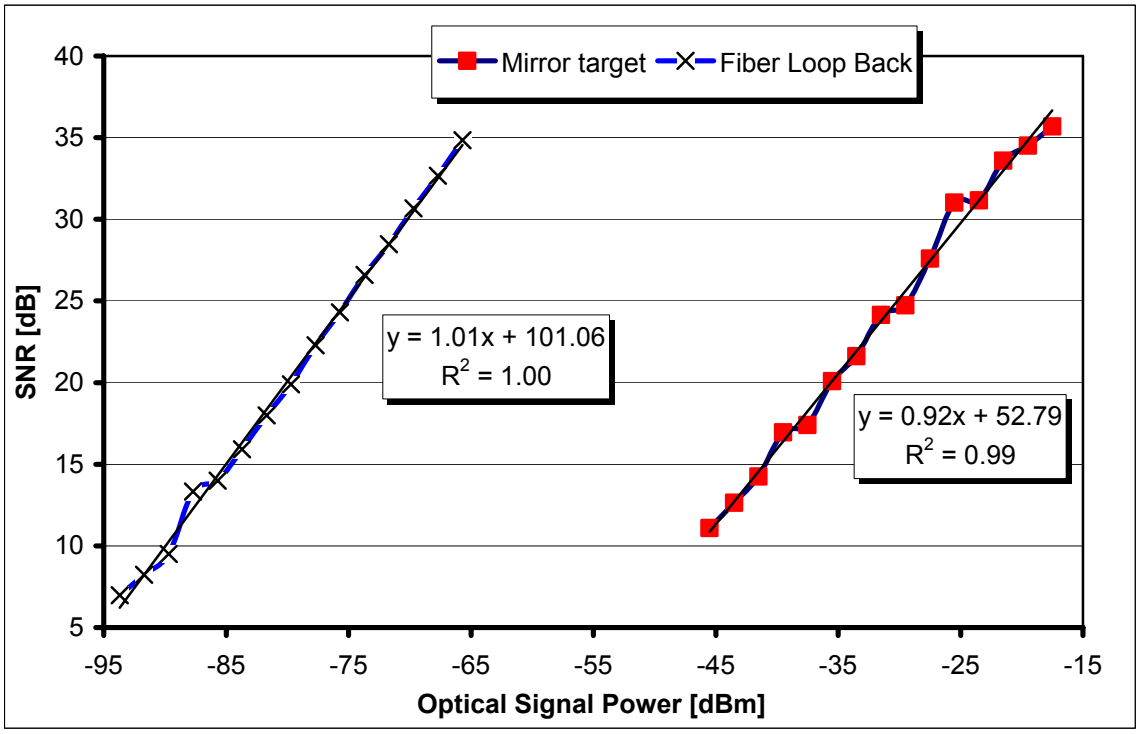

Figure 4.2.3 Determination of roundtrip free-space loss using SNR.

4.3 MTP connector isolation

Since the MTP connector works for both the transmitter and receiver, and the transmit and receive fibers are adjacent to one another, the isolation between both fibers should be as high as possible so jamming does not become a significant problem. Figure

4.3.1 shows the isolation between the fibers. The transmit signal is launched from fiber position 1, and the receive fiber is moved sequentially away from the transmit fiber (position 2, then position 3, etc.). The isolation is between 90 dB and 104 dB. This result implies that there are many applications we can implement, which we will discuss later.

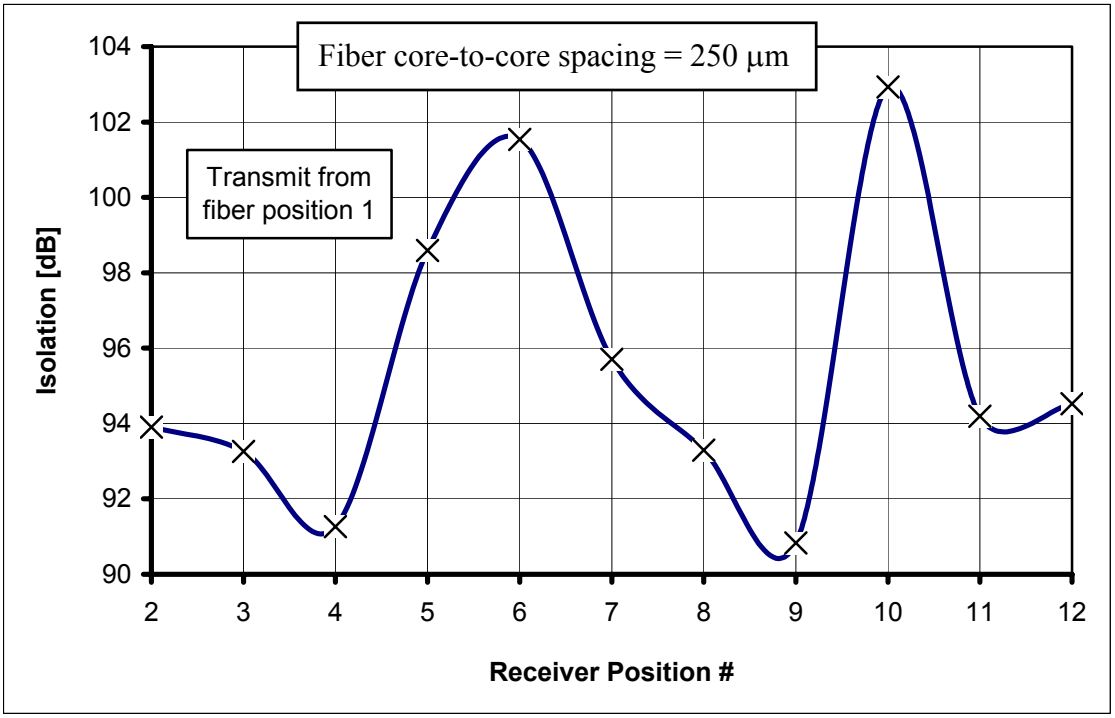

Figure 4.3.1 Receiver position versus isolation.

4.4 Receiver performance in terms of SNR

An important test of the laser radar and receiver performance is a signal-to-noise ratio test. The test setup used is as shown in Figure 4.2.2, where a 40 m single-mode fiber connects the transmit to the receive path of the test setup (fiber-to-fiber connection or, similarly, loop-back configuration). The optical attenuator is changed in 2 dB steps of attenuation for every measurement taken. The received power is digitized and recorded

using the data acquisition system. The data are then signal processed in Matlab. A sample of the collected data processed using Matlab and plotted is shown in Figure 4.4.1. The frequency spike at 328 kHz is the chirp beat frequency after the dechirping process.

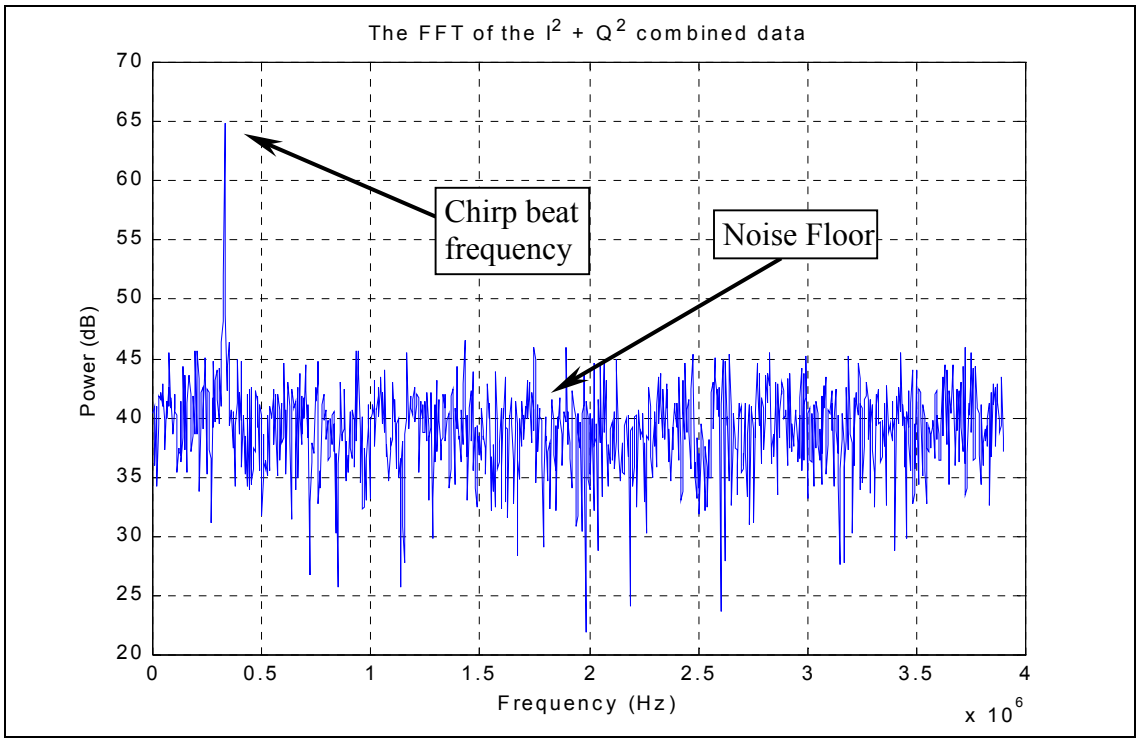

Figure 4.4.1 Matlab-processed data.

As explained in Chapter 3, the in-phase and quadrature detection signal processing is done in Matlab, where the in-phase and the quadrature dechirped data are first transformed into the frequency domain, squared, and then summed.

The plot of the collected data for the in-phase and quadrature detection system with the loop-back configuration in terms of signal-to-noise ratio, detected signal power and noise floor with respect to optical transmit power is given in Figure 4.4.2. The plot shows that the noise floor remains the same, at about 39 dB, as the optical transmit power

is increased. This is to be expected since the optical transmit power is very low compared to the optical local oscillator power, which is at around 0 dBm to -1 dBm, and the system is shot noise limited due to the high optical LO power.

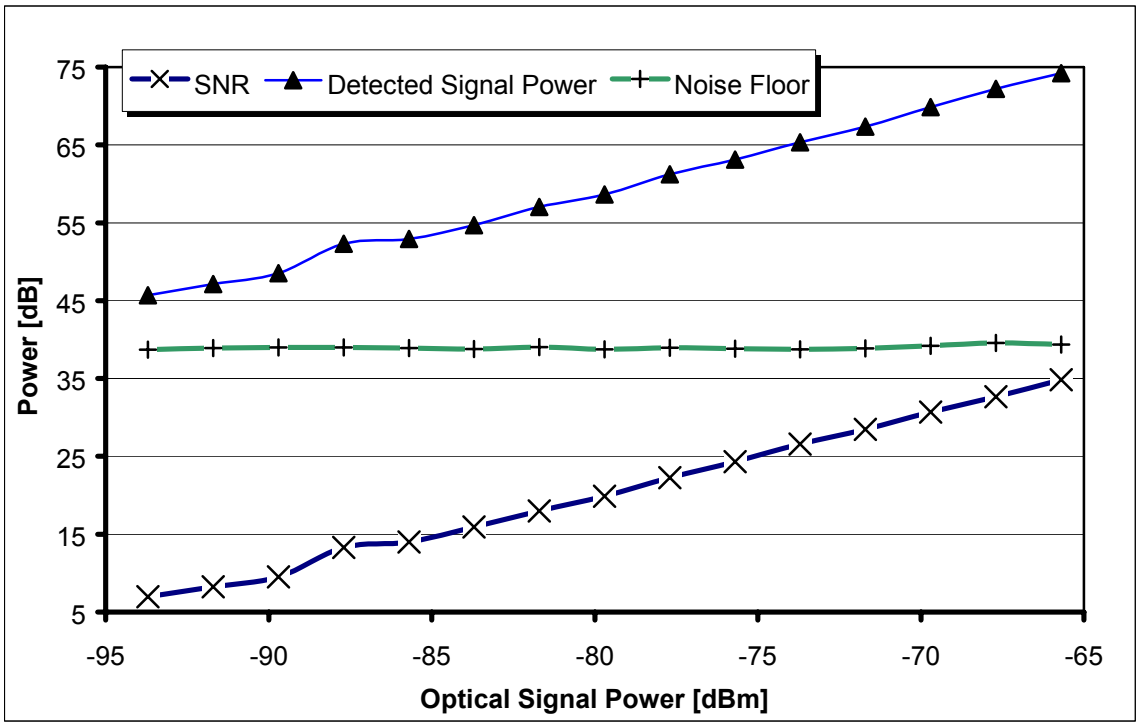

Figure 4.4.2 Relationship between SNR, detected receive signal power, noise floor and optical signal power.

Furthermore, the shot-noise contribution from the signal power is insignificant as compared to the additive shot noise from the optical LO and thermal noise. The detected signal power is the signal power obtained after taking the sum of the square of the in-phase and quadrature detected signals and then converting to dB. The process is shown below:

$$\text{detected signal power} = 10\log_{10}\left(I^2 + Q^2\right)$$

The plot also shows that the minimum signal power that can be detected is around -94 dBm.

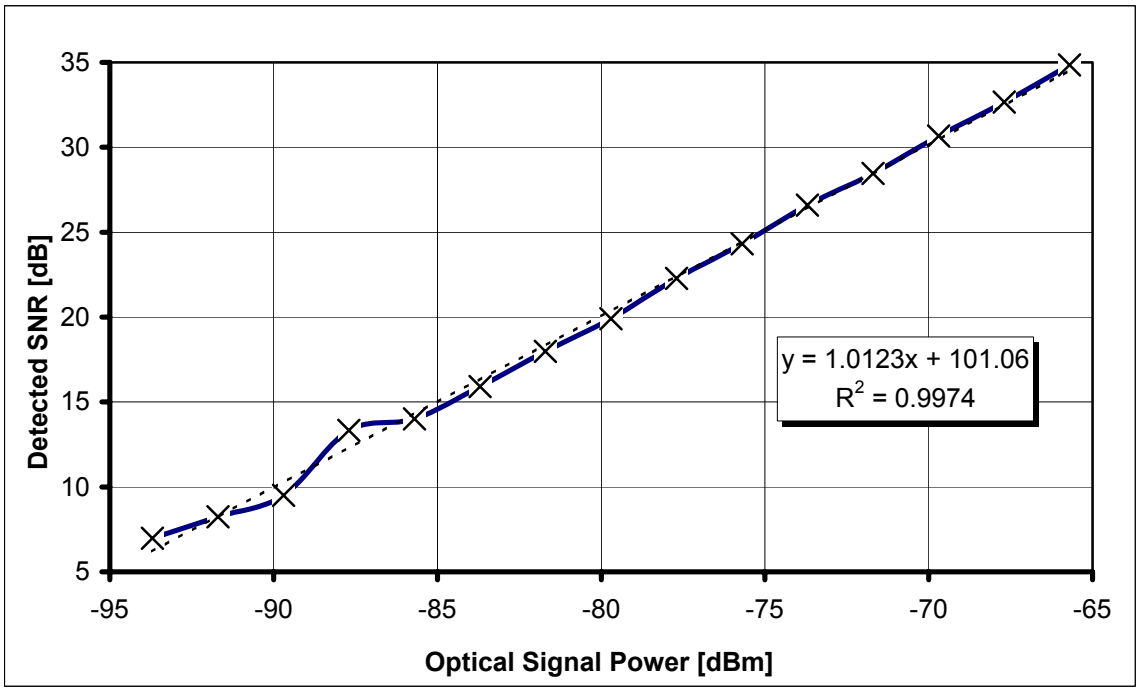

Figure 4.4.3 Signal-to-noise ratio characteristic with respect to optical signal power.

The same data set is plotted again in Figure 4.4.3, but only the signal-to-noise ratio is plotted against the optical signal power. The plot shows that there is a one-to-one or a linear relationship between the optical signal power and the detected signal-to-noise ratio.

In order to verify that there is a direct relationship between the pulse duration and the detected signal power (and, inherently, the SNR once the noise floor is known), the same experiment setup shown in Figure 4.2.2 is used. The optical transmit power is fixed at -66.5 dBm or 224 pW. The effect of varying the pulse duration on the detected signal

is plotted in Figure 4.4.4, where the noise floor, detected signal power, and signal-to-noise ratios are plotted against the chirp pulse duration.

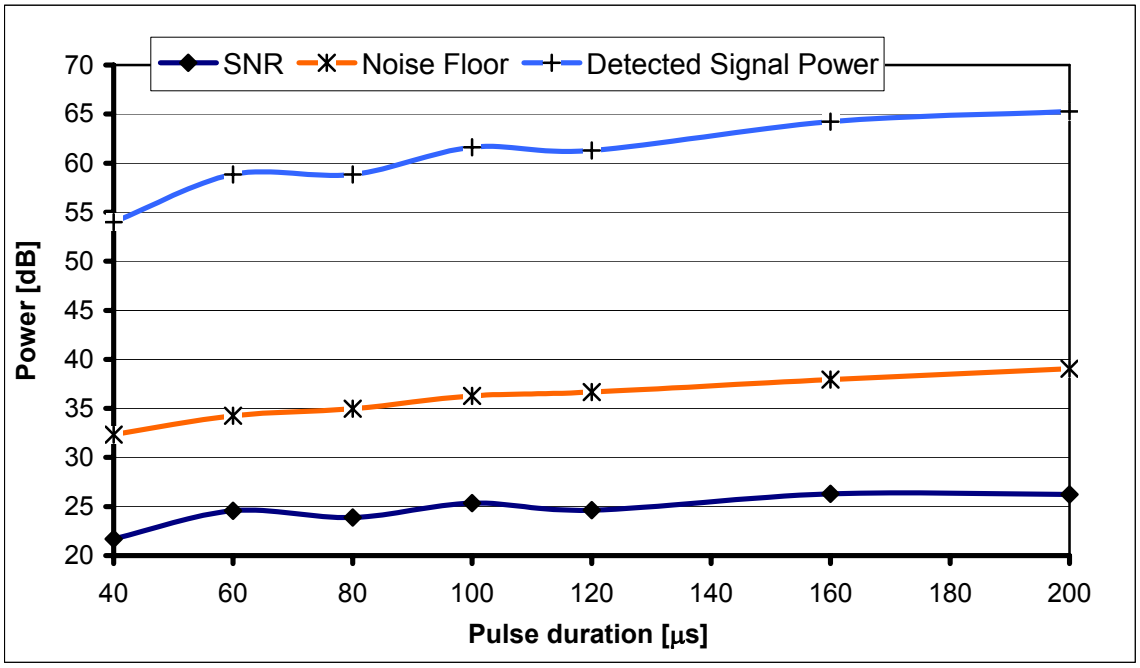

Figure 4.4.4. Effect of chirp pulse duration on the detected signal.

Figure 4.4.4 shows that the noise floor increases by about 7 dB, going from a 40 µs to a 200 µs pulse width. This is to be expected since increasing the pulse duration means that we are looking at more photons as the duration increases. The detected signal in Figure 4.4.5 shows that, as the pulse duration is doubled, the detected signal power also increases by 3 dB or is doubled.

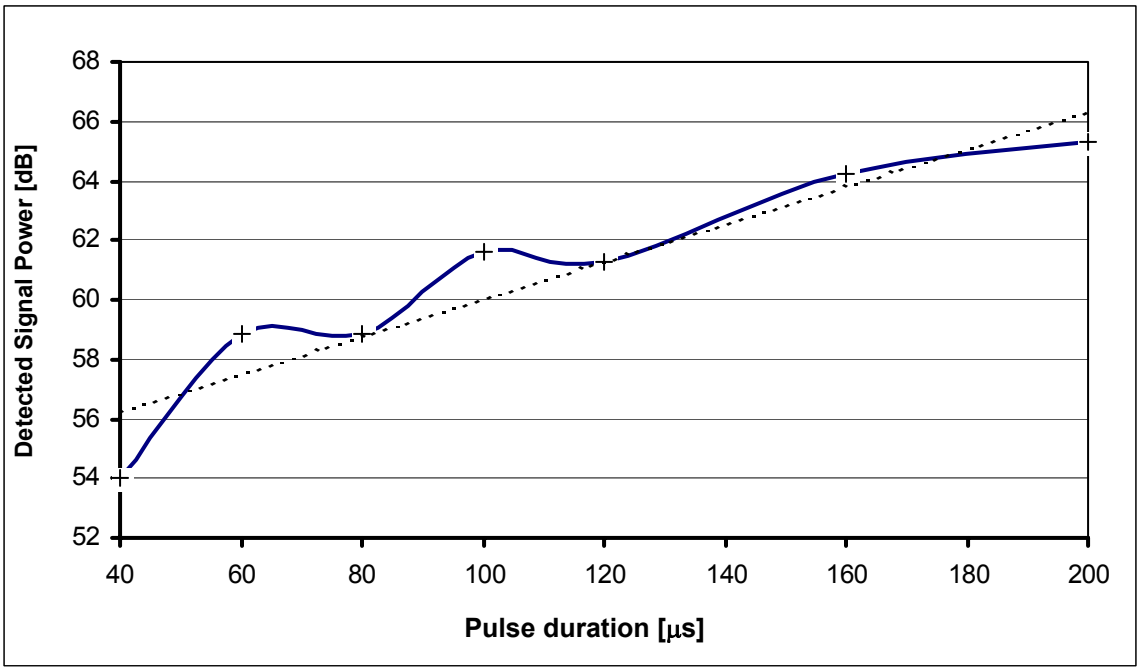

Figure 4.4.5 The effect of chirp pulse duration on the detected signal power.

4.5 Testing the laser radar performance using various type of targets

Short range testing

Now that we have characterized the laser radar system, we can turn our attention to working with different types of targets. So far we have been using a specular target (a mirror) to maximize the return power (assuming that the mirror is a perfect reflector). In this section, we introduce diffuse targets: plain paper, rock, leaves, grass, snow, and asphalt. A diffuse target is, as defined in Chapter 2, a target that uniformly scatters in all directions. We assume that all the targets' surfaces are diffuse (Lambertian) surfaces. The different parameters for the experiment are tabulated in Table 4.2.1. We again found that the return signal is maximized by focusing the telescope to a point on the target as shown in Figure 3.6.2 (where a visible light is fed into the telescope and the projected image on the target is focused to a point), and we followed the same procedure throughout this

section. Figure 4.5.1 shows the detected return signal from a dead piece of brown leaf used as a target, without any incoherent integration. The optical transmit signal power measured at the output of the fiber optic amplifier is 13.5 dBm. The leaf was flattened out as much as possible to emulate a flat diffuse target. The range from the telescope to the target is approximately 4 m.

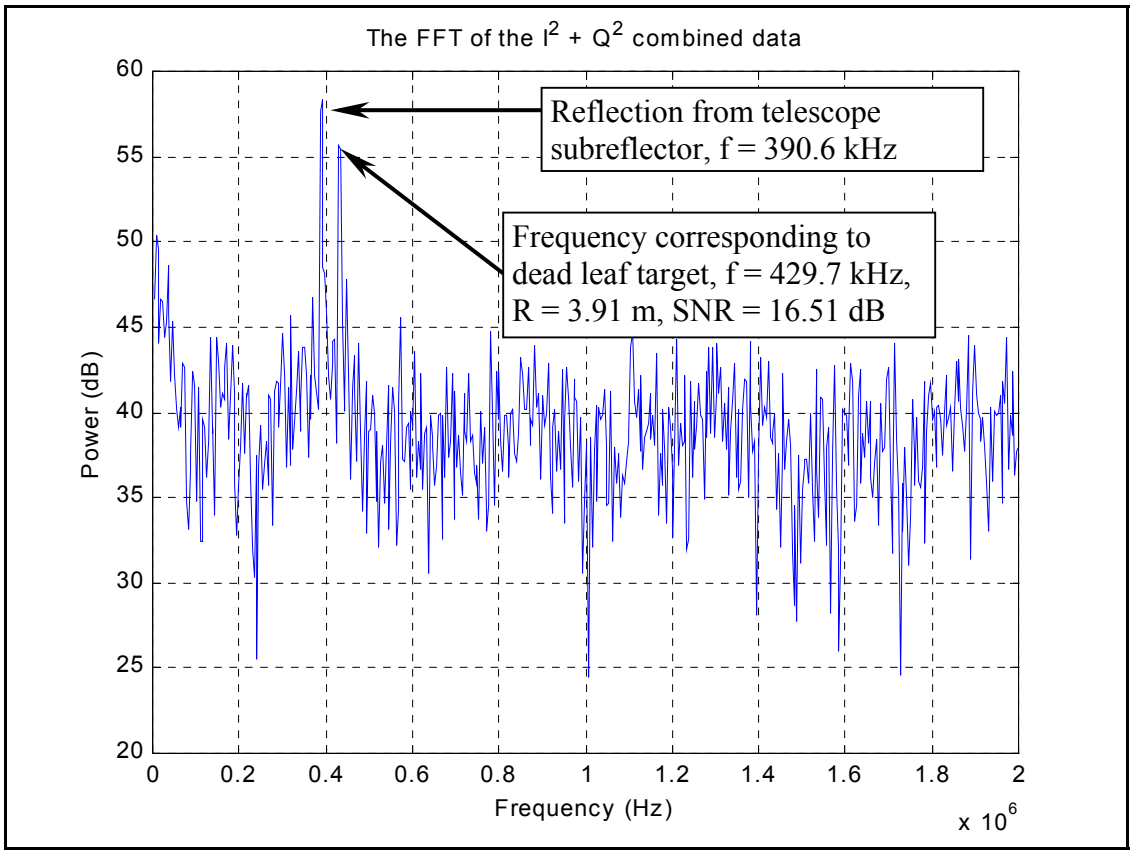

Figure 4.5.1 Detected signal for brown dead leaf without incoherent integration.

The first spike from the left at a frequency of 390.6 kHz is a result of internal reflection from the subreflector or the secondary mirror of the telescope. The second

frequency spike at 429.7 kHz corresponds to the return signal which the dead piece of leaf as the target.

The formula in (4.5.1) is used to verify that the frequency corresponds to the range. We take the difference in frequency between the return signal from the subreflector and the frequency corresponding to the real target, using the subreflector as a reference point. The distance between the subreflector and the fiber launch should not be more than 30 cm, as shown in Figure 4.2.1. As a result, we subtract 0.6 m (roundtrip distance) from the calculated range to account for this error. Figure 4.5.2 shows how the transmitted light is reflected off the secondary mirror.

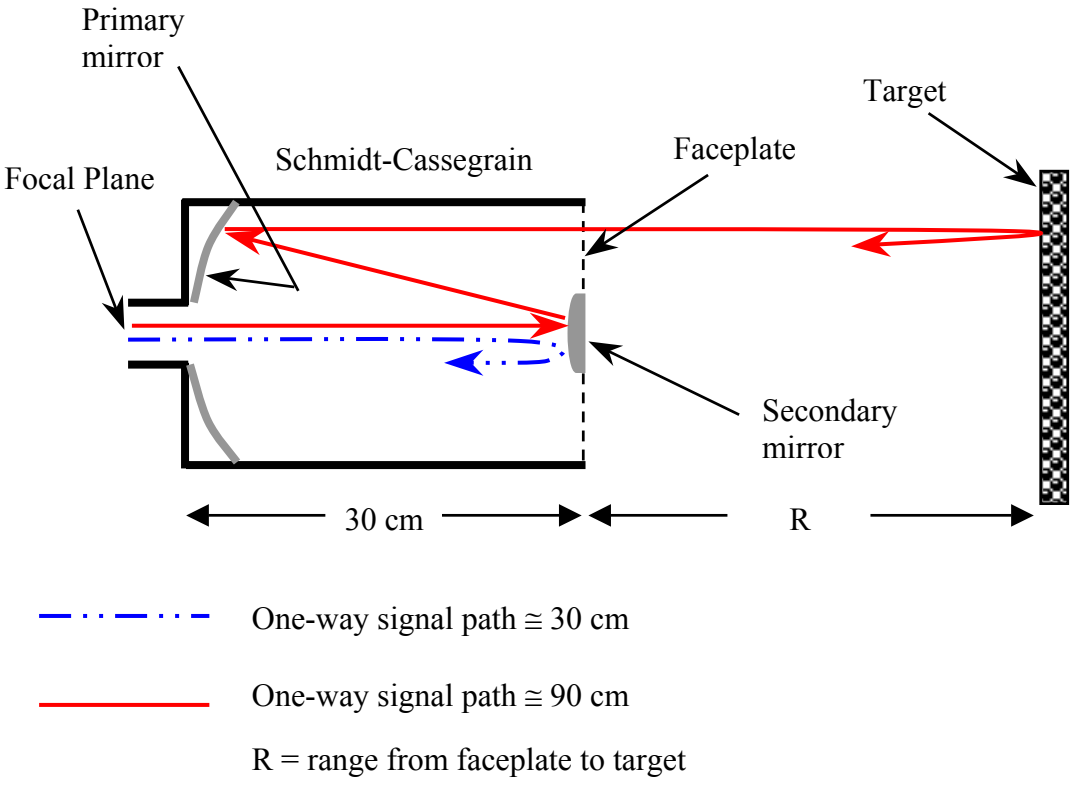

Figure 4.5.2 Internal reflection due to secondary mirror.

Equation (4.5.1) gives the range starting from the faceplate of the telescope to the target.

$$\text{Range, } R = \left\{ \frac{(F_t - F_{ref}) \times T \times c}{2 \times B} \right\} - 0.6\,[\text{m}] \qquad [4.5.1]$$

where,

F_t = frequency of target return signal [Hz],

F_{ref} = frequency of reflection from telescope [Hz],

T = pulse width [s],

c = speed of light, 3×10^8 m/s

B = chirp bandwidth [Hz].

Taking the target frequency from Figure 4.5.1 and using (4.5.1), we find that R = 3.91 m, and the return SNR is 16.51. The result from the target frequency in terms of range is quite close to that of the measured range of 4 m.

Next, we replaced the piece of brown leaf with a piece of green live foliage as a target. The Matlab data frequency display is shown in Figure 4.5.3. Again, we find that the frequency 433.6 kHz corresponds to 4.36 m range.

Then, the piece of live leaf was replaced by a piece of rock, without changing the range of the target. We see from Figure 4.5.4 that the detection frequency for the rock is not changed and remains at 433.6 kHz, and corresponds to 4.36 m.

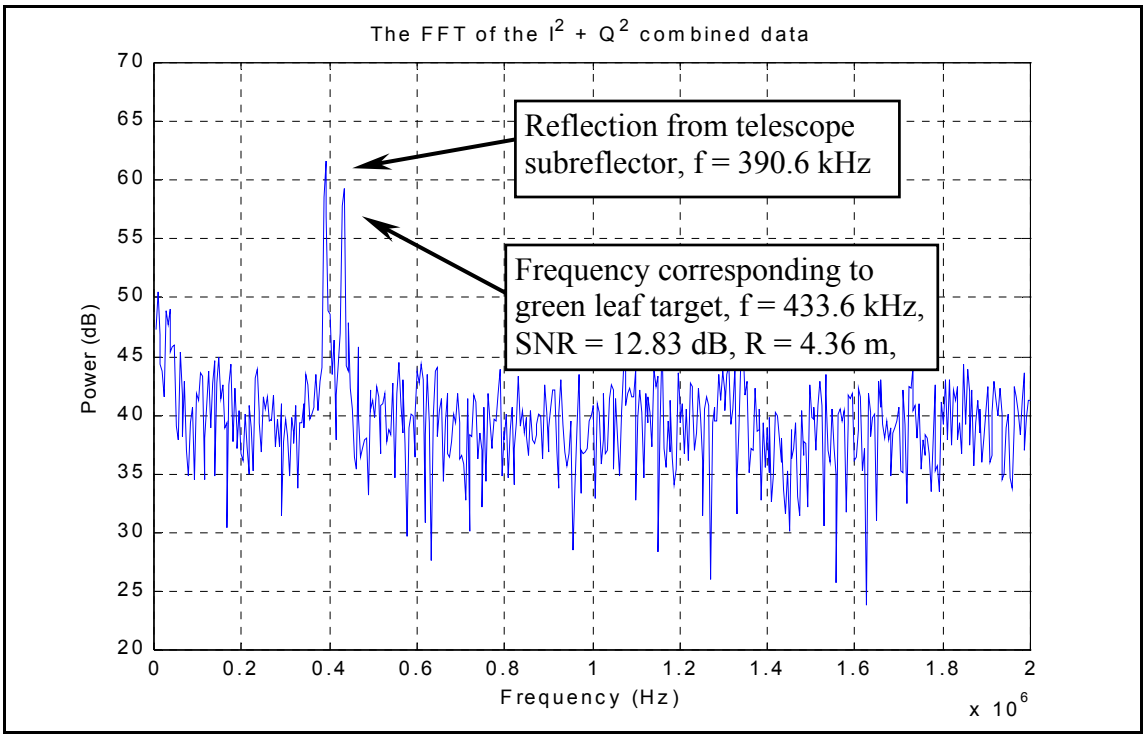

Figure 4.5.3 Detected signal for green live leaf without incoherent integration.

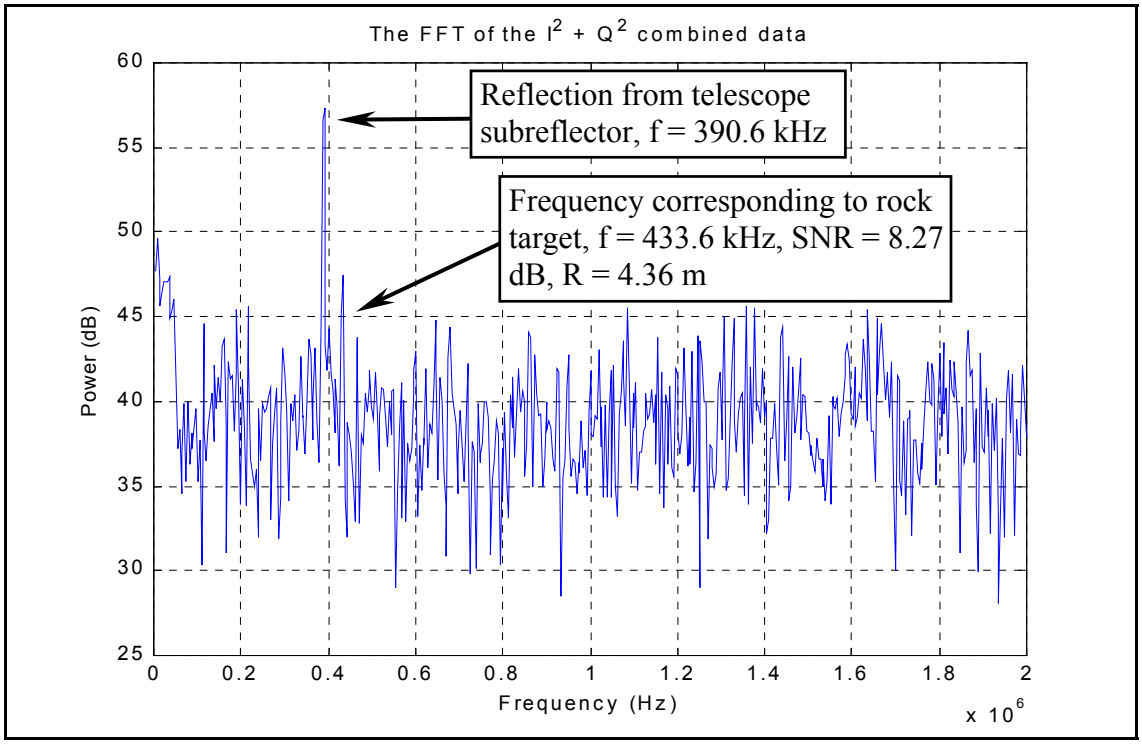

Figure 4.5.4 Detected signal for rock without incoherent integration.

Extended range testing

After testing the system in a laboratory setting, we extended the range to 20 m and 35 m. The telescope was set up to point out a third-floor window to view the asphalt, grass and snow below, as shown in Figure 4.5.5. The optical transmit power was readjusted to output 15 dBm and was measured at the output of the optical amplifier. The data collected from asphalt at a range of about 20 m are shown in Figure 4.5.6. However, we see that the noise floor has a high variability, so, to decrease the variability of noise, we incoherently integrated the collected data set. The result is shown in Figure 4.5.7.

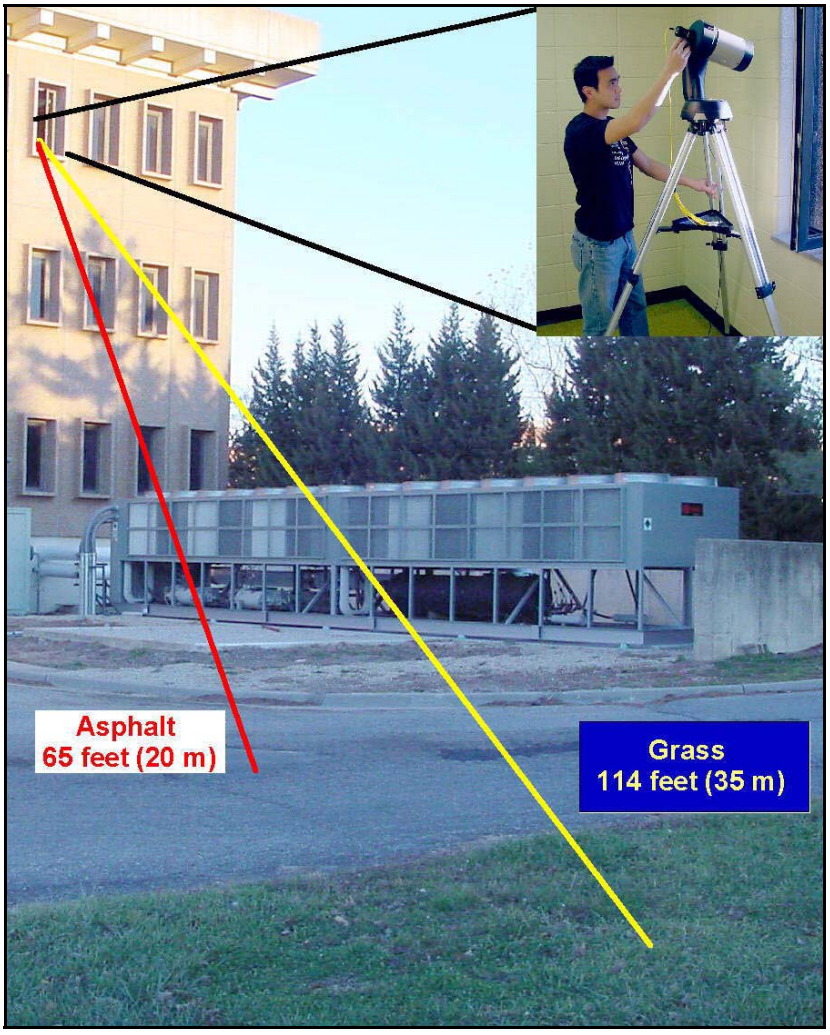

Figure 4.5.5 Ranges of different extended targets.

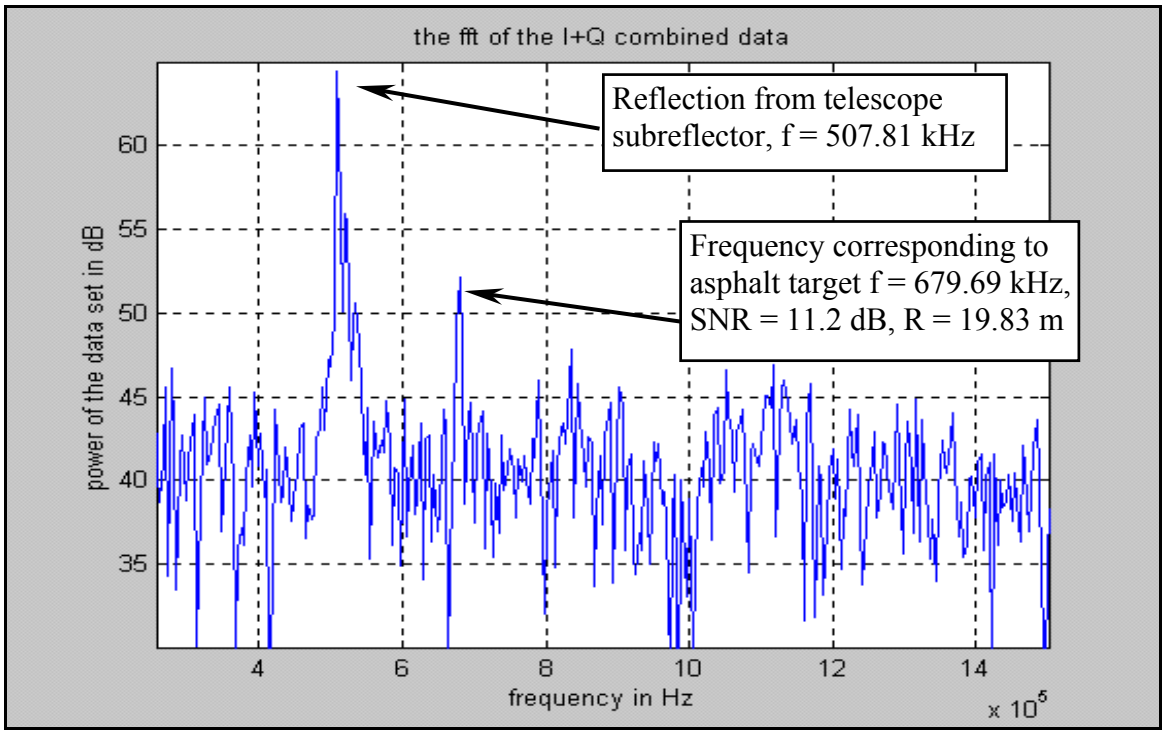

Figure 4.5.6 Detected signal for asphalt without incoherent integration.

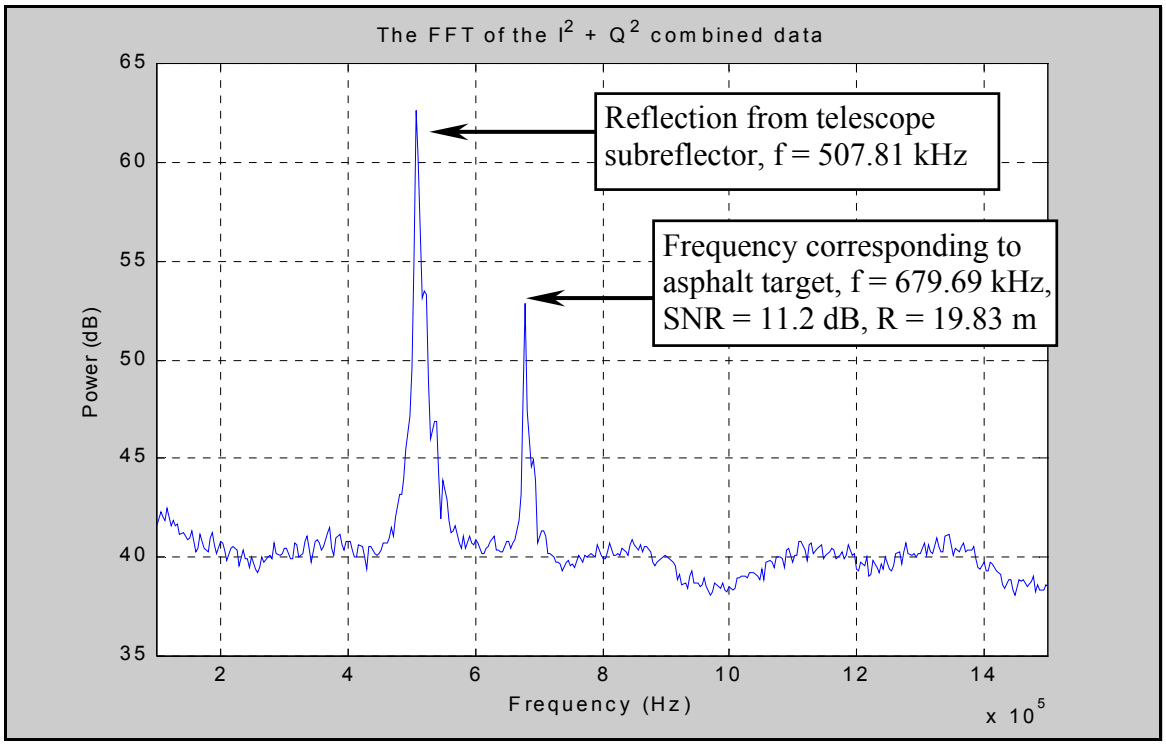

Figure 4.5.7 Detected signal for asphalt with 100 incoherent integrations.

By using Figure 4.5.7, calculation shows that the detected range is 19.83 m, which is very close to the actual measured distance of 20 m.

Then as Figure 4.5.8 shows, we moved the telescope to detect grass at the longer range of about 35 m. The detected signal for the grass target is given in Figure 4.5.8. With an SNR of 11 dB, the system detected a range of 35.61 m.

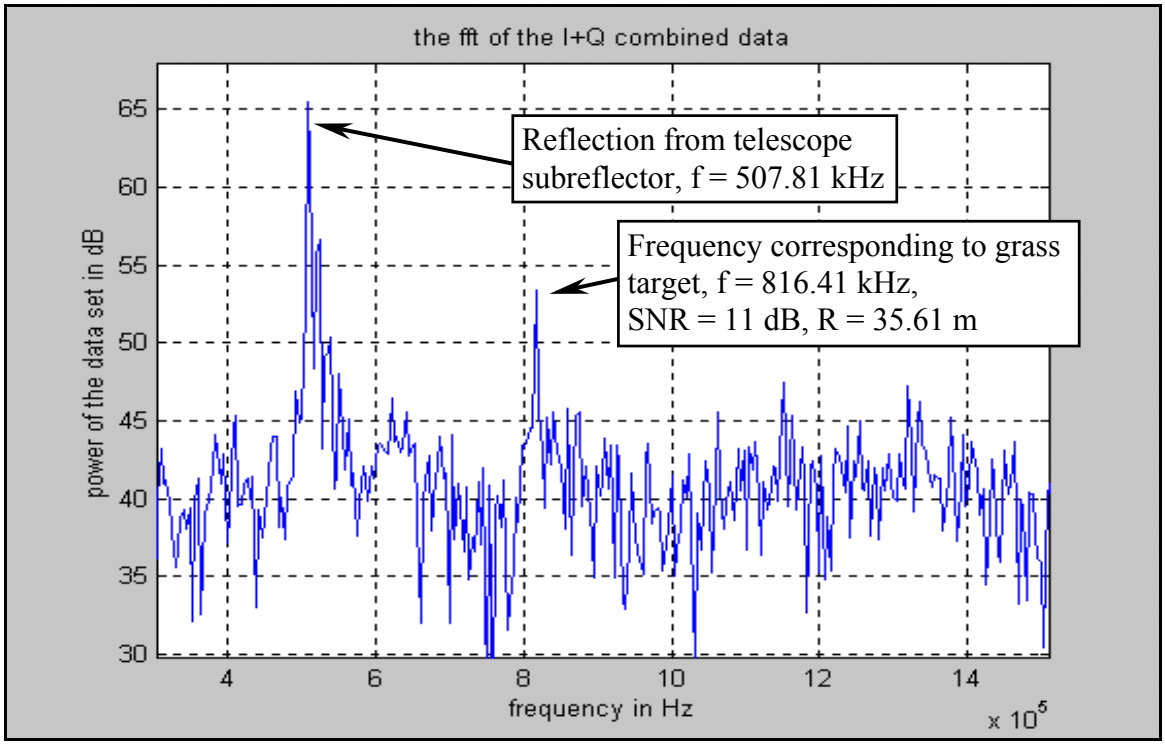

Figure 4.5.8 Detected signal for green grass.

The ultimate test for our prototype laser radar is measuring range with snow as the target. As Figure 4.5.9 shows, the snow was detected at a range of 21.6 m and has an SNR of 8 dB.

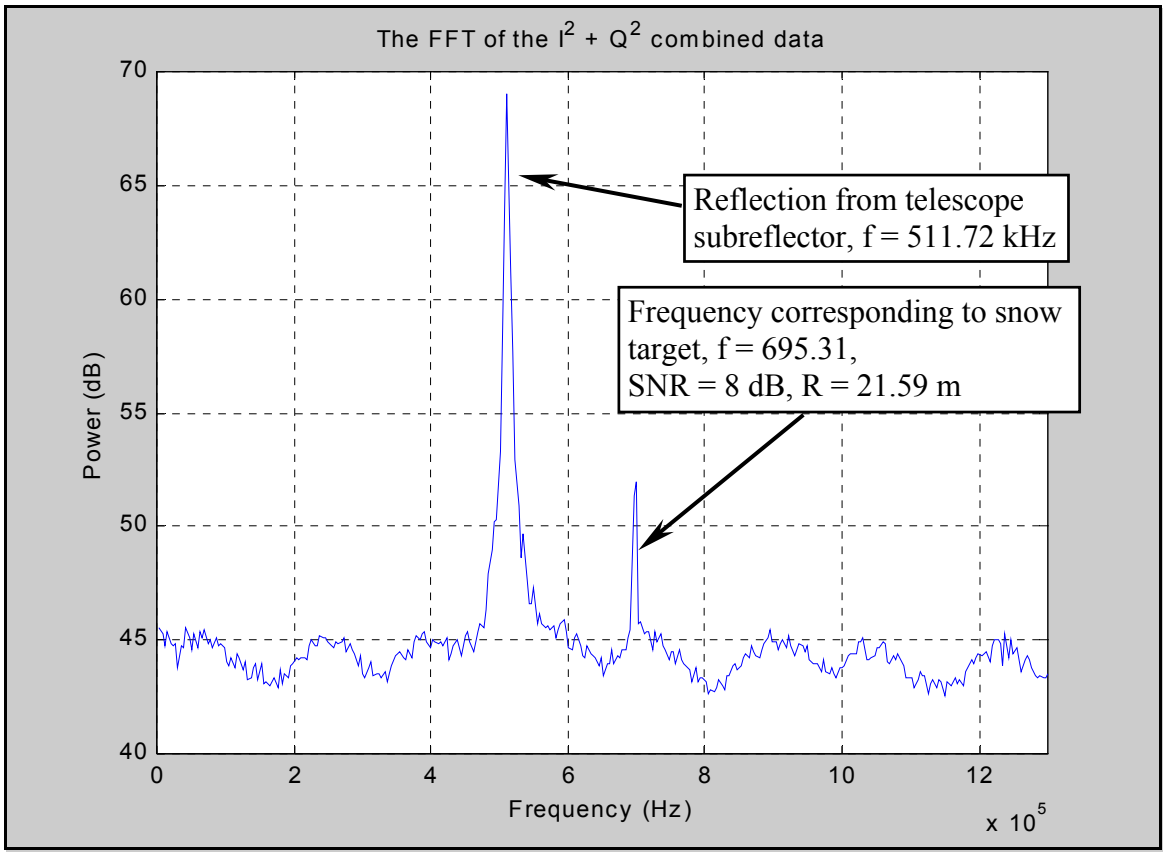

Figure 4.5.9 Detected signal for snow at 20 m range with 100 incoherent integrations.

A summary of the test results is given in Table 4.5.1.

Table 4.5.1 Summary of test results.

Target	Measured Range [m]	Tested Range [m]	Detected Signal Power [dB]	SNR [dB]	Noise Floor [dB]
Brown leaf	4	3.91	55.70	16.5	39.19
Green leaf	4	4.36	59.26	12.8	39.43
Granite rock	4	4.36	47.46	8.3	39.19
Asphalt	20	19.83	52.09	11.2	40.89
Grass	35	35.61	53.43	11.0	42.40
Snow	20	21.59	52.51	8	44.51

Variability of SNR with respect to range

An experiment was conducted to determine the variation in detected signal power and signal-to-noise ratio with regard to the range of the target. A plain piece of paper was placed in the telescope's line of sight. The piece of paper is moved by steps of 2 m away from the telescope, starting at 4 m and ending at 32 m. We had to focus the telescope so that a sharp point image was formed on the piece of paper. This is done by connecting a fiber optic visible fault locator to one of the fibers of the MTP connector. The optical transmit signal power measured at the output of the optical amplifier is 13.7 dBm. The plot of the detected signal power and signal-to-noise ratio versus target range is given in Figure 4.5.10.

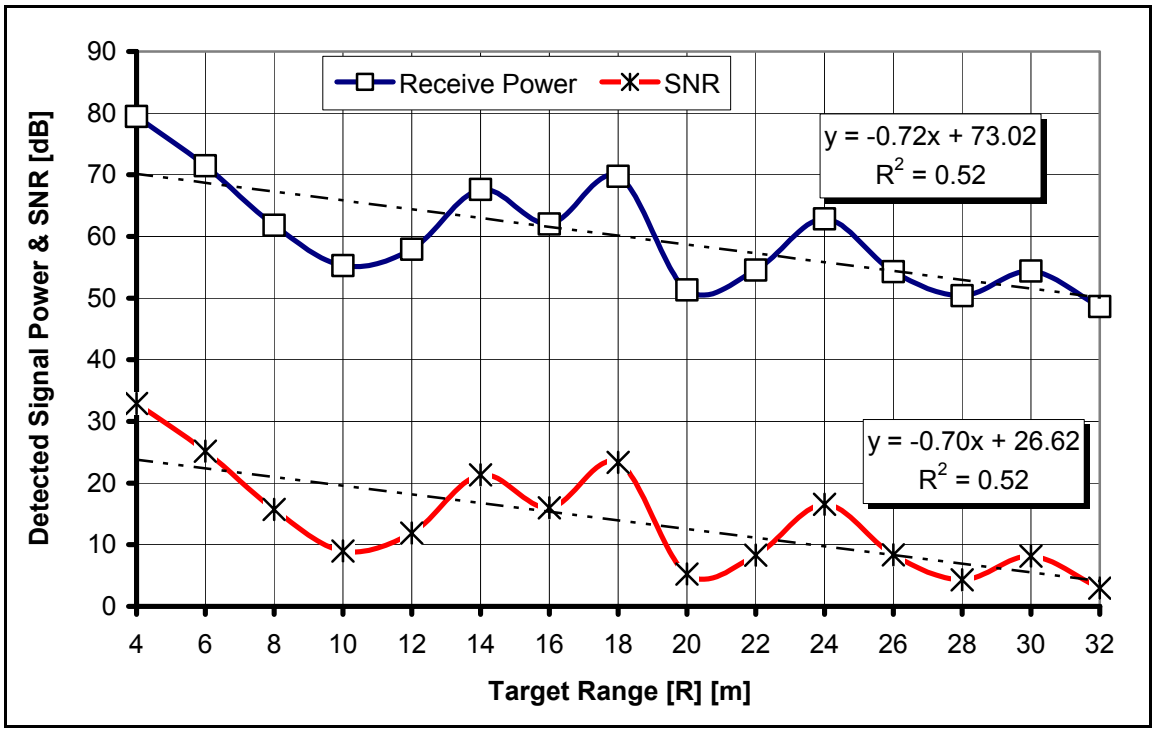

Figure 4.5.10 Plot of signal power versus range for plain—paper target (without incoherent integration).

Figure 4.5.10 shows the decrease in detected signal power and SNR as the target is moved further and further away. From the curve fit line, we see that for every 20 m increase in range, the detected signal power decreases by 10 dB. Figure 4.5.10 is plotted again, but this time the detected signal is plotted against the logarithm of the range; the plot is shown in Figure 4.5.11.

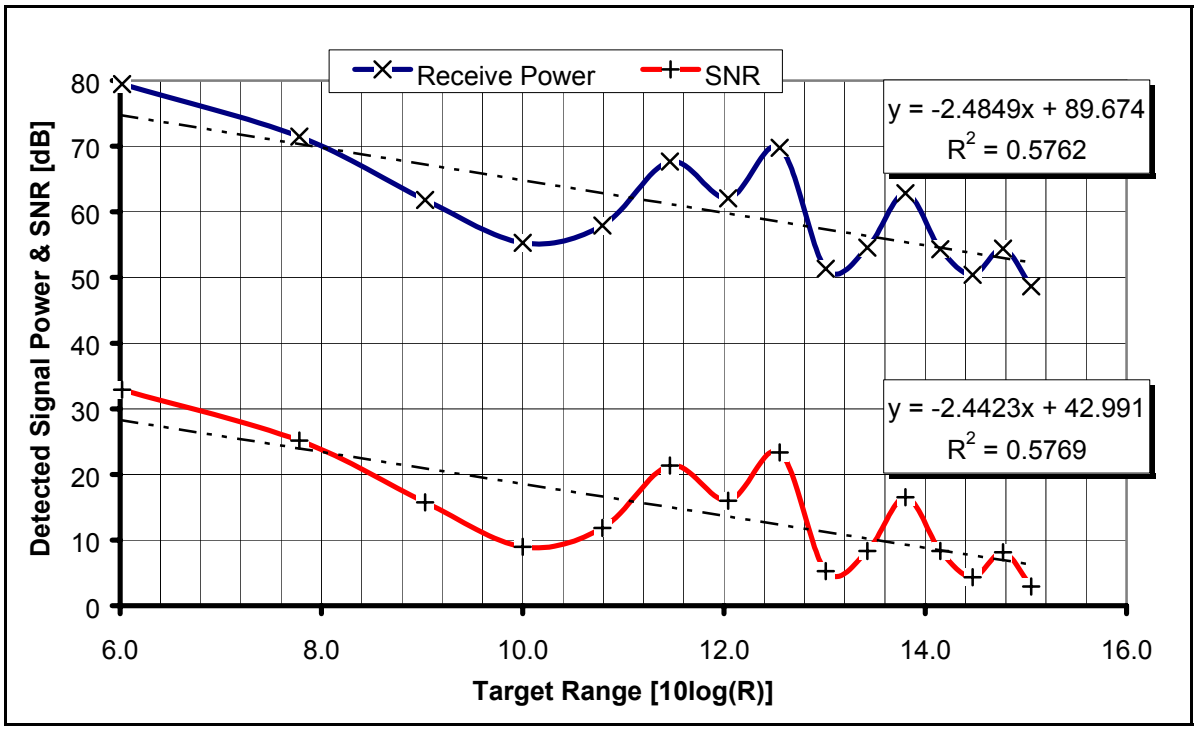

Figure 4.5.11 Power versus logarithm of range for plain paper target (without incoherent integration).

Another plot of the data set is shown in Figure 4.5.12 using 100 incoherent integrations. This lowers the variability of noise in the signal processing. We see, in Figure 4.5.12, that the slope of the curve has become less steep and the detected signal power does not decrease as quickly. Furthermore, the curve line fit shows that the detected signal power and SNR have a range-squared dependence.

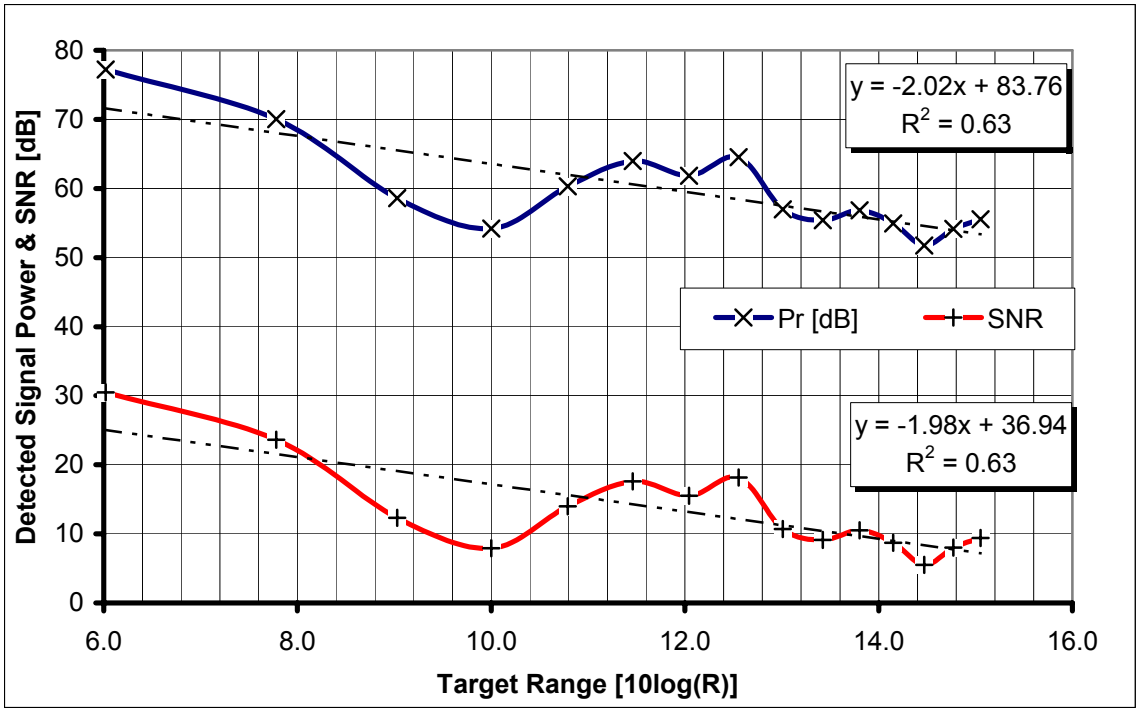

Figure 4.5.12 Range squared dependence of detected signal power and SNR for plain paper target (with 100 incoherent integrations).

The data we collected should have shown a √M factor decrease in noise power as M number of return pulses are incoherently integrated. This is not to be the case because, as Figure 4.5.7 and Figure 4.5.9 show, there is a periodic signal leakage into the data acquisition system. We see from the figures that the noise floor contains a periodic signal in the frequency domain, which suggests that a periodic signal in the time domain exists and is being leaked into the data acquisition system.

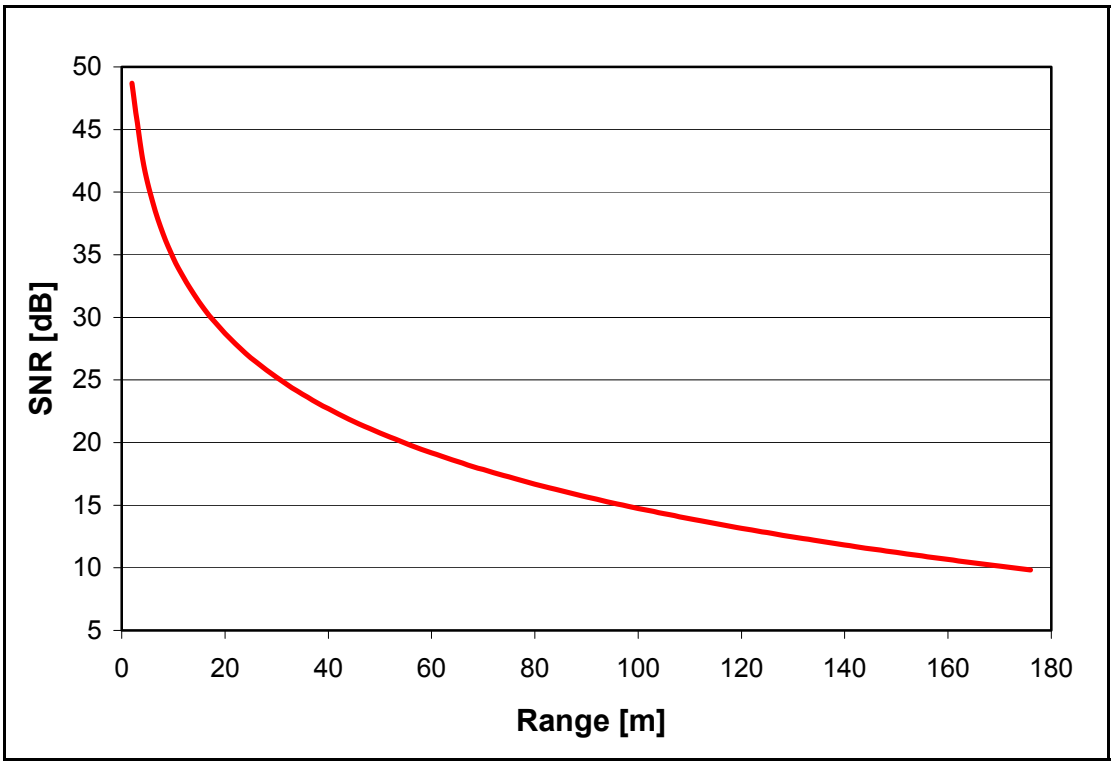

Figure 4.5.12 Theoretically obtained SNR for different ranges.

Table 4.5.2 Parameters used in theoretically calculated SNR.

Parameters	Values used
P_T	13.7 dBm (0.0234 W)
D	0.127 m (5 in.)
η_{ATM}	1
η_{SYS}	0.5
ρ_T	1
$\Re$	1 A/W
P_{lo}	0 dBm/ 1 mW
q	1.6×10^{-19} C
k	1.38×10^{-23} J/K
T	273 K
R	50 Ω

Figure 4.5.13 shows the theoretical SNR change with range, and Table 4.5.2 shows the parameters used to calculate the SNR. First, the received power was calculated using (2.2.6):

$$P_R = \frac{P_T \rho_T \pi D^2}{(4R)^2} \times \eta_{ATM}\ \eta_{SYS}$$

Then, the coherent detection SNR was calculated using (2.5.4) by substituting P_T with P_{sig}:

$$SNR_{coh} = \frac{\left(2\Re\sqrt{P_{sig}P_{lo}}\right)^2}{2B\left[\Re q\left(P_{sig} + P_{lo}\right) + 2kT/R\right]}$$

We see that the SNR at 24 m range is calculated to be about 27 dB. As a comparison, we see that at the measured SNR for a 24 m range target is 10 dB from Figure 4.5.10. There is a 17 dB decrease in SNR. This decrease is due to the fiber-telescope coupling losses. Furthermore, we see from Figure 4.5.13 that the theoretical range that would yield a 10 dB SNR is about 170 m and this value is obtained if there are no fiber-telescope coupling losses.

CHAPTER 5

OTHER CONCEPT IMPLEMENTATION AND FINDINGS

In the course of developing and testing the breadboard laser radar system, we tried several different approaches to increase the sensitivity of the system. This chapter reports the tests and findings we did on the various techniques we investigated.

5.1 Polarization diversity receiver

The return optical signal, after passing through free space, will be depolarized as the optical signal is scattered off a diffuse target. When the return signal is mixed with the local oscillator, the relative alignment of the state of polarizations (SOPs) will affect the resultant signal at the output of the coupler. To solve this polarization problem, we use a polarization diversity receiver, which detects all incoming SOPs equally. Figure 5.1.1 shows what a typical polarization diversity receiver looks like, and Figure 5.1.3 shows the implementation of the polarization diversity receiver in the breadboard laser radar system. The idea is to split the received signal and the LO along two orthogonal polarization axes, using the polarization splitters. Then the return signal and LO outputs with identical SOPs (defined arbitrarily as either parallel or perpendicular, as shown in figure 5.1.2) are combined and photodetected independently. A 45° polarization rotator is used to rotate the linearly polarized optical LO so that the SOP is 45° between the parallel and perpendicular axes as shown in Figure 5.1.2. This is done so the LO power is split evenly in between the two coupler branches.

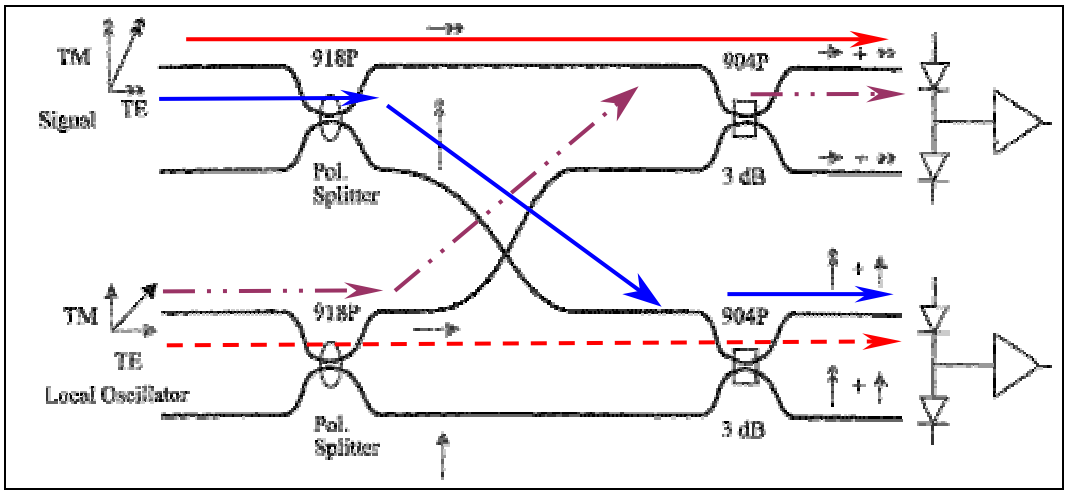

Figure 5.1.1 Polarization diversity receiver

(adapted from Canadian Instrumentation and Research, Ltd.).

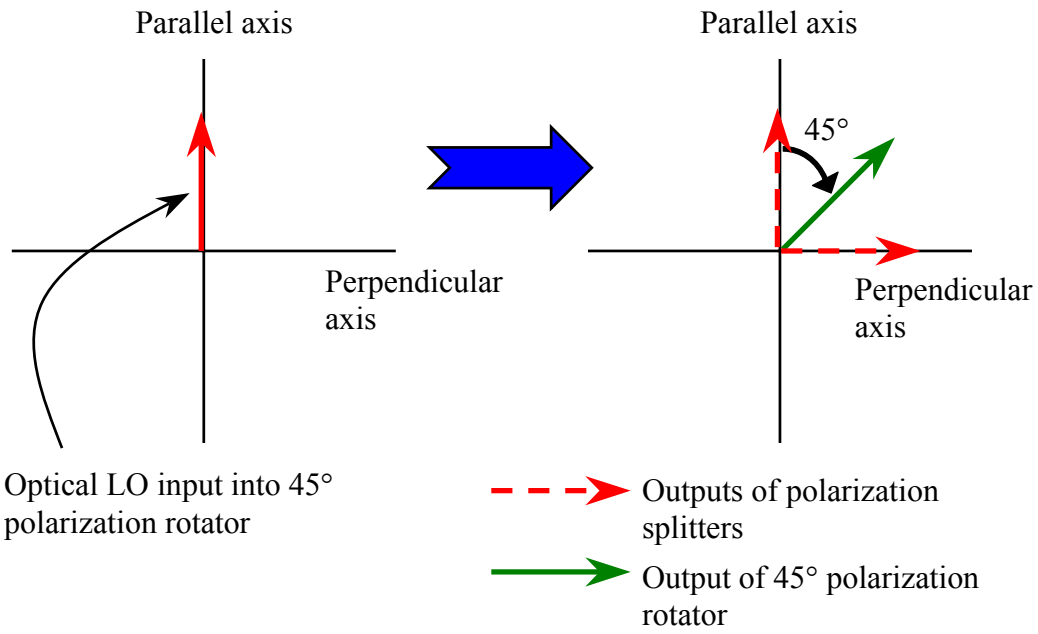

Figure 5.1.2 The SOP of the LO is split evenly along the orthogonal axes.

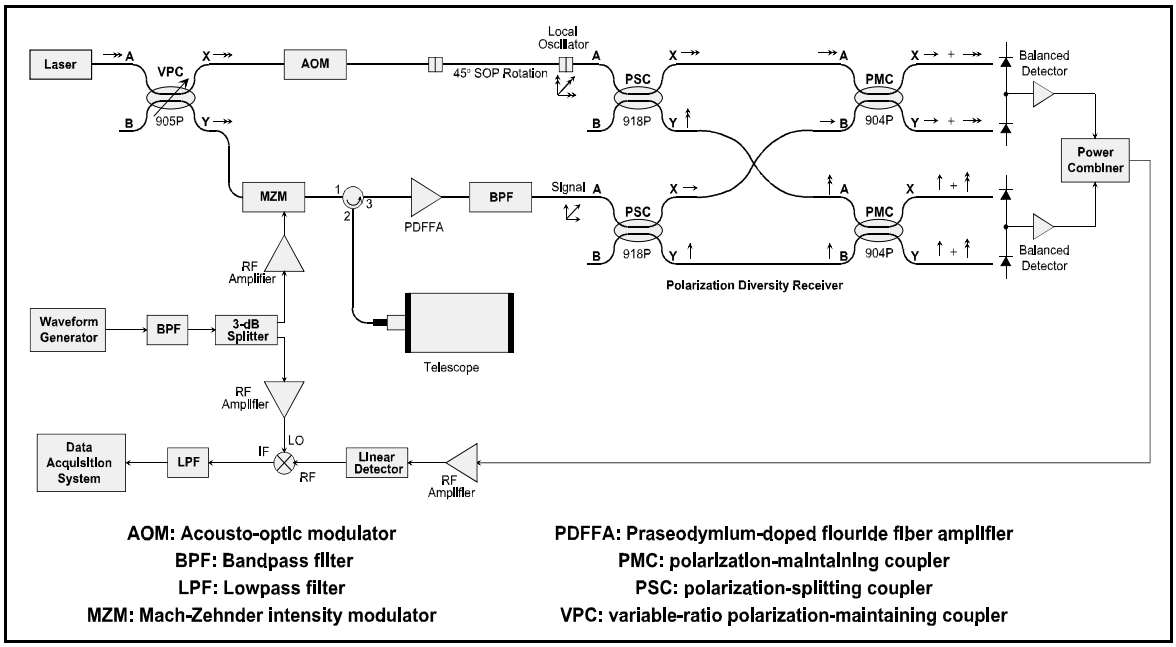

Figure 5.1.3 Polarization diversity receiver implementation in breadboard laser radar.

The use of the polarization diversity receiver ensures that the amplitude of the output signal does not change when the depolarized return signal is mixed with the local oscillator.

The only disadvantage of using this receiver in our system is the 6 dB power penalty. This is because in any one optical path, as shown by the red arrow in Figure 5.1.1, for example, the signal and optical LO go through a splitter (3 dB) and a coupler (another 3 dB). The same 6 dB loss is incurred for the blue arrow path and, similarly, the loss is the same for the other paths shown.

5.2 Superheterodyne detection

Envelope detection—the superheterodyne system

Figure 5.2.1 shows the implementation of the superheterodyne architechture, which makes use of the polarization diversity receiver and envelope detection. The

coherent receiver consists of the polarization diversity receiver and the balanced photodetector.

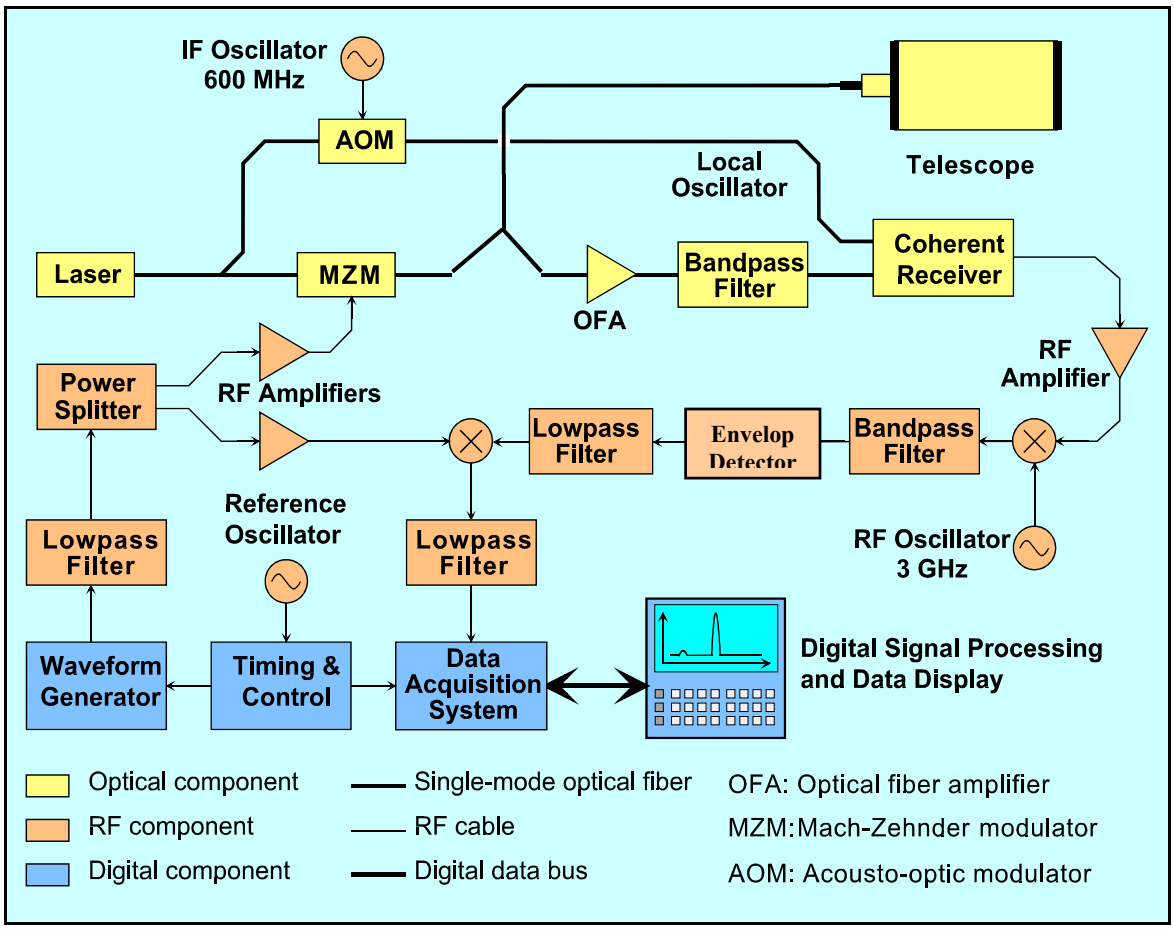

Figure 5.2.1 Block diagram of envelope detection test setup.

Envelope detection removes any phase fluctuation due to temporal correlation issues commonly associated with coherent laser remote sensing such as laser phase noise, atmospheric changes, and frequency shifting due to Doppler effects [7]. This is because the optical phase information contained in the optical carrier is discarded through envelope detection.

Envelope detection is accomplished using a Schottky-barrier diode detector working in the linear region. The output voltage versus input power of the linear detector is shown in Figure 5.2.2 for a 3.6 GHz tone input. For input powers greater than about -2 dBm input power onward, we see that the diode output voltage varies linearly with the input power and, below that input power, the output voltage varies non-linearly with the input power.

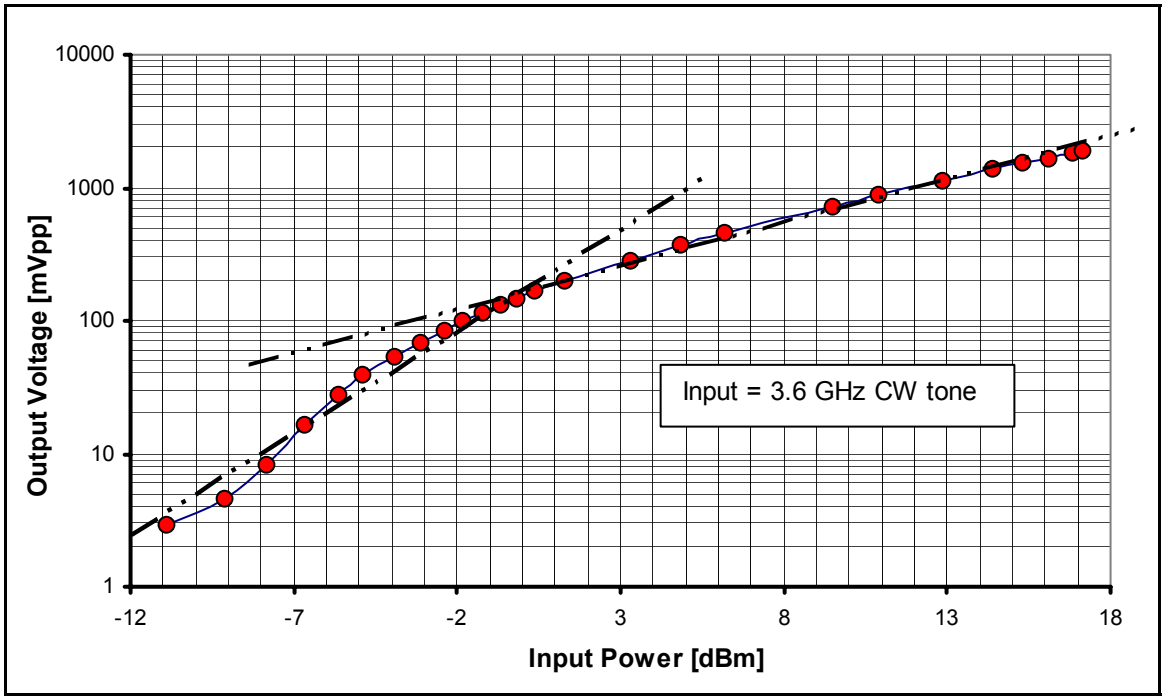

Figure 5.2.2 Schottky detector output voltage versus input power.

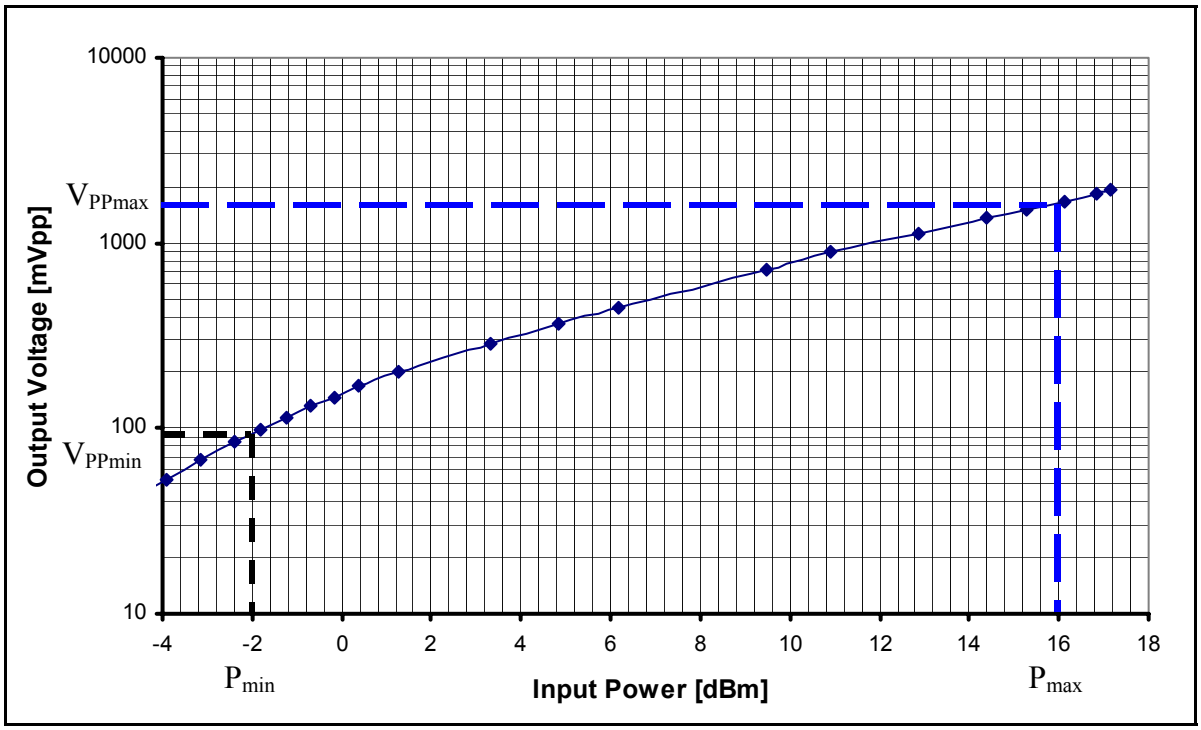

Figure 5.2.3 Linear range of the Schottky-barrier diode detector.

Figure 5.2.3 shows the linear range of the Schottky-barrier diode detector, and a picture of the linear detector is shown in Figure 5.2.4. To determine the linearity of the Schottky diode detector, the slope of the curve in Figure 5.2.3 within the linear range can be calculated as:

$$\text{Slope} = \{20\log_{10}(V_{Pmax}/V_{Pmin})\}/\{P_{max}/P_{min}\}$$

$$\therefore \text{ Slope} = \{20\log_{10}[600/80]\}/\{16-[-2]\}$$

$$= 17.5/18$$

$$\cong 1.0$$

where $V_{Pmax} = V_{PPmax}/2$, $V_{Pmin} = V_{PPmin}/2$. P_{max}, P_{min}, V_{PPmax} and V_{PPmin} are values as shown from Figure 5.2.3. Since the slope of the curve is one, the relationship between the input voltage, in dB, and the input power is a linear one-to-one relationship.

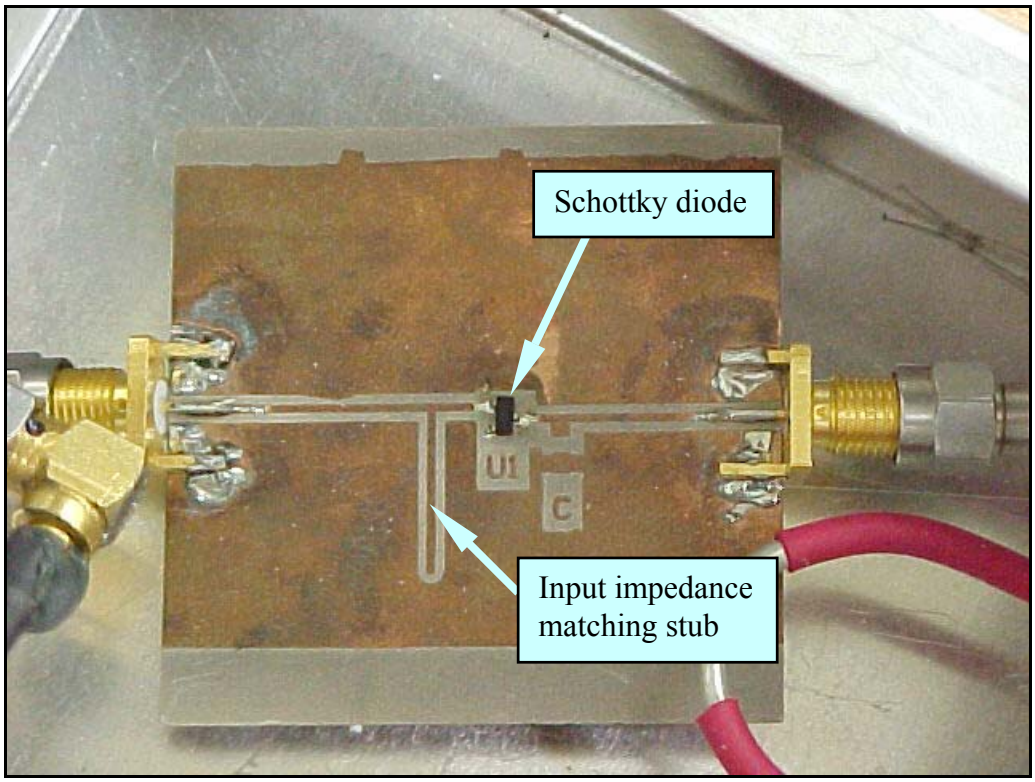

Figure 5.2.4 Schottky diode linear detector.

Envelope detection—SNR versus pulse duration tests

The characteristics of the envelope detection system were found using the test setup shown in Figure 5.2.1, except that the free-space segment was replaced with an optical attenuator and a loop-back fiber cable.

In the first experiment, we want to determine the signal-to-noise ratio variation with respect to chirp pulse width. The optical transmit power is kept constant at -27.3 dBm. Table 5.2.1 gives the parameters used in this experiment, and the result of this experiment is shown in Figure 5.2.5.

Table 5.2.1 SNR versus chirp pulse width experiment parameters.

Parameter	Setting
Sampling frequency (f_S)	8 MHz
Chirp bandwidth (B)	260 MHz
Chirp start frequency	100 MHz
Pulse repetition frequency (PRF)	20 kHz
Optical local oscillator power (P_{LO})	0 to -1 dBm
Number of samples	2048
Number of coherent integrations	256

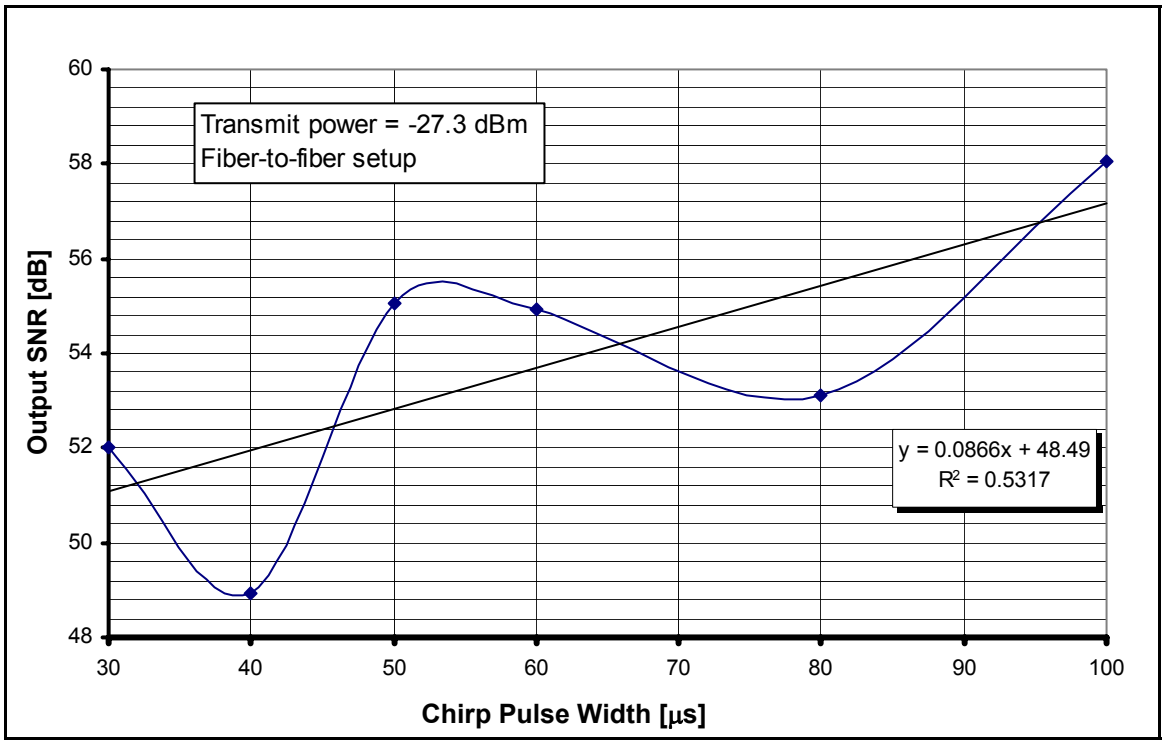

Figure 5.2.5 Variation of signal-to-noise ratio with input chirp pulse width.

As expected, we see that doubling of the chirp pulse width increases the output SNR by 3 dB, which shows a linear relationship between output SNR and pulse width.

Envelope detection—SNR versus number of coherent integrations

We conducted an experiment to evaluate the linearity of the output SNR with the number of coherent integrations. The result of this experiment is presented in Figure 5.2.6.

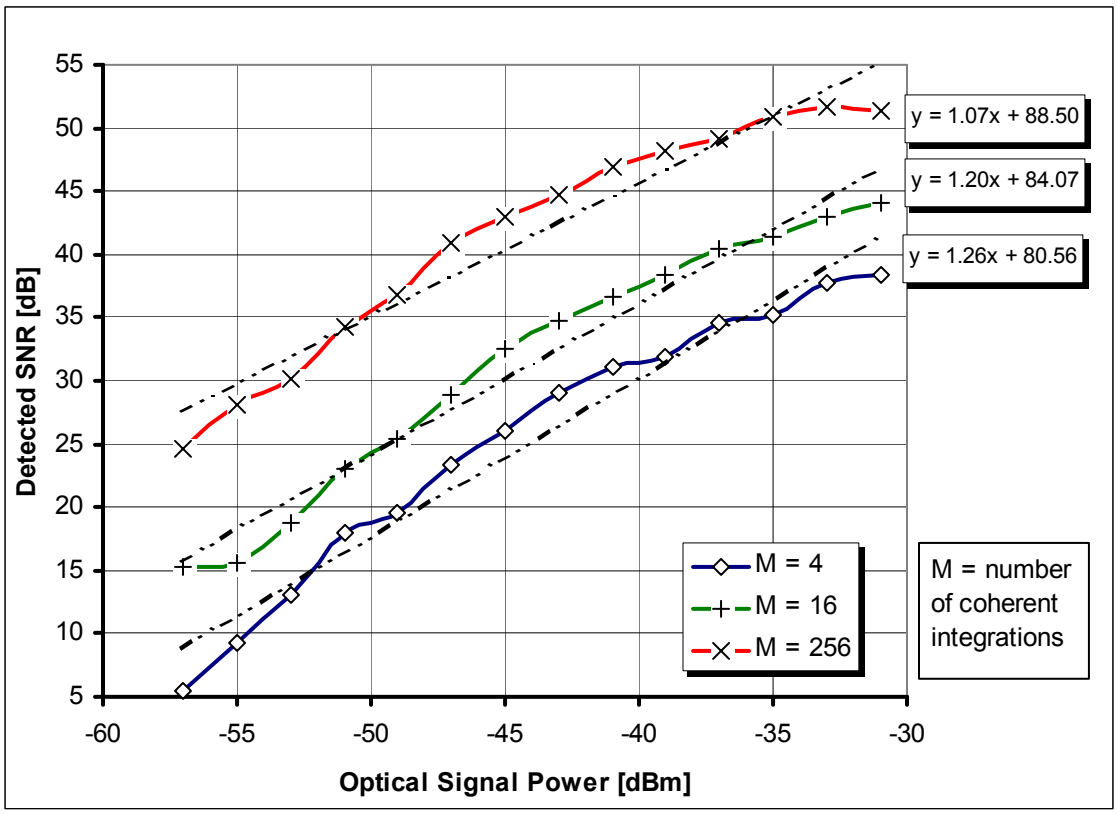

Figure 5.2.6 Improvement of SNR with increasing coherent integrations.

We see a linear relationship between the number of coherent integrations, M, and the SNR for a given optical signal power. From four coherent integrations to 16, there is an increase of about 5 – 6 dB, and from 16 integrations to 256, there is about a 10 – 12 dB increase. This is consistent with the theory that there is a one-to-one correlation between the number of integrations and the SNR improvement.

Envelope detection—roundtrip free-space loss measurement

The next experiment we conducted was the determination of the roundtrip loss incurred in transmitting from a collimator and receiving with a telescope. The optics test bench setup is shown in Figure 5.2.7. The collimator, which serves as the transmitting aperture, is placed about 50 cm away from the mirror. The receiver telescope is approximately 4 m from the mirror. The parameters for our experiments throughout this section are given in Table 5.2.2.

Table 5.2.2 System parameters used throughout all experiments.

Parameter	Setting
Sampling frequency (f_S)	8 MHz
Chirp pulse duration (T)	40 μs
Chirp bandwidth (B)	260 MHz
Chirp start frequency	100 MHz
Pulse repetition frequency (PRF)	20 kHz
Optical local oscillator power (P_{LO})	0 to -1 dBm
Number of samples per pulse	1024

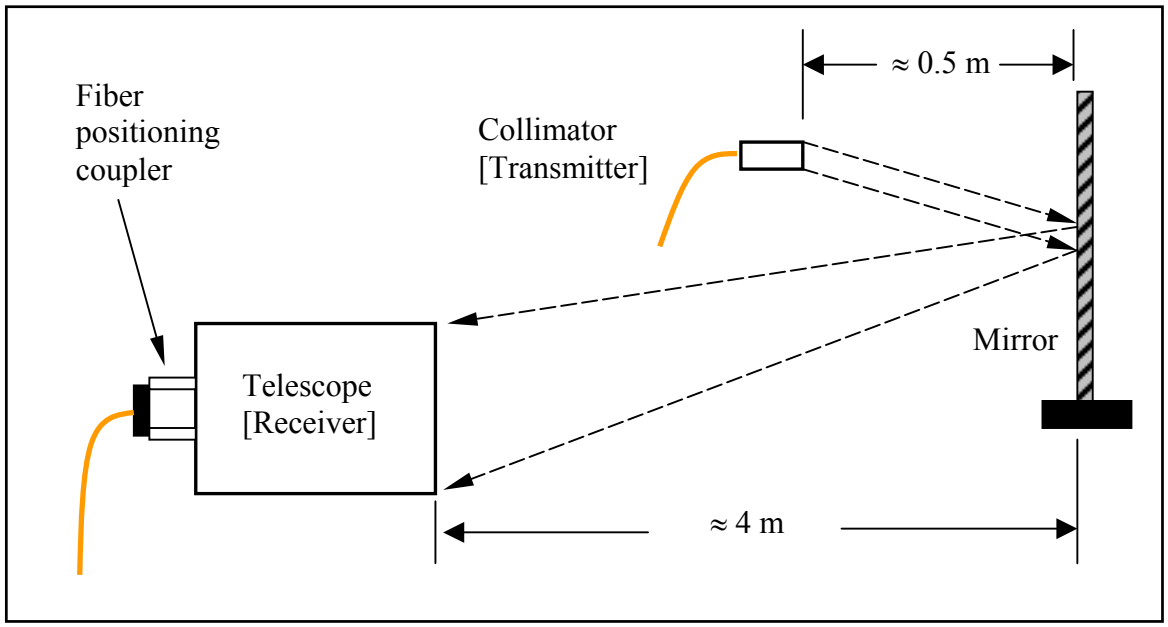

Figure 5.2.7 Envelope detection experiment setup to determine roundtrip loss.

To determine the loss, we used the test setup shown in Figure 5.2.7. We collected 1024 samples for every pulse received and processed the received signal using 32 coherent integrations. An optical attenuator provided variation in the transmitted signal power. This variation ensures that we have dynamic-range measurements. The Schottky barrier diode detector was replaced by a Mini-Circuits ZEM-4300 mixer whose LO port was terminated with a 50-Ω load. This change was made because the insertion loss of the Schottky-barrier diode is greater than 10 dB, whereas the conversion loss in the ZEM-4300 mixer is around 6 – 7 dB. The result of the measurement is given in Figure 5.2.8. where the optical transmit power is plotted against detected signal power. The telescope is fitted with a fiber-positioning coupler system to control the x- and y- position of the fiber launch. This is so we can align the fiber core with the telescope's focal plane. We used a visible fault locator, which outputs a visible red light, to enable us to see the path of the signal. The mirror is positioned so the image does not fall on the blind spot on the faceplate where the secondary mirror is situated.

The top plot in Figure 5.2.8 shows the result of the collimator-mirror-telescope experiment. The loop-back configuration experiment is given in the bottom plot, where the transmit fiber is connected to the receive fiber with a 20 m patch cord acting as a delay line. We found that, to obtain a detected signal power of 25 dB, the free-space optical transmit power has to be 22 dB higher than that needed for a fiber loop-back configuration. This difference gives us the coupling and roundtrip free-space loss. The same experimental results are plotted in terms of SNR versus optical transmit power and are shown in Figure 5.2.9.

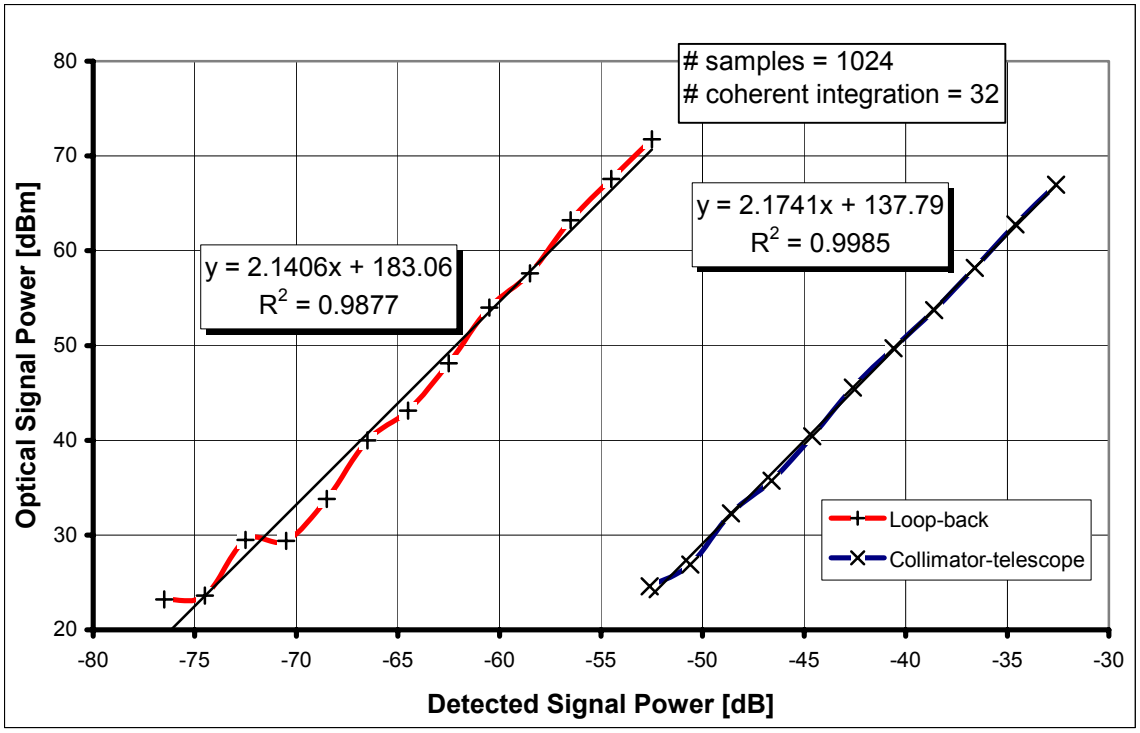

Figure 5.2.8 Envelope detection roundtrip loss measurement–optical transmit power versus detected signal power.

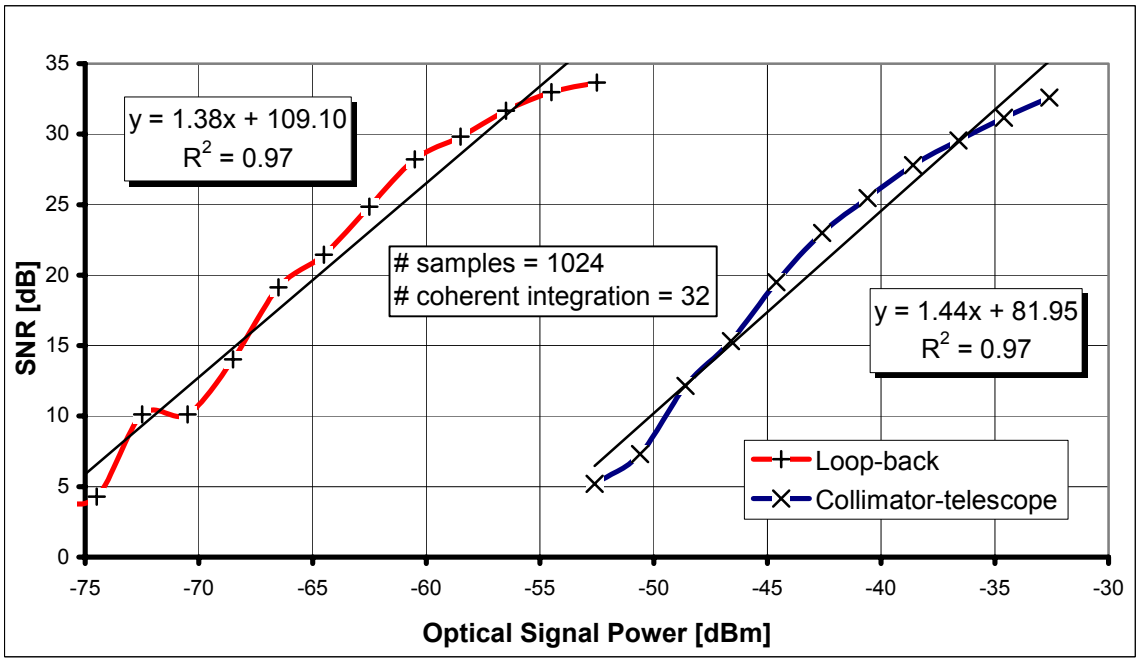

Figure 5.2.9 Envelope detection roundtrip loss measurement–SNR versus optical transmit power.

Once again, in Figure 5.2.9, we see about 22 dB more signal power is required in the free-space configuration than in the loop-back configuration.

Envelope detection—testing using plain paper as a target

An experiment was conducted using a piece of plain paper as a scattering target. The test bench setup was similar to that in the last section when we determined free-space roundtrip loss. The results of the paper target experiment are shown in Figure 5.2.11. We found that the received signal is strongest when the receive telescope is focused down to a point as shown in Figure 5.2.10. Figure 5.2.11 shows the detected SNR is about 26 dB for a piece of paper at a range of about 3 m.

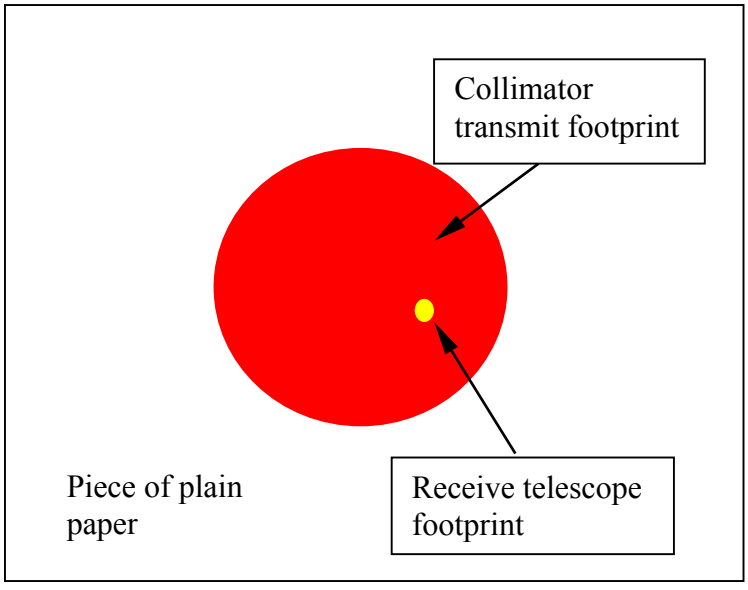

Figure 5.2.10 Footprints setup to maximize return signal power on paper target.

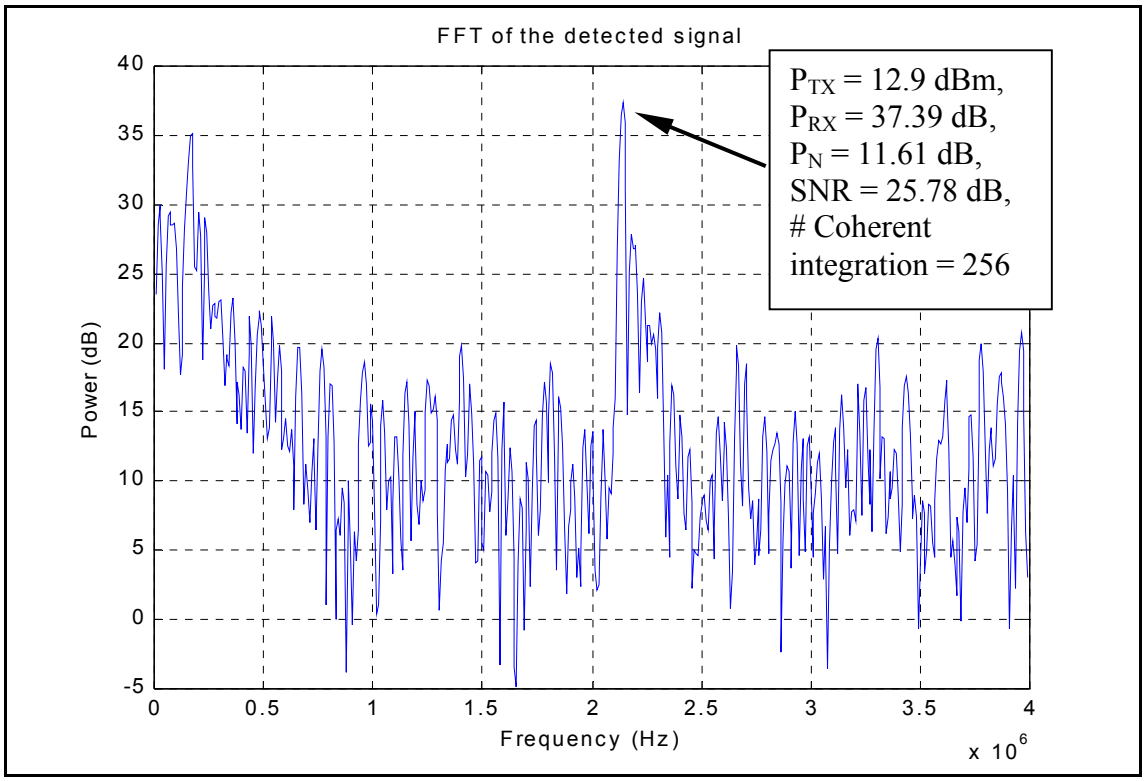

Figure 5.2.11 Detected signal using envelope detection–paper target.

5.3 Comparison of envelope detection system and frequency downconversion system

The envelope detection receiver characteristics are shown in Figure 5.3.1. In this experiment we used a Schottky-barrier diode as an envelope detector. The experiment was set up using the fiber loop-back configuration, similar to that used previously in the downconversion process. We found that the receiver has sensitivity comparable to that of the downconversion system. The minimum detectable signal is about -85 dBm. However, we see that the curve in Figure 5.3.1 has some variability as the signal power is decreased. Moreover, the slope of the curve is 1.38, which suggests a nonlinear relationship between the detected SNR and the optical signal power.

On the other hand, for the downconversion receiver, Figure 5.3.1 shows a linear, one-to-one relationship between the detected SNR and optical signal power, which is a better-fit curve. Note also that the minimum detectable signal is -90 dBm.

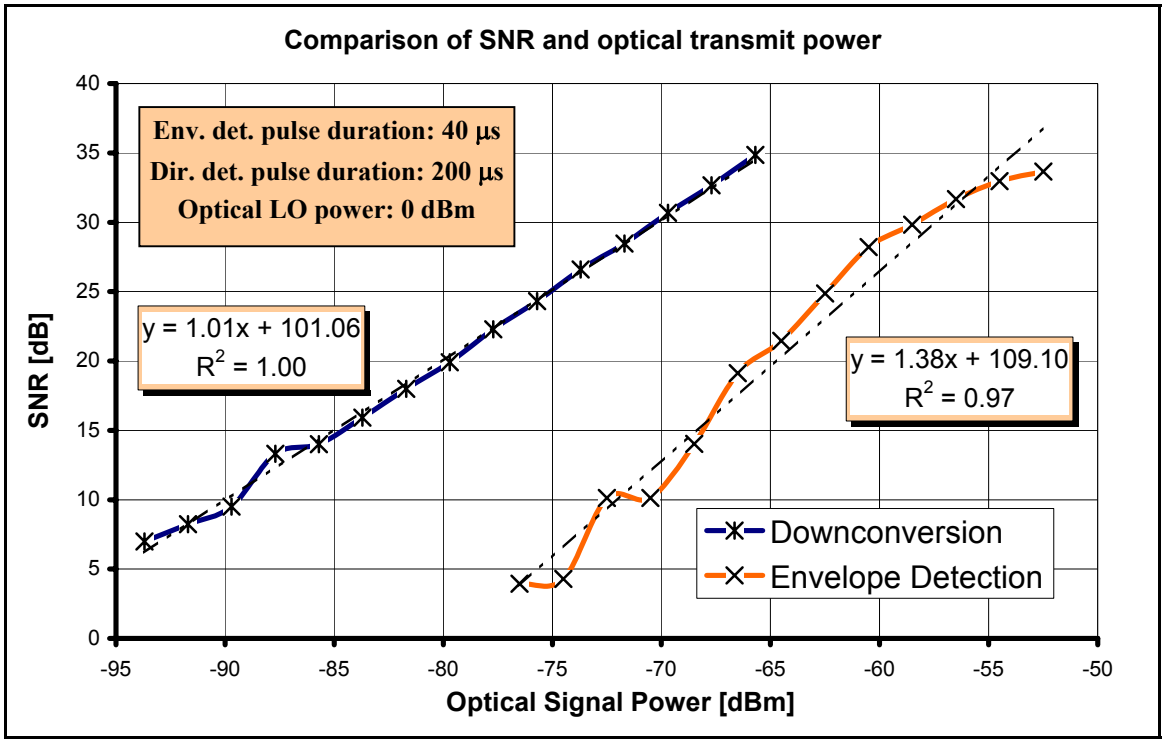

Figure 5.3.1 Comparison of downconversion and envelope detection systems.

Another advantage the downconversion system has over envelope detection is in terms of SNR and detected signal power. Figure 5.3.3 shows the variation between SNR and optical signal power for direct downconversion and envelope detection. A mixer with its LO port terminated with a 50-Ω load is used as an envelope detector. Referring to Figure 5.3.3, for an SNR of 10 dB, the envelope detection system needs around 22 dB more optical transmit power than the downconversion system. Taking into account the

different pulse width used, the pulse compression gain in downconversion system is 7 dB higher than in the envelope detection system.

Therefore, to restate, envelope detection will need 15 dB more in optical signal power than the downconversion receiver system, for a 10 dB SNR in both systems. Furthermore, the use of the envelope detector degrades the SNR by 6 – 10 dB. This is inherent in most mixers and envelope detectors.

In conclusion, the use of direct downconversion is more attractive than envelope detection in that it has a more linear response and better sensitivity. However, in the downconversion system optical phase fluctuations are prevalent. This is because (A1.6) shows that the optical phase information are present in the dechirped signal. Applying inphase and quadrature detection solves this problem of signal fading.

5.4 Homodyne detection—3×3 phase diversity receiver

In coherent systems, baseband signal fading can be a problem. The problem of phase and frequency fluctuation, due to propagation and scattering phenomenon, has already been mentioned in the previous section. Another concept we investigated briefly to address this problem of baseband signal fading is the phase diversity receiver, which employs the use of a 3×3 coupler. The 3×3 coupler introduces a 120° phase shift at the IF output ports ([23], p.79). Figure 5.4.1 shows a block diagram of the phase diversity receiver implementation.

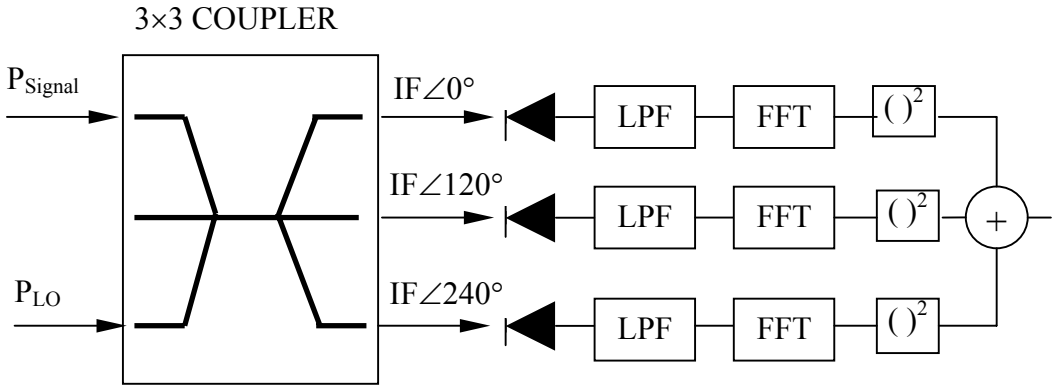

Figure 5.4.1 Principle of 3×3 symmetrical phase diversity receiver (from [23], p.80).

To illustrate the three port outputs explicitly, consider the photocurrent outputs ([23], p.79):

$$i_{P1} = 2\Re\sqrt{\frac{2P_{LO}P_S}{3}}\cos(\theta_{IF}) \tag{5.4.1}$$

$$i_{P2} = 2\Re\sqrt{\frac{2P_{LO}P_S}{3}}\cos\left(\theta_{IF} + \frac{2\pi}{3}\right) \tag{5.4.2}$$

$$i_{P3} = 2\Re\sqrt{\frac{2P_{LO}P_S}{3}}\cos\left(\theta_{IF} - \frac{2\pi}{3}\right) \tag{5.4.3}$$

where, P_{LO} = optical LO power [W],

P_S = optical signal power [W],

$\Re$ = responsivity [A/W],

θ_{IF} = intermediate frequency [rad].

The IF signal is then detected by square-law detectors and summed. The output of the summer is ([23], p.79):

$$\cos^2(\theta_{IF}) + \cos^2\left(\theta_{IF} + \frac{2\pi}{3}\right) + \cos^2\left(\theta_{IF} - \frac{2\pi}{3}\right) = \frac{2}{3} \tag{5.4.4}$$

As (5.4.4) shows, the output of the summer is independent of phase and sums up to a constant. In this way, the detected SNR will be independent of phase variations. The disadvantage of this approach is the increase in system complexity. Three channels are required from the optical receiver and right through the digital signal processing.

CHAPTER 6

CONCLUSIONS

We have demonstrated how the concept of applying RF pulse compression with an optical heterodyne receiver can improve significantly the receiver sensitivity. A more sensitive receiver allows a significant reduction in the peak transmit power required for accurate range measurements. Through analysis we have shown that this concept can be applied to a satellite-based altimeter system with a transmit peak power of less than 100 W can provide over 4000 elevation measurements per second with an accuracy of 10 cm.

We have shown that using direct downconversion of the return signal yields a linear relationship between the detected SNR and the optical signal. By implementing in-phase and quadrature detection, the detected signal is independent of signal phase.

Post-detection integration or incoherent integration lowers the variability of the noise significantly. As a result, incoherent integration can be used to lower noise variability so the SNR can be increased.

We have shown that the breadboard laser radar system can detect scattering targets at ranges of up to 35 m. Tests show that the detected signal has a range-squared dependence, which agrees with theory. The targets detected include snow, leaves, grass, rock, paper and asphalt. Thus the laser radar could be used in a variety of ranging applications; from measuring the height of forests to mountain ranges.

With SNRs greater than 10 dB for the different targets, we satisfied the requirements needed to achieve a 10 cm range accuracy using the breadboard laser radar system.

One of the major problems we encountered during our experimentation was the alignment of the receiver and transmitter telescopes. The received signal power was very sensitive to the alignment of the transmit and receive optics. The introduction of the MTP linear fiber array solved this alignment problem. By attaching the MTP array to the telescope, a single telescope acts as both a transmit and receive apertures. This setup is desirable since the telescope with the MTP array has high isolation (greater than 90 dB between fibers), thus reducing self-jamming. Furthermore, because only one telescope is involved in transmission and reception, the alignment issue is avoided.

When envelope detection is used instead of direct downconversion, the system linearity is compromised somewhat. In addition, a larger minimum detectable signal is required. However with envelope detection, the effects of optical frequency and phase variations (including include laser phase noise, effects of atmospheric turbulence, and frequency shifting due to Doppler effects) do not appear in the detected signal. Consequently coherent integrations may be used to improve the detected SNR. We demonstrated that number of coherent integrations is proportional the the improvement in SNR and the received signal power. The use of coherent integration further enhances the sensitivity of the receiver.

CHAPTER 7

RECOMMENDATIONS FOR FUTURE WORK

While this project successfully demonstrated the feasibility of heterodyne optical downconversion and RF pulse compression to dramatically improve receiver sensitivity, a number of technical issues remain unresolved that could further improve system performance.

The free-space roundtrip loss in the telescope-air-target interface is approximately 22 dB, as shown in Chapter 5, and is due to coupling losses and optical alignment issues. A theoretical coupling loss of about 5 dB should be possible. One possible cause of the excessive loss can be the beam launch conditions, collimated vs. focused beam. Thus far we found our best results when the beam was focused on the target, however further investigation is needed to determine an optimum focusing scheme.

The acousto-optic frequency shifter introduces an insertion loss of about 10 dB to 12 dB on both the first and zeroth order output port. Since the breadboard laser radar requires a high LO power, another LO laser source that is frequency locked to the signal laser source can be incorporated into the laser radar system, thus avoiding the need for the acousto-optic frequency shifter. This approach would permit lower power lasers to be used to realize the heterodyne optical downconversion.

The balanced photodetector used in the breadboard laser radar has a bandwidth of 800 MHz, but the photodetected signal's upper frequency sideband reaches up to 960 MHz. Hence, the bandwidth of the photodetector rolls off in the upper end of the signal bandwidth. Furthermore, the directly detected signal at baseband will overlap with the coherently detected signal, at the output of the balanced photodetector. This overlap is

illustrated in Figure 7.1. The use of a higher bandwidth balanced photodetector solves the bandwidth problem. Moreover, the optical LO frequency can be increased so the directly detected signal and the coherently detected signal do not overlap in frequency. For example, the use of a 1500 MHz shifted optical LO will shift the double-sided band AM signal to a higher frequency. This is shown in Figure 7.2.

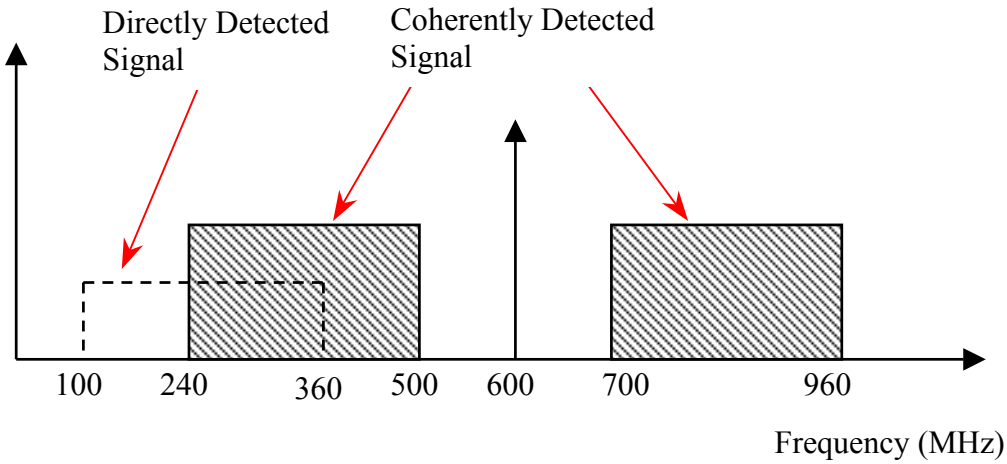

Figure 7.1 Overlap of directly detected and coherently detected signals.

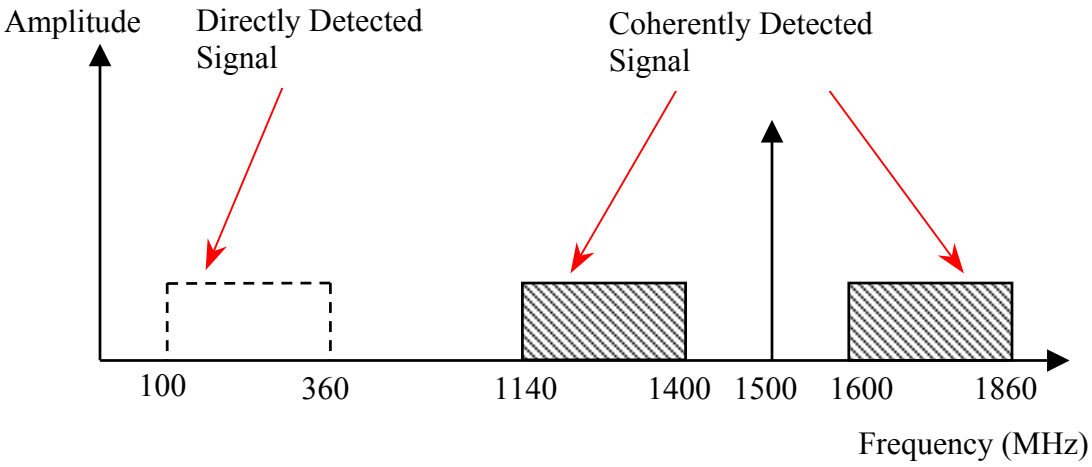

Figure 7.2 Directly detected and coherently detected signal using 1500 MHz LO.

The fiber core diameter for single-mode fibers is only 9 μm. Therefore, the efficiency of coupling light into a small diameter is low compared to coupling light into a larger diameter core. Multimode fibers have relatively larger cores ranging from 50 μm to 100 μm, and this allows for more efficient coupling of light into the fiber. An investigation of the tradeoffs associated with using multimode fibers in the receiver could significantly improve the coupling efficiency from free space into the optical fiber.

Our attempts to realize envelope detection involved Schottky-barrier diodes and an RF mixer. Perhaps by using ideal envelope detection and subsequent dechirping could result in better results. Ideal envelope detection may be achieved digitally, i.e. after digitization. This would require wide-bandwidth data acquisition system to digitize the IF signal.

The transmitted signal bandwidth in our system was 260 MHz, however much greater bandwidths are easily realized. Methods to convert this excess bandwidth into improved receiver sensitivity should be investigated.

Our system operated in a chirped-pulse mode with a duty factor of about 20%. By operating in FM-CW mode (duty factor of 100%) should result in a five-fold improvement in receiver sensitivity.

In our system we used heterodyne optical downconversion to recover the RF signal from the optical carrier. It is well known that homodyne detection is superior to heterodyne in terms of SNR. Furthermore, in homodyne detection the optical LO is easily derived from the master laser. However to prevent signal fading due to phase variations, a phase diversity receiver is required which may require a three-channel data acquisition system. The tradeoffs of this approach should be investigated.

REFERENCES

[1] National Aeronautics and Space Administration (NASA), "Polar ice," The Earth Science Enterprise Series, NF-212, Maryland, April 1998. (This article can be found on the website address http://www.eipfed.org/knowledge_center /polar_ice.pdf)

[2] Twilley, R. and Reed, D., "Global warming and sea-level rise in the Gulf Coast region," *Selected Findings from Confronting Climate Change in the Gulf Coast Region*, Union of Concerned Scientists, Ecological Society of America, October 2001. (This article can be found on the website address http://www.ucsusa.org/environment/gcsealevel.pdf)

[3] Kachelmyer, A. L., "Range-Doppler imaging: wave-forms and receiver design," Laser Radar III, R. J. Becherer, Ed., Proceedings of the SPIE, Vol. 999, pp. 138-161, 1988.

[4] Mullen, L. J., A. J. C. Vieira, P. R. Herczfeld, and V. M. Contarino, "Application of RADAR technology to aerial LIDAR systems for enhancement of shallow underwater target detection," *IEEE Transactions on Microwave Theory and Techniques*, 43(9), pp. 2370-2377, 1995.

[5] Allen, C. and P. Gogineni, "A fiber-optic-based 1550-nm laser radar altimeter with RF pulse compression," *Proceedings of the 1999 International Geoscience and Remote Sensing Symposium* (IGARSS '00), Honolulu, Hawaii, pp. 1784-1786, July 2000.

[6] Allen, C. Y. Cobanoglu, S. K. Chong, and S. Gogineni, "Development of a 1310-nm, coherent laser radar with RF pulse compression," *Proceedings of the 1999*

International Geoscience and Remote Sensing Symposium (IGARSS '99), Hamburg, Germany, pp. 1740-1742, June 1999.

[7] Allen, C., Y. Cobanoglu, S. K. Chong, and S. Gogineni, "Performance of a 1319 nm laser radar using RF pulse compression," *Proceedings of the 2001 International Geoscience and Remote Sensing Symposium (IGARSS '01)*, Sydney, session SS52, paper Th03-04, July 2001.

[8] Akins, T. L., "Design and development of an improved data acquisition system for the coherent radar depth sounder", MSEE Thesis, Department of Electrical Engineering and Computer Science, University of Kansas, 1998.

[9] Jelalian, A. V., *Laser Radar Systems*, Artech House, Norwood, MA., 1992.

[10] Skolnik, M. I., "Theoretical accuracy of radar measurements," *IRE Transactions on Aeronautical and Navigational Electronics*, pp. 123-129, Dec. 1960.

[11] Lillesand, M., and R. W. Kiefer, *Remote Sensing and Image Representation*, John Wiley & Sons, Inc, New York City, 1987, p. 12.

[12] Green, P. E., *Fiber Optic Networks*, Prentice-Hall, New Jersey, 1993.

[13] Liu, M. M.-K., *Principles and applications of optical communications*, Irwin Book Team, Chicago, 1996.

[14] Peebles, P. Z., Jr., *Radar Principles*, John Wiley & Sons, New York City, 1998.

[15] Stimson, G. W., *Introduction to Airborne Radar,* 2nd ed., Scitech Publishing, New Jersey, 1998.

[16] Allen, C., "Analysis of a Digital Chirp Synthesis", *Exploratory Radar Development*, Sandia National Laboratories, Albuquerque, New Mexico, August, 1988.

[17] Haykin, S., *Communication Systems,* 3rd ed., John Wiley & Sons, New York City, p. 122, 1994.

[18] Levanon, N., *Radar Principles*, John Wiley & Sons, New York City, 1988.

[19] Uniphase Telecommunications Products, "APE Extended Frequency Response Modulator," Form MWI-09.701/1 Rev. A, 1999.

[20] Shaklan, S. "A long-baseline interferometer employing single-mode fiber optics," *Fiber Optics in Astronomy* – Vol. 3, S. C. Barden, Ed., pp. 262-268, 1988.

[21] Shaklan, S., and R. Roddier, "Coupling starlight into single-mode fiber optics," *Applied Optics*, 27(11), pp. 986-988, 1998.

[22] Winzer, P. J., and W. R. Leeb, "Fiber coupling efficiency for random light and its applications to lidar," *Optics Letters*, 23 (13), pp. 986-988, 1998.

[23] Hooijmans, P. W., *Coherent Optical System Design*, John Wiley & Sons, New York City, 1994.

APPENDIX 1

Laser radar receiver analysis – Direct downconversion system.

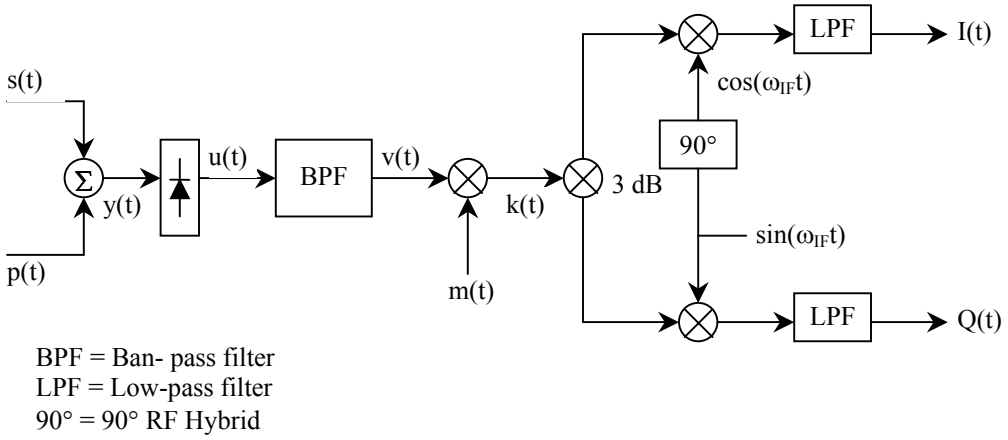

Figure A1.1 In-phase and quadrature detection process.

The analysis of the inphase and quadrature detection system is given below. Figure A1.1 shows the block diagram of the detection process.

Let s(t) be the frequency down-shifted and intensity modulated optical transmit signal, and p(t) be the optical local oscillator.

$\omega_s = 2\pi(f_c - f_d)$

$\omega_c = 2\pi f_c$

f_c = frequency of the laser source

f_d = amount of frequency downshifting

$\phi(t)$ = arbitrary starting phase

Then,

$$s(t) = A_s\left[1+\beta m(t-\tau)\right]\cos\left[\omega_s\left(t-\tau\right)+\phi(t-\tau)\right] \tag{A1.1}$$

$$p(t) = A_c\cos(\omega_c t) \tag{A1.2}$$

where β = modulation index,

$m(t)$ = baseband signal,

A_s = signal amplitude,

A_c = carrier amplitude

τ = roundtrip delay.

Let $y(t)$ be the optical mixing of the return signal, after a delay of τ seconds, and the local oscillator in the fiber optic coupler.

$$\begin{aligned} y(t) &= s(t)+p(t) \\ &= A_s\left[1+\beta m(t-\tau)\right]\cos\left[\omega_s\left(t-\tau\right)+\phi(t-\tau)\right]+A_c\cos(\omega_c t) \end{aligned} \tag{A1.3}$$

Then at the photodetector current output, $u(t)$ is obtained by the square-law photodetection process.

$$\begin{aligned} u(t) &= \Re y^2(t) \\ &= \Re\begin{bmatrix} A_s^2\left[1+\beta m(t-\tau)\right]^2\cos^2\left[\omega_s\left(t-\tau\right)+\phi(t-\tau)\right]+{A_c}^2\cos^2(\omega_c t) \\ +2A_sA_c\left[1+\beta m(t-\tau)\right]\cos\left[\omega_s\left(t-\tau\right)+\phi(t-\tau)\right]\cos(\omega_c t) \end{bmatrix} \\ &= \Re\begin{bmatrix} \tfrac{1}{2}A_s^2\left[1+\beta m(t-\tau)\right]^2\left\{1+\cos 2\left[\omega_s\left(t-\tau\right)+\phi(t-\tau)\right]\right\} \\ +\tfrac{1}{2}A_c^2\left[1+\cos(2\omega_c t)\right] \\ +A_sA_c\left[1+\beta m(t-\tau)\right]\begin{Bmatrix}\cos\left[\omega_s\left(t-\tau\right)+\omega_c t+\phi(t-\tau)\right] \\ +\cos\left[\omega_s\left(t-\tau\right)-\omega_c t-\phi(t-\tau)\right]\end{Bmatrix} \end{bmatrix} \end{aligned} \tag{A1.4}$$

Let $\omega_s - \omega_c = \omega_{IF}$, where $\omega_{IF} = 2\pi f_d$. Then the output of the band-pass filter is

$$v(t) = \tfrac{1}{2}A_s^2\left[\beta m(t-\tau)\right]^2 + A_cA_s\beta m(t-\tau)\cos\left[\omega_{IF}t-\phi(t)\right] \tag{A1.5}$$

The photodetector filters out twice the carrier frequency and DC.

Dechirping the signal v(t) gives,

$$\begin{aligned} k(t) &= v(t)m(t) \\ &= \tfrac{1}{2}A_s^2 m(t)\left[\beta m(t-\tau)\right]^2 \\ &+ A_c A_s m(t)\left[\beta m(t-\tau)\right]\cos\left[\omega_{IF}t - \phi(t)\right] \end{aligned} \tag{A1.6}$$

Then, from the I and Q downconversion process and low-pass filtering,

$$\begin{aligned} I(t) &= k(t)\cos(\omega_{IF}t) \\ &= A_c A_s m(t)\left[\beta m(t-\tau)\right]\cos\left[\omega_{IF}t - \phi(t)\right]\cos(\omega_{IF}t) \\ &= \tfrac{1}{2}A_c A_s m(t)\left[\beta m(t-\tau)\right]\cos\left[\phi(t)\right] \end{aligned} \tag{A1.7}$$

$$\begin{aligned} Q(t) &= k(t)\sin(\omega_{IF}t) \\ &= A_c A_s m(t)\left[\beta m(t-\tau)\right]\cos\left[\omega_{IF}t - \phi(t)\right]\sin(\omega_{IF}t) \\ &= \tfrac{1}{2}A_c A_s m(t)\left[\beta m(t-\tau)\right]\sin\left[\phi(t)\right] \end{aligned} \tag{A1.8}$$

The low-pass filter blocks out the higher frequency, but passes the selected frequency terms. The selection of the low-pass filter depends on the beat frequency of the dechirped signal, which in turn depends on the range of the target. We have seen from (2.7.7) that the dechirped signal s(t) is:

$$s(t) = \frac{1}{2}\cos\left(2\pi f_o \tau + \frac{\pi B t \tau}{T} + \frac{\pi B \tau^2}{T}\right)$$

and the frequency that corresponds to the range was given in (2.7.8) as:

$$f_R = \frac{B}{T}\tau.$$

APPENDIX 2

Laser radar receiver analysis – Envelope detection

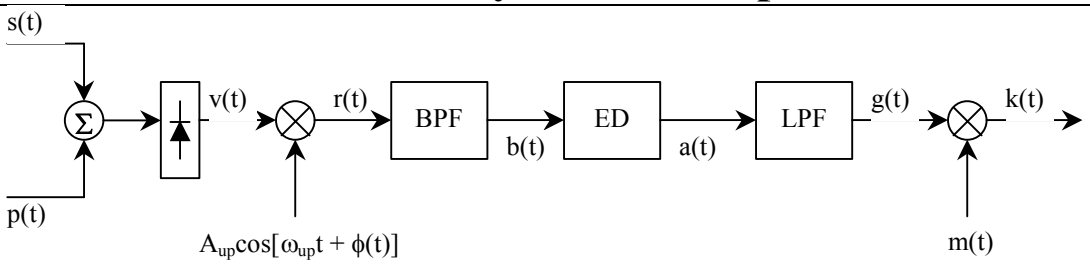

BPF = Band pass filter
ED = Envelope Detector
LPF = Low pass filter

Figure A2.1 Envelope detection analysis block diagram.

Analysis of the envelope detection process is shown in the following paragraphs below. The block diagram of the envelope detection process is given in Figure A2.1 above.

Let v(t) be the photodetected signal as defined in Appendix 1, assuming that the photodiode has a band-pass filter at the output. Then beginning from (A1.5),

$$v(t) = \tfrac{1}{2} A_s^2 \left[\beta m(t-\tau)\right]^2 + A_c A_s \left[1 + \beta m(t-\tau)\right] \cos\left[\omega_{IF} t - \phi(t)\right]$$

The spectrum of the photodetected return signal will now have the shape shown in Figure A1.2.

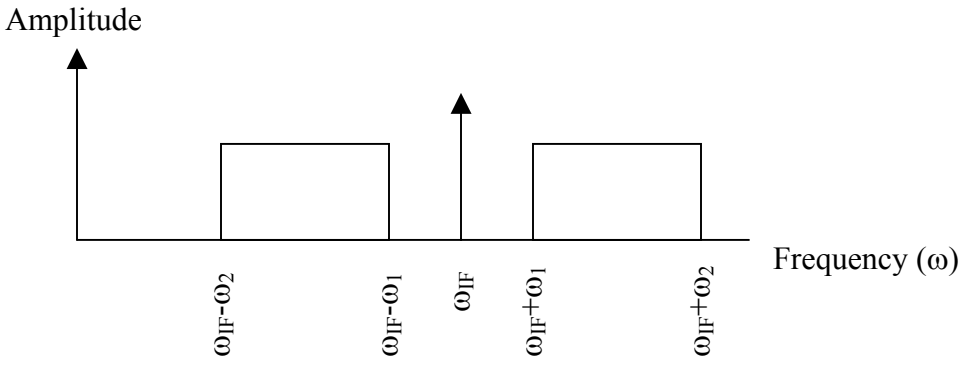

Figure A1.2 Spectrum of photodetected signal.

Where $\omega_1 = 2\pi f_1$, f_1 = chirp start frequency

$\omega_2 = 2\pi f_2$, f_2 = chirp stop frequency

The upconversion process yields

$$\begin{aligned} r(t) &= v(t)q(t) \\ &= v(t)A_{up}\cos\left[\omega_{up}t + \phi_{up}(t)\right] \\ &= \tfrac{1}{2}A_s^2 A_{up}\left[\beta m(t-\tau)\right]^2\cos\left[\omega_{up}t + \phi_{up}(t)\right] + \\ &\quad A_s A_c A_{up}\left[1 + \beta m(t-\tau)\right]\cos\left[\omega_{up}t + \phi_{up}(t)\right]\cos\left[\omega_{IF}t - \phi(t)\right] \\ &= \tfrac{1}{2}A_s^2 A_{up}\left[\beta m(t-\tau)\right]^2\cos\left[\omega_{up}t + \phi_{up}(t)\right] + \\ &\quad \tfrac{1}{2}A_s A_c A_{up}\left[1 + \beta m(t-\tau)\right]\left\{\begin{matrix}\cos\left[(\omega_{up} - \omega_{IF})t + \phi_{up}(t) + \phi(t)\right] \\ + \cos\left[(\omega_{up} + \omega_{IF})t - \phi(t) + \phi_{up}(t)\right]\end{matrix}\right\} \end{aligned} \qquad \text{(A2.1)}$$

where $q(t) = A_{up}\cos[\omega_{up}t + \phi_{up}(t)]$,

A_{up} = upconversion frequency amplitude,

ω_{up} = upconversion angular frequency,

$\phi_{up}(t)$ = upconversion frequency starting phase.

To perform envelope detection efficiently, the carrier frequency must be at least ten times higher than the maximum frequency of the envelope (signal) waveform.

A band-pass filter is selected with a center frequency of $\omega_{up} + \omega_{IF}$, and a bandwidth sufficient to cover the bandwidth of the up-converted sidebands. Therefore, the output of the band-pass filter becomes:

$$b(t) = \tfrac{1}{2}A_s A_c A_{up}\left[1 + \beta m(t-\tau)\right]\left\{\cos\left[(\omega_{up} + \omega_{IF})t - \phi(t) + \phi_{up}(t)\right]\right\} \qquad \text{(A2.2)}$$

The signal then goes through an envelope detector which we shall treat this as a square-law detector. Hence,

$$
\begin{aligned}
a(t) &= b^2(t) \\
&= \left\{\tfrac{1}{2} A_s A_c A_{up}\left[1+\beta m(t-\tau)\right]\cos\left[(\omega_{up}+\omega_{IF})t-\phi(t)+\phi_{up}(t)\right]\right\}^2 \\
&= \left(\tfrac{1}{2} A_s A_c A_{up}\right)^2\left[1+2\beta m(t-\tau)+\beta^2 m^2(t-\tau)\right]\cos^2\left[(\omega_{up}+\omega_{IF})t-\phi(t)+\phi_{up}(t)\right] \\
&= \tfrac{1}{2}\left(\tfrac{1}{2} A_s A_c A_{up}\right)^2\left[1+2\beta m(t-\tau)+\beta^2 m^2(t-\tau)\right]\times \\
&\qquad \left\{1+\cos 2\left[(\omega_{up}+\omega_{IF})t-\phi(t)+\phi_{up}(t)\right]\right\}
\end{aligned}
\tag{A2.3}
$$

Then the signal is low-pass filtered to retrieve the return signal information.

$$
g(t) = \tfrac{1}{8}\left(A_s A_c A_{up}\right)^2 + \tfrac{1}{8}\left(A_s A_c A_{up}\right)^2\left[1+2\beta m(t-\tau)\right] \tag{A2.4}
$$

We see from g(t) that the optical phase and the phase of the up-conversion frequency is absent. As a result, envelope detection process eliminates any return phase uncertainty that causes fluctuation in the detected signal.

Dechirping the signal g(t) gives,

$$
\begin{aligned}
k(t) &= g(t)m(t) \\
&= \tfrac{1}{8}\left(A_s A_c A_{up}\right)^2\left[2+2\beta m(t-\tau)\right]m(t) \\
&= \tfrac{1}{4}\left(A_s A_c A_{up}\right)^2 + 2\beta m(t-\tau)m(t)
\end{aligned}
\tag{A2.5}
$$

Then we pass the dechirped signal through a low pass filter, and a DC block. The low-pass filter is selected based on the maximum frequency. Thus, the low-pass filter will have a cutoff frequency corresponding to this maximum range. Hence, the final output becomes

$$
w(t) = 2\beta m(t-\tau)m(t) \tag{A2.6}
$$